Title
Investigation of Peculiar Steady and Unsteady Flow Behavior of Dense Gas

Permalink
https://escholarship.org/uc/item/464992w2

Author
Zhu, Jie

Publication Date
2022

Peer reviewed|Thesis/dissertation

UNIVERSITY OF CALIFORNIA,
IRVINE

Investigation of Peculiar Steady and Unsteady Flow Behavior of Dense Gas

DISSERTATION

submitted in partial satisfaction of the requirements
for the degree of

DOCTOR OF PHILOSOPHY

in Mechanical and Aerospace Engineering

by

Jie Zhu

Dissertation Committee:
Professor Feng Liu, Chair
Professor William Sirignano
Professor Yun Wang

2022

TABLE OF CONTENTS

LIST OF FIGURES

LIST OF TABLES

Page

ACKNOWLEDGMENTS

First and foremost, I would like to express my deepest gratitude to my advisor Professor Feng Liu, valuable guidance and support throughout the years of my dissertation research. Without him I would not have the opportunity to pursue PhD studies at UC Irvine and finish this research.

I would like to thank my Ph.D. committee members Professor William Sirignano and Professor Yun Wang for sparing time out of their busy schedule to serve on the committee and for their helpful advice.

I also want to thank Dr. Juntao Xiong for sharing his knowledge in CFD with me and providing me advices whenever I encountered problems during my research.

I would like to thank all my friends and colleagues in the CFD lab, Rayomand Gundevia, Zihao Zhu, Jingyi Zeng, Lei Zhan and Ferran Marti Duran for help not only in my research but also in my daily life. It is a great honor to be able to work and share ideas with them for the past few years.

Last but not least, I would like to thank my parents and my girl friend, Linh Ly, for their love and unconditional support during this journey. Without their support I would not be able to get through this long journey.

VITA

Jie Zhu

EDUCATION

Doctor of Philosophy in Mechanical and Aerospace Engineering **2022**
University of California, Irvine *Irvine, California*

Master of Science in Mechanical and Aerospace Engineering **2015**
University of California, Irvine *Irvine, California*

Bachelor of Science in Mechanical Engineering **2013**
Shanghai Jiao Tong University *Shanghai, China*

RESEARCH EXPERIENCE

Graduate Research Assistant **2015–2022**
University of California, Irvine *Irvine, California*

TEACHING EXPERIENCE

Teaching Assistant **2015–2022**
University of California, Irvine *Irvine, California*

ABSTRACT OF THE DISSERTATION

Investigation of Peculiar Steady and Unsteady Flow Behavior of Dense Gas

By

Jie Zhu

Doctor of Philosophy in Mechanical and Aerospace Engineering

University of California, Irvine, 2022

Professor Feng Liu, Chair

Due to the dramatic increase in global energy consumption in the past decade, thermodynamic power cycles such as Oraganic Rakine Cycle and Supercritical Carbon Dioxide Cycle draw lots of attention recently because of their high efficiency in waste heat recovery. The fluids in these power cycles usually have complex molecular structure and operate in the vicinity of saturation vapor line and critical point, where the gas behavior significantly deviates from the ideal gas behavior. Objective of this dissertation is to numerically investigate and understand the peculiar gas behavior in this region.

The fundamental derivative of gas dynamics is a measurement of the variation of the speed of sound of a gas with respect to pressure in an isentropic process. The van der Waals model is used to confirm the existence of negative fundamental derivative regions for dense gas. Regions of $\Gamma < 0$, $0 < \Gamma < 1$ and $1 < \Gamma$ are identified and mapped out in the p-v diagram. Jump relations are investigated in three regions of $\Gamma, i, e.\Gamma > 1$, $0 < \Gamma < 1$ and $\Gamma < 0$ respectively. The non-monotone dependence of the speed of sound along a shock adiabat is demonstrated to result in the increase of the sound speed across normal shock waves in the region where $1 > \Gamma > 0$. Expansion shock solution is obtained in the region where $\Gamma < 0$. Double sonic shock wave are confirmed admissible where fluid can be expanded and accelerated through a discontinuity with Mach number being unity before and after the discontinuity. Unconventional gas behaviors of the isentropic quasi-1D flow have been investigated systematically and in depth for dense gas. Analysis indicates that dense gas behavior in one dimensional nozzle is directly related to the value of Γ. For example, when $\Gamma < 0$, the divergent-convergent nozzle is needed to accelerate flow from subsonic to supersonic. A real gas numerical solver using Jameson-Schmidt-Turkel scheme is developed. Simulation result of dense gas over compression ramp and expansion ramp shows agreement with the analytical solution and confirms the existence of complicated wave field such as expansion shock and expansion shock-fan. Results of unsteady shock tube simulation show that shock tube can produce different wave fields depending on the initial conditions. More results of dense gas over corners and arc surface are presented and discussed in details.

Chapter 1

Introduction

1.1 Background and Motivation

Global energy consumption has increased dramatically in recent decades as a result of rising industrialization and human demand. The energy consumption climbed by 2.9 percent in 2018 and will continue to rise, according to the BP Statistical Review of World Energy 2019 [1], resulting in higher energy prices and environmental issues. Among the huge energy usage, fossil fuels (coal, peat, shale, oil, and natural gas) account for over 80% of world primary energy supply, according to data from 2017 [2]. Biofuels account for 10% of the total, while nuclear and renewable energy each account for only 5%. According to studies, only 18% of primary energy gets transformed into electricity, with the rest going towards heat and transportation.

Sulfur dioxide, nitrogen oxides, ammonia, particulate matter, carbon monoxide, volatile organic compounds, and ozone are all produced when fossil fuels are burned [3]. Sulfur dioxide is mostly created by coal combustion. Sulfur dioxide aggravates nasal congestion, asthma, pulmonary inflammation, and other respiratory problems; it also contributes to acid rain and hazardous particle production in the atmosphere. Particulate matter, commonly known as soot, can cause haze and aggravate health disorders such as aggravated asthma and chronic bronchitis, as well as being linked to an increased risk of early mortality.

In addition to the pollutants stated above, fossil fuel combustion also produces global warming emissions, which have the potential to have irreversible implications for the Earth's atmosphere [4]. Global warming is caused by the release of greenhouse gases, which results in the formation of ground-level ozone, a rise in sea levels, more severe and frequent natural disasters such as flooding, wildfires, drought, and storm surges, an increase in the number of heat-related deaths, increased ocean acidity, and ultimately increased mortality and morbidity [4]. Coal, oil, and natural gas burning are the leading sources of greenhouse gas emissions worldwide. When fossil fuels are burned, they produce carbon dioxide.

Increasing environmental concerns, as well as more rigorous national and international laws on greenhouse gas emissions, are driving academia and industry to seek innovative sustainable solutions to meet rising energy demand. Aside from increasing the percentage of renewable in the energy mix, improving the energy efficiency of existing industrial and power generation facilities is seen as critical to meeting the aforementioned goals. A variety of renewable and cleaner energy has been studied and used including solar, wind, tidal, biomass energy or hybrid renewable energy systems. However, despite the fact that coal-burning power plants emit approximately 40% of CO_2, cleaner options cannot compete with them since coal is such a cheap and readily available resource [5]. Even with government laws and restrictions on the use of fossil fuels, their use is predicted to expand and continue to meet a large portion of the world's energy demand. Nearly 50% of energy is wasted throughout the world [6] during the energy consumption process, thus the development of waste heat recovery is of primary research interests.

Flue gas, liquid flows, steam, and gases from processes or vapors are the four sources of waste heat, with temperature ranges ranging from 50 to 800 C^o [7]. Various thermodynamic cycles have been proposed and studied for the conversion of waste heat source into electricity.

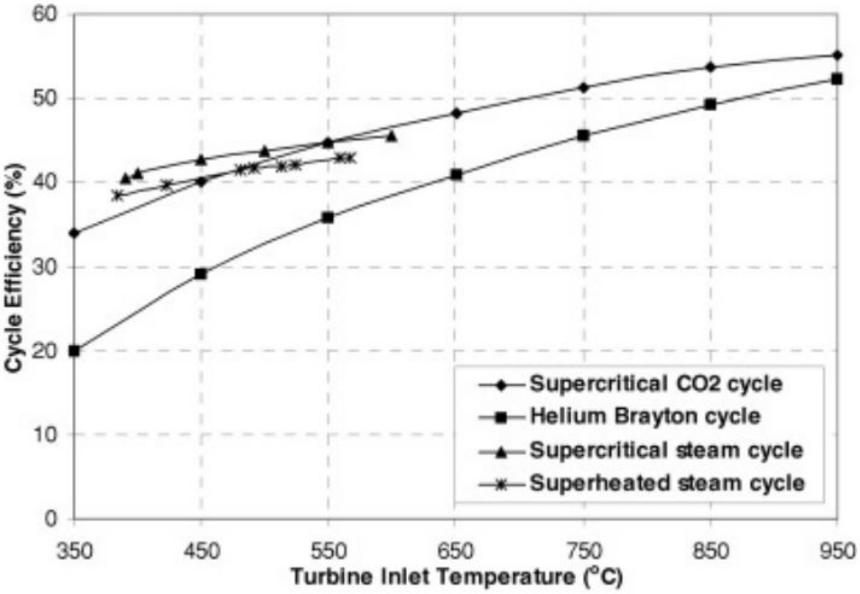

Figure 1.1: Cycle efficiency comparison of advanced power cycles[8]

One example is Supercritical Carbon Dioxide (sCO_2) Cycle. sCO_2 cycle was first proposed in 1968 by E.G.Feher[9] in order to overcome the drawback of the phase change and low power conversion rate of traditional Rankine Cycle and Brayton Cycle. Much attention has been given to Supercritical CO_2 cycles due to the development of nuclear power and nuclear reactors, where the operating temperature are commonly 500^oC to 900^oC [10]. Fig 1.1 compares the efficiency of sCO_2 cycles with other supercritical cycles. sCO_2 power cycles are considered one of the highest efficiency power cycle to successfully utilize the high heat source temperature. Besides the high efficiency, it also significantly reduces the compression work of the compressor by operating near the critical point and leads to a very compact design. With CO_2's critical temperature at 30.98 C^o as shown in table 1.1, air cooling would be possible for supercritical CO2 power cycle.

Another example is Organic Rankine Cycle (ORC) [11].The Organic Rankine cycle has the same system configuration as traditional steam Rankine cycle, but it uses organic compounds as working fluid. For small to medium power plants, the advantage of employing organic

Name	Formula	Critical temperature (^OC)	Critical pressure (Mpa)
Ammonia	NH_3	132.89	11.28
Carbon Dioxide	CO_2	30.98	7.38
Hexafluorobenzene	C_6F_6	237.78	2.77
Perfluoropropane	C_3F_8	71.89	2.68
Sulfer Dioxide	SO_2	157.60	7.88
Sulfur Hexafluoride	SF_6	45.56	3.76
Water	H_2O	373.89	22.10
Xenon	Xe	16.61	5.88

Table 1.1: Critical constant of different fluids

molecules is in the design and building of the power plants, which are simpler and less expensive than steam Rankine Cycle facilities [12]. Organic Rankine Cycle has been proved to be suitable for recovering low grade waste heat and for power generation [13].

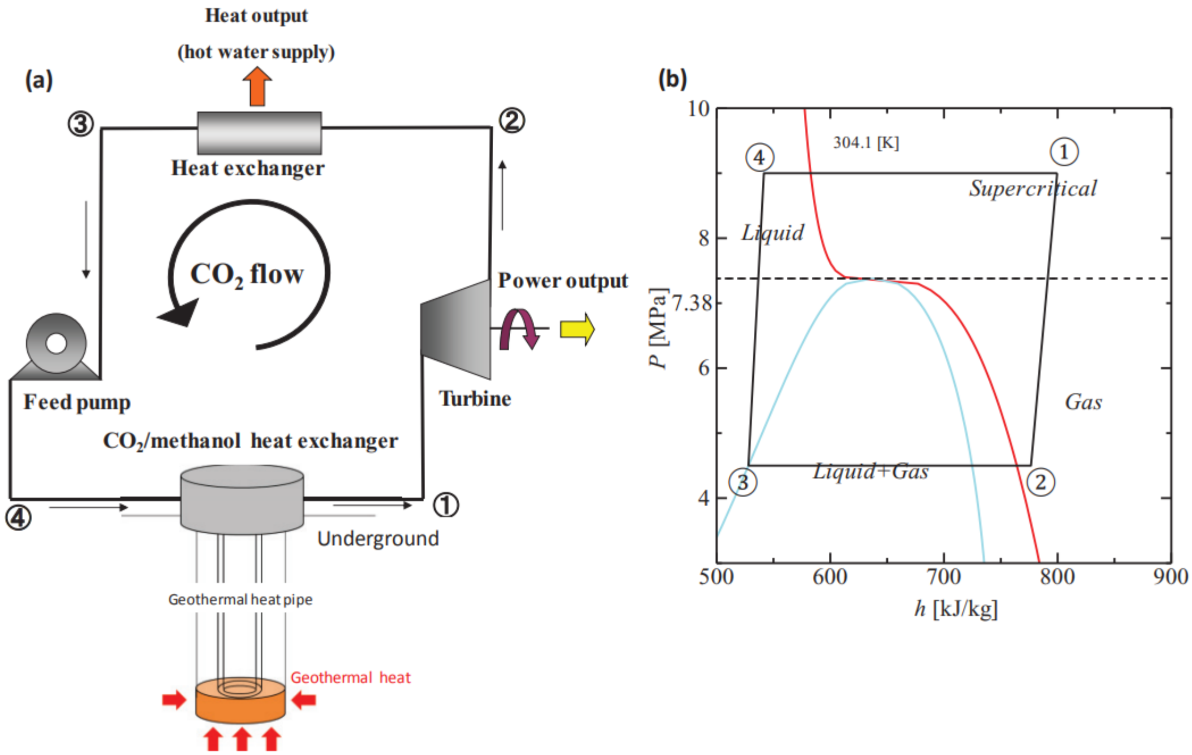

Figure 1.2: (a) Schematic diagram of supercritical CO2 Rankine cycle with geothermal heat pipe and (b) P-h diagram (blue line is saturate vapor line and red line is isotherm at $T = T_c$) [14]

The system configuration and cycle configuration is shown in Fig 1.2 and Fig 1.3 for sCO_2

cycle and Organic Rankine Cycle. As shown in the figure, these advanced cycles operate in the vicinity of the critical point or near the saturation vapor line. The fluid dynamic design of efficient turbo machinery components, such as the compressor, turbine and expander, is the most difficult portion of power cycle design in or near the non-ideal compressible fluid region. The design and performance analysis of components in conventional thermodynamics cycles heavily rely on ideal-gas law, which neglects the inter-molecular force, to describe the fluids thermodynamics properties [15]. But in the region near the critical point and saturation vapor line, the inter-molecular force plays a major role and a significant departure from ideal-gas behavior is observed [16]. In this region of thermodynamic conditions, the ideal-gas law can no longer accurately predict the gas behavior, more complicated equations of states are required to achieve accurate prediction [17][18][19]. In this region, fluids with high molecular complexity can also exhibit qualitatively different fluid dynamic behavior such as expansion shock and mixed shock/fan waves [20][21]. Thus, this region is often referred as the non-classical region. Details will be discussed in next section. Figure 1.4 shows both ideal gas and real gas assumption designs for the same inlet condition. As it can be seen using an ideal-gas model leads to a much smaller nozzle length in comparison with real-gas model even for same exit Mach number. To this extent, a deep understanding of the non-ideal and non-classical gas behavior is of the major importance for the improvement of better component design and performance analysis for engineering applications such as ORC cycle and sCO_2 cycle.

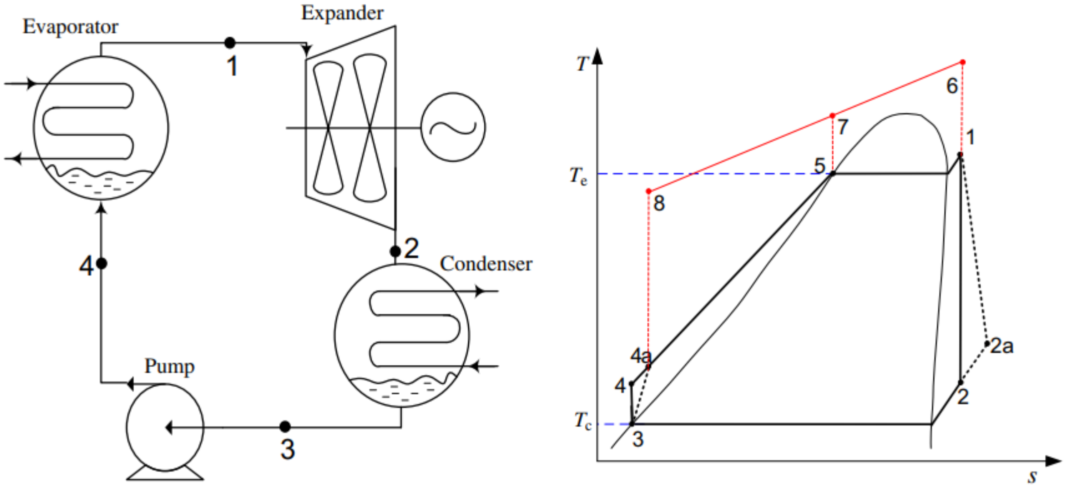

Figure 1.3: Simple ORC: (a) schematic diagram; (b) T-s diagram[22]

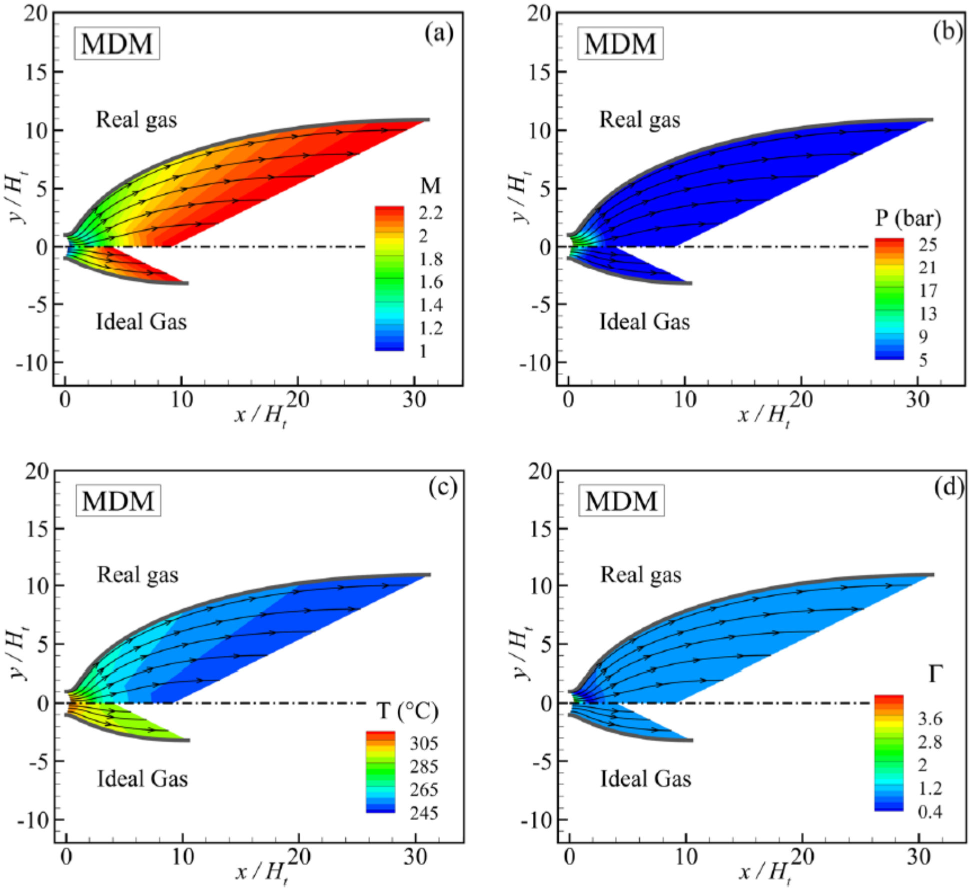

Figure 1.4: The effect of the real-gas law on the nozzle geometry [23] (M: Mach number, P: Pressure, T: Temperature, Γ: Fundamental derivative of gas dynamics).

1.2 Literature Review on Non-classical Gas Dynamics

Thompson[20] introduced a thermodynamic quantity and called it the fundamental derivative,

$$\Gamma = \frac{c^4}{2v^3}\left(\frac{\partial^2 v}{\partial p^2}\right)_s \tag{1.1}$$

In the above expression, v is the specific volume, p is the pressure, c is the speed of sound and s is the specific entropy. It is often referred to as the curvature of isentropes. The crucial effects of the fundamental derivative on the behaviour of compressible fluids was discussed in Thompson's paper. The fundamental derivative plays a central role in the qualitative behaviour of the fluid flow in many contexts including shock waves, expansion fans, gas dynamic relations such as between Mach number and cross-sectional area ratio in one-dimensional isentropic flow. Manipulation of derivatives shows that the following form is equivalent to the original definition of fundamental derivative:

$$\Gamma = 1 + \rho c\left(\frac{\partial c}{\partial p}\right)_s \tag{1.2}$$

where ρ is the density of the fluid. The above expression shows that the fundamental derivative also represents a measure of the variation of sound speed with respect to pressure in an isentropic process. Conventional treatises of gasdynamics assume, either explicitly or implicitly, that $\Gamma > 1$. This is the case for a perfect gas, which gives $\Gamma = \frac{\gamma+1}{2}$, where γ is the ratio of the isobaric heat capacity and isochoric heat capacity. Though fluid in this region shows a significant departure from a dilute gas due to the large density, but no qualitatively difference appears in the region of $\Gamma > 1$, e.g. shock wave is still of compression type. When $0 < \Gamma \leq 1$, shock waves are still of the ordinary compression type but the sound speed no longer increases with pressure upon isentropic compression, this may result in the non-classical behavior of Mach number increase across oblique shock waves[24]. The most impressive phenomenon appears in the regime of $\Gamma < 0$, where expansion shocks are admissible so that the flow can be suddenly accelerated through a discontinuous surface, i.e., an expansion shock. Such gas dynamical phenomena in the negative fundamental region are often referred to as non-classical gas dynamics behaviour. The classification of the gas based on Γ can be found in table 1.2

Γ	classification
$\Gamma > 1$	classical gas
$1 > \Gamma > 0$	classical non-ideal gas
$\Gamma < 0$	non-classical gas

Table 1.2: Classification of gas based on Γ

Bethe[25] first investigated the possibility of forming an expansion shock in a single-phase vapour. His work indicated an expansion shock was possible only when the specific heat at constant volume $\frac{c_v}{R}$ is greater than 17.5, which he considered impossible for a real fluid. Zel'dovich[26] explored the possibility of such fluids and reached the same conclusion. Thompson and Lambrakis[27] also provided theoretical evidence for the existence of such fluids and listed a few candidate fluids such as $C_{11}F_{22}$. These candidate fluids have finite negative fundamental derivative regions in the neighboring of the critical point and the liquid-vapour saturated line due to the molecular complexity and inter-molecular forces[21]. The family of fluids that exhibit negative isentrope curvature is referred to as the Bethe-Zel'dovich-Thompson(BZT) fluid, named after the three scientists who first explored the existence of such fluids. More BZT fluids were presented in the recent studies[28] including siloxanes, a working fluid that is currently used in organic Rankine cycle engines. These literature supporting the existence of BZT fluids set the stage for the research of understanding the non-classical gas behaviour of BZT fluids.

Dense gas effects were taken into consideration in nozzle flow analyses a long time ago at the beginning of the last century by Callendar[29]. Recent studies focused more on non-ideal gas flow and its application. Sullivan[30] provided a review and comparison of five isentrope equations: the polytrope, Walker, Van der Waals, Rayleigh, and Callendar models. The historical development and limitation of each model were discussed. Arp et al.[31] attempted to find the occurrence of the Gruneisen parameter which relates thermodynamic properties to lattice vibrational spectra and has long been used in equations of state for solids[32]. Leung and Epstein[33] focused on one-dimensional isentropic flow and developed a generalized critical flow model for the non-ideal gas flow. By adopting the Redlich-Kwong (R-K) equation of state, their computation results for various common gases were compared with Johnson's work[34] as well as the experimental data. Bober and Chow[35] did numerical computation on the convergent-divergent nozzle and obtained a method for one-dimensional non-ideal gas flow by applying the R-K equation of state. They used methane gas as the working fluid and gave the plots of pressure, temperature, and area ratios as functions of Mach number. More recently, Sirignano [36][37] discussed the real-gas modifications for compressible flow at high pressures and analyzed normal compressive shock wave with supercritical upstream thermodynamic conditions using the SRK model. Calculation results for some common gases including argon, nitrogen, and carbon dioxide were presented.

In the past decades, the need of understanding the non-classical gas dynamics has led to construction of experimental facilities. A number of experimental studies have been done on exploring the non-classical gas behavior in the dense gas region and to demonstrate the existence of rarefaction shock wave. Borisov [38] first used Freon-13 to produce the rarefaction shock wave near the gas critical liquid-vapour point. To confirm that the rarefaction shock wave is an unique phenomenon that can only occur in the gas critical region, experiments using Freon-13 far away from the critical point and nitrogen were also performed to provide a comparison. Kutateladze, Nakoryakov, and Borisov [39] later compared the experimental data with calculated results and ascribed this non-classical phenomenon to the abnormal adiabats in the critical region. However, others have questioned whether the observed wave was caused by anomalous behavior of the test gas at or very near the critical point, rather than a true expansion shock [40][41]. Fergason [42] later designed a dense gas shock tube and used a single copper diaphragm to initiate each experimental trial. The experiment aimed at the generation of a non-classical rarefaction shock in fluid $PP10$. However, no rarefaction was captured and they concluded that the diaphragm opening time affects the experiments significantly.

Figure 1.5: Picture of FAST [43].

At TU Delft, researchers conducted experiments with dense gases. The Flexible Asymmetric Shock Tube (FAST), a Ludwieg tube, was developed to investigate the wave velocity of dense vapor [44]. Measurements are carried out on the Test Rig for Organic Vapors (TROVA) at the Politecnico di Milano's compressible fluid dynamics for renewable energy applications laboratory (CREA) . The TROVA is a revolutionary blow down wind tunnel that was designed and used for non-ideal compressible fluid studies and the detection of non-classical effects of expanding flows [45]. Spinelli obtained first results for the linear siloxane fluid MDM in the non-ideal thermodynamic zone. Although non-classical effects have not been observed at this moment, a lot of promising preliminary results are obtained for future research [46][47].

Even though the non-classical phenomena in a single-phase flow can rarely be obtained experimentally, there are several numerical studies on it based on the numerical schemes to solve the Euler equations for dense gas. Unlike the standard numerical scheme for solving classical compressible Euler equations, the dense gas cases are more complex due to the existence of mixed waves. For example, the numerical dissipation operator in an artificial viscosity method needs to be reconsidered. Argrow [48] introduced a TVD predictor-corrector (TVD-MacCormack) scheme to solve the one-dimensional Euler equations for Van der Waals gas. The symmetric boundary conditions were applied, and results showed that the reflections observed at the shock tube end walls for a dense gas are much more complex than regular gases. Evaluation of more refined Equation of States (EOS) are also needed to cover the shortcomings of the Van der Waals model. Aldo and Argrow [49] [50] developed a method of characteristics (MOC) for two-dimensional (planar) and axisymmetric flow of a Van der Waals gas, and tried to employ this method into the design of minimum length nozzles (MLN). Following Argrow's studies, Brown and Argrow [51] [52] [53] extended the TVDM method to the computation of two-dimensional non-classical flows under the Martin–Hou equation of state. Discussions on the wave field structures and thermodynamic states for a dense gas flow were presented. Fergason and Argrow [54] then extended its application also into the simulations of two-dimensional viscous flow for nonclassical gases by solving the two-dimensional planar Navier Stokes equations. Displacement thicknesses were quantified and analyzed. Guardone, Selmin, and Vigevano [55], Guardone and Vigevano [56] extended the widely used Roe linearization method for the ideal gas to the polytropic Van der Waals gas.

Researchers have attempted to investigate the BZT gasdynamic behaviors in the organic Rankine cycle engine. As discussed above, BZT fluids have showed many unconventional phenomena near the liquid–vapor critical point, such as expansion shock waves, compression isentropic fans, splitting shocks, etc. The generation of shock waves is one of the major losses in the organic Rankine cycle engines. Applying the BZT fluids in the organic Rankine cycle engines may significantly reduce the shock-related losses (both the wave drag from shocks and losses from boundary-layer separation due to shock reflections) and enable the design of supersonic shock-free turbine cascades. Brown and Argrow [53] simulated the cascade flow using PP10 ($C_{13}H_{22}$), a proposed BZT fluid, as working fluid and compared the simulation results with using Toluene (C_7H_8). All performance parameters for the PP10 cascade flow were enhanced. Wheeler and Ong [57] proposed a new method for the design of nozzles operating with dense gases and ran a two-dimensional simulation to determine the turbine performance. Results showed that the turbine efficiency is highly dependent on the choice of working fluid.

Besides single component fluids, some non-conventional gas behaviors of multi-component fluids have also been discussed. Different from the mixtures of ideal gases, the molecular interactions between different molecules play an important role here, and the thermodynamic properties of dense vapors of multi-component mixtures are no longer linear functions of the mole fractions of each compound. Colonna and Silva [58] presented the procedure to evaluate the equation of state for highly non-ideal mixtures, and the fundamental derivative for Siloxanes. Angelino and Invernizzi [59] showed the experimental results on the thermal stability of siloxane mixtures. Guardone et al.[60] did a review on the non-classical gas dynamics of mixtures, and showed numerical simulations of a supersonic expansion by using mixtures of siloxanes and perfluorocarbons. They also gave the conclusion that the mixing compounds of the same fluid family does not enhance the non-classical gas dynamic phenomena for the considered mixtures.

The objective of this dissertation is as follow:

- Mapping out non-classical region and qualitatively study the non-classical wave phenomena using Van der Waals equation of state.

- Understand the non-ideal and non-classical gas behavior of dense gas quasi one dimensional flow.

- Develop an acurate real gas numerical solver using Jameson-Schmidt-Turkel (JST) scheme.

- Numerically investigate the peculiar gas behavior of dense gas in unsteady (Shock Tube) and steady (ramp/wedge) flow.

1.3 Outline of Research

This dissertation is structured as follows.

In Chapter 2, several real gas models including Van der Waals, Soave Redlich Kwong and Peng Robinson model, are discussed. Dense gas candidates' properties are reported and are used to compare the effect of molecular complexity on the BZT gas region. The fundamental derivative Γ is calculated and plotted using a real gas model.

In Chapter 3, Unconventional gas behaviors of the isentropic quasi-1D nozzle flow have been investigated systematically and in depth for a typical BZT gas. The result show that for a given upstream states of expansion shock, there exist a maximum mach number for expansion shock solution to exist.

In Chapter 4, The necessary conditions for the formation of non-classical wave are examined. Jump relation and entropy condition are reviewed. Results are reported for expansion shock, double sonic shock and Prandtl Meyer relations, where the Van der Waals equation of state is used.

In Chapter 5, a numerical solver using JST scheme is described and is extended to handle arbitrary gas model. The considered solver is verified against simple flow configurations for which it is possible to compute the analytic solution. Then, different test cases are investigated using this solver to compare the classical and non-classical gas behavior of BZT gas. Results show that, for a flow over the compression corners, as Mach number increases, the wave structure transients first from a centered compression fan to a compression fan-shock and finally to a single compression shock.

Chapter 2

Non-Ideal Gas and Dense Gas

2.1 Thermodynamic Modeling

In this chapter, thermodynamics for real gas and ideal gas are reviewed. Three Γ regions are mapped using Van der Waals equations of state. Properties of BZT gas candidates are presented and discussed. A region with $\Gamma < 0$ is located near the saturation vapor line. The size of the non-classical region are found to be closely related to the molecular comlexity of the fluid.

The thermodynamic state of a generic system is uniquely determined by n state variables. $X_i, i = 1, 2, \cdots, n$, according to classical thermodynamics. The generic relation used to determine a dependent state variable Y is called the equation of state (EOS),

$$Y = Y(X_1, X_2, ..., X_n) \tag{2.1}$$

For a single-component fluid in thermodynamic equilibrium, the thermodynamic state can be determined by two independent intensive state variables,

$$Y = Y(X_1, X_2) \tag{2.2}$$

It is often written as

$$F(p, \rho, T) = 0 \tag{2.3}$$

where ρ is density, T is temperature and p is pressure.

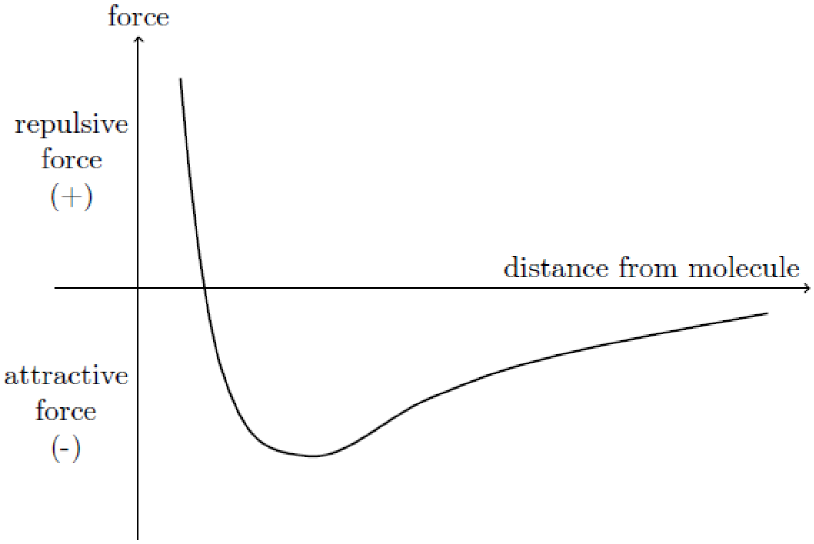

Figure 2.1: Qualitative representation of the variation of the intermolecular force of a single molecule with distance [61]

A fluid can be imagined as a collection of molecules moving at random and interacting with one another. Each molecule is surrounded by a force field created by the electromagnetic action of the molecule's electrons and nuclei. This force field is known as the inter-molecular force because it governs the interaction of molecules. In figure 2.1, a qualitative representation of the variation of a single molecule's inter-molecular force with distance is given. The force is strongly repulsive at small distances, tending to push molecules apart, but the inter-molecular force rapidly declines with distance, eventually becoming a modest attractive force. The magnitude of the inter-molecular force is insignificant at a distance of around 10 molecular diameters from the molecule. Inter-molecular forces influence molecular movements, which influences the macroscopic thermodynamic properties of the fluid. They must be taken into account in actual gases.

For many problems in aerodynamics the assumption of ideal gas is very accurate and simplifies the mathematical treatment of the Navier-Stokes equations. This assumption is valid especially at pressures well below the critical pressure and temperatures well above the critical temperature, where inter-molecular forces have little effect on molecular mobility and hence on the macroscopic features of the system. The idea gas law is given by

$$p = \rho R T \tag{2.4}$$

where R is the specific gas constant formed as the ratio of the universal gas constant and the molecular weight of the gas in question $R = \Re/M$. For a thermally perfect gas, it can be demonstrated mathematically and experimentally that internal energy and enthalpy is a function of temperature only

$$e = e(T) \tag{2.5}$$

$$h = h(T) = e(T) + \frac{p}{\rho} \tag{2.6}$$

The heat capacity at constant volume and that at constant pressure are defined, respectively, as below

$$c_v = \left(\frac{\partial e}{\partial T}\right)_v \tag{2.7}$$

$$c_p = \left(\frac{\partial h}{\partial T}\right)_p \tag{2.8}$$

A further simplification can be achieved by assuming constant heat capacities, reducing the caloric equation of state for the internal energy and enthalpy to

$$e = c_v T \tag{2.9}$$

$$h = c_p T \tag{2.10}$$

$$\tag{2.11}$$

Introduction of the heat capacity ratio $\gamma = c_p/c_v$ allows combining the above equations and perfect gas law into the single caloric equation of state for an ideal gas

$$p = (\gamma - 1)\rho e \tag{2.12}$$

As previously discussed, this ideal gas assumption, giving a simple relation between pressure, density and internal energy, is very convenient in numerically solving the Navier-Stokes equation. Thus, it is widely used in a lot of numerical solvers. However, this assumption breaks down whenever inter-molecular forces are not negligible. This is quite common in the Organic Rankine Cycle when the fluid is operated near the critical point and the saturated vapor region. The deviation of real gas effects from idea gas law can be seen by defining compressibility factor Z given by

$$Z = \frac{p}{\rho R T} \tag{2.13}$$

For ideal gas, $Z = 1$. However, Z only gives the magnitude of the deviation. There are two additional state variables that determine the relative change in specific volume with respect to pressure at constant temperature β_T (isothermal compressibility) and with respect to temperature at constant pressure β_p (isobaric compressibility). The definitions of these properties and their expressions for an ideal gas are summarized in Table 2.1.

Property	Definition	Ideal Gas
Compressibility Factor	$Z = f(T,P)$	Z =1
Isothermal compressibility	$\beta_T = -\frac{1}{v}\left(\frac{\partial v}{\partial p}\right)_T = \frac{1}{p} - \frac{1}{Z}\left(\frac{\partial Z}{\partial p}\right)_T$	$\beta_T = \frac{1}{p}$
Isobaric compressibility	$\beta_p = \frac{1}{v}\left(\frac{\partial v}{\partial T}\right)_p = \frac{1}{T} + \frac{1}{Z}\left(\frac{\partial Z}{\partial T}\right)_p$	$\beta_p = \frac{1}{T}$

Table 2.1: Compressibility functions for real gas

When dealing with ideal fluids, these state variables are usually disregarded due to their trivial formulation, but they must be accounted for in many thermodynamic relations for real gases.

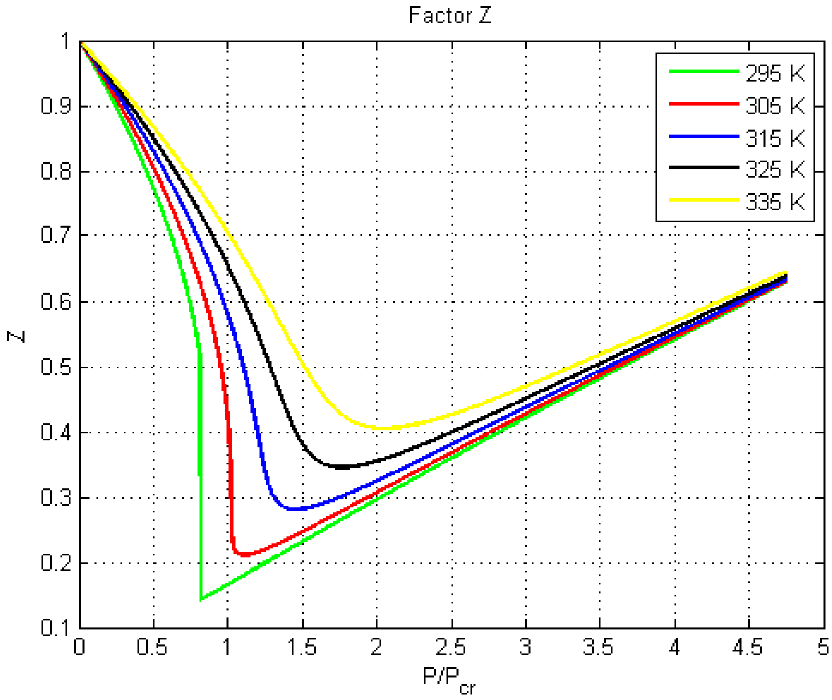

Figure 2.2: Compressibility factor of CO_2 near critical point with SRK model

The compressibility factor Z predicted by Soave Redlich Kwong gas model is plotted in Figure 2.2. Z increases with temperature increase at any given pressure because the interaction between molecules decreases. When pressure approaches the critical value, Z is far away from unity (ideal gas), which means the gas behavior deviates most from ideal gas behavior. This further indicates the importance of using a more comprehensive equation of state. Three real gas equation of states are discussed in this chapter.

2.1.1 Departure Function for Real Fluid

A significant difference between a real gas and an ideal gas is that enthalpy is a function of both pressure and temperature.

$$dh = \left(\frac{\partial h}{\partial T}\right)_p dT + \left(\frac{\partial h}{\partial p}\right)_T dp \tag{2.14}$$

By definition $c_p = \left(\frac{\partial h}{\partial T}\right)_p$, while the second partial derivative can be rewritten using the Maxwell relations, shown in Appendix B, as

$$\left(\frac{\partial h}{\partial p}\right)_T = v - T\left(\frac{\partial v}{\partial T}\right)_p \tag{2.15}$$

Substituting the expressions for the two derivatives in Eq 2.14 yields

$$dh = c_p dT + \left[v - T\left(\frac{\partial v}{\partial T}\right)_p\right] dp \tag{2.16}$$

The internal energy and entropy can also be expressed in terms of $u(T, v)$ and $s(p, T)$

$$du = \left(\frac{\partial u}{\partial T}\right)_v dT + \left(\frac{\partial u}{\partial v}\right)_T dv \tag{2.17}$$

$$ds = \left(\frac{\partial s}{\partial T}\right)_p dT + \left(\frac{\partial s}{\partial p}\right)_T dp \tag{2.18}$$

Applying appropriate Maxwell relations, Eq 2.17 and 2.18 can be rewritten as

$$du = c_v dT + \left[T\left(\frac{\partial p}{\partial T}\right)_v - p\right] dv \tag{2.19}$$

$$ds = c_v \frac{dT}{T} + \left(\frac{\partial P}{\partial T}\right)_v dv \tag{2.20}$$

Equations 2.17, 2.19, and 2.20 provide convenient general relations for computing enthalpy, internal energy and entropy changes as function of volumetric properties and specific heats.

If a fluid is described with a suitable EOS, these equations may be conveniently integrated to obtain analytical expressions for energy and entropy.

2.1.2 Van der Waals Equation of State

In 1873, van der Waals [62] proposed a modification to the ideal gas pressure equation of state, $p(v, T) = RT/v$, to take into account repulsive and attractive forces. It is referred to as the van der Waals equation of state EOS

$$p(T, v) = \frac{RT}{v - b} - \frac{a}{v^2}, \tag{2.21}$$

where the constants a and b have positive values representing the characteristic of the individual gas. The constant a is a measure of the average attraction between particles. The constant b is the volume excluded by a mole of particles. The van der Waals equation of state approaches ideal gas equation of state when temperature is high and pressure is low. These constants can be expressed in terms of critical quantities as follows:

$$a = \frac{27}{64}\frac{R^2 T_c^2}{p_c}, \quad b = \frac{1}{8}\frac{RT_c}{p_c} \tag{2.22}$$

The Van der Waals EoS is often expressed in polynomial form

$$Z^3 - (1 + B)Z^2 + AZ - AB = 0 \tag{2.23}$$

where

$$Z = \frac{pv}{RT}, \qquad A = \frac{pa}{(RT)^2}, \qquad B = \frac{pb}{RT}$$

Here the coefficients A and B are non-dimensional parameters related to intermolecular attraction and repulsion, respectively. For a perfect gas, $A = B = 0$. The value of these coefficients can reflect how far a real gas deviates from the ideal-gas behavior. With polytropic assumption, the internal energy and entropy can be expressed as follows:

$$e(T, v) = e_{ref} + c_v(T - T_{ref}) - \frac{a}{v} \tag{2.24}$$

$$s(T, v) = s_{ref} + c_v ln(\frac{T}{T_{ref}}) + Rln(\frac{v - b}{v_{ref} - b}) \tag{2.25}$$

2.1.3 Soave-Redlich-Kwong Equation of State

Otto Redlich and Joseph Neng Shun Kwong [63] formulated a new equation of state, known as Redlich-Kwong equation of state, that is generally more accurate than the van der Waals equation and the ideal gas equation at temperatures above the critical temperature. Soave [17] later introduced a modification to the Redlich-Kwong EOS to improve its performances in the representation of the vapor pressure of pure substances. The modification consists of introducing a third dimensionless parameter w, called the acentric factor, defined as

$$w = -log_{10}\frac{p_{sat}(T = 0.7T_c)}{p_c} - 1 \tag{2.26}$$

where $p = p_{sat}$ is the vapor pressure at the vapor-liquid phase change. The acentric factor w represents a measure of the molecular complexity with respect to both the geometry and the polarity and of its manifestation at the macroscopic thermodynamic level [64]. The SRK EoS for a single-component fluid is given by

$$p(T, v) = \frac{RT}{v - b} - \frac{a}{(v^2 + bv)\sqrt{T}} \tag{2.27}$$

or it can be written as a cubic equation form

$$Z^3 - Z^2 + (A - B - B^2)Z - AB = 0 \tag{2.28}$$

where

$$\begin{aligned}
Z \equiv& \frac{pv}{R_u T} = \frac{p}{\rho R_u T} && (2.29)\\
A \equiv& \frac{ap}{(R_u T)^2} && (2.30)\\
B \equiv& \frac{bp}{R_u T} && (2.31)\\
a \equiv& 0.42748 \frac{(R_u T_c)^2}{p_c}\left[1 + S(1 - T_r^{0.5})\right]^2 && (2.32)\\
b \equiv& 0.08664 \frac{R_u T_c}{p_c} && (2.33)\\
T_r \equiv& \frac{T}{T_c} && (2.34)\\
S \equiv& 0.48508 + 1.5517\omega - 0.15613\omega^2 && (2.35)
\end{aligned}$$

R and R_u are the specific and universal gas constants, respectively. Subscript c denotes a thermodynamic critical value. The coefficients a and b (and therefor A and B) relate respectively to inter-molecular attraction and repulsion force. For the SRK model, by applying Eq 2.16, the enthalpy[65] is given by

$$h = h_i + \frac{1}{W}\left[R_u T(Z-1) + \frac{T(da/dT) - a}{b} ln \frac{Z+B}{Z}\right] \tag{2.36}$$

Sirignano [66] derived further for the calculation of enthalpy, entropy and speed of sound using the SRK model

$$h = c_p T + \left[(Z-1)RT + \frac{\tilde{a}}{bW}(S+1)\left[S\sqrt{\frac{T}{T_c}} - (S+1)\right] ln \frac{Z+B}{Z}\right] \tag{2.37}$$

where

$$\tilde{a} \equiv 0.42748\frac{(R_uT_c)^2}{p_c} \tag{2.38}$$

$$T\frac{da}{dT} = \tilde{a}\left[S^2\frac{T}{T_c} - S(S+1)\sqrt{\frac{T}{T_c}}\right] \tag{2.39}$$

$$T^2\frac{d^2a}{dT^2} = \frac{\tilde{a}S(S+1)}{2}\sqrt{\frac{T}{T_c}} \tag{2.40}$$

$$A \equiv \frac{ap}{(R_uT)^2} = \frac{\tilde{a}p}{(R_uT)^2}\left[(S+1)^2 - 2S(1+S)\sqrt{\frac{T}{T_c}} + S^2\frac{T}{T_c}\right] \tag{2.41}$$

$$A' \equiv \frac{p}{(R_uT)^2}T\frac{da}{dT} = \frac{AT}{a}\frac{da}{dT} = \frac{\tilde{a}p}{(R_uT)^2}\left[S^2\sqrt{\frac{T}{T_c}} - S(S+1)\sqrt{\frac{T}{T_c}}\right] \tag{2.42}$$

$$A' - A = \frac{\tilde{a}p}{(R_uT)^2}(S+1)\left[S\sqrt{\frac{T}{T_c}} - (S+1)\right] \tag{2.43}$$

$$A' \equiv \frac{AT^2}{a}\frac{d^2a}{dT^2} = \frac{\tilde{a}p}{(R_uT)^2}\frac{S(S+1)}{2}\sqrt{\frac{T}{T_c}} \tag{2.44}$$

The entropy change can be calculated by

$$\Delta s = \Delta s_i + R\left(ln\frac{Z_2 - B_2}{Z_1 - B_1} + \frac{A_1'}{B_1}ln\frac{Z_1}{Z_1 + B_1} - \frac{A_2'}{B_2}ln\frac{Z_2}{Z_2 + B_2}\right) \tag{2.45}$$

$$c \equiv \sqrt{\left(\frac{\partial p}{\partial \rho}\right)_s} = \sqrt{\frac{ZR_uT}{W}(f + g\beta)} \tag{2.46}$$

where f,g, κ and β is

$$f \equiv \frac{2Z^3 - Z^2 + AB}{Z^3 - B^2Z} \tag{2.47}$$

$$g \equiv \frac{1}{Z - B} - \frac{A'}{Z(Z + B)} \tag{2.48}$$

$$\beta \equiv \frac{(\gamma - 1)Zg}{1 + \kappa/c_v} \tag{2.49}$$

$$\kappa \equiv c_v(\gamma - 1)\frac{A''}{B}ln\left(\frac{Z + B}{Z}\right) \tag{2.50}$$

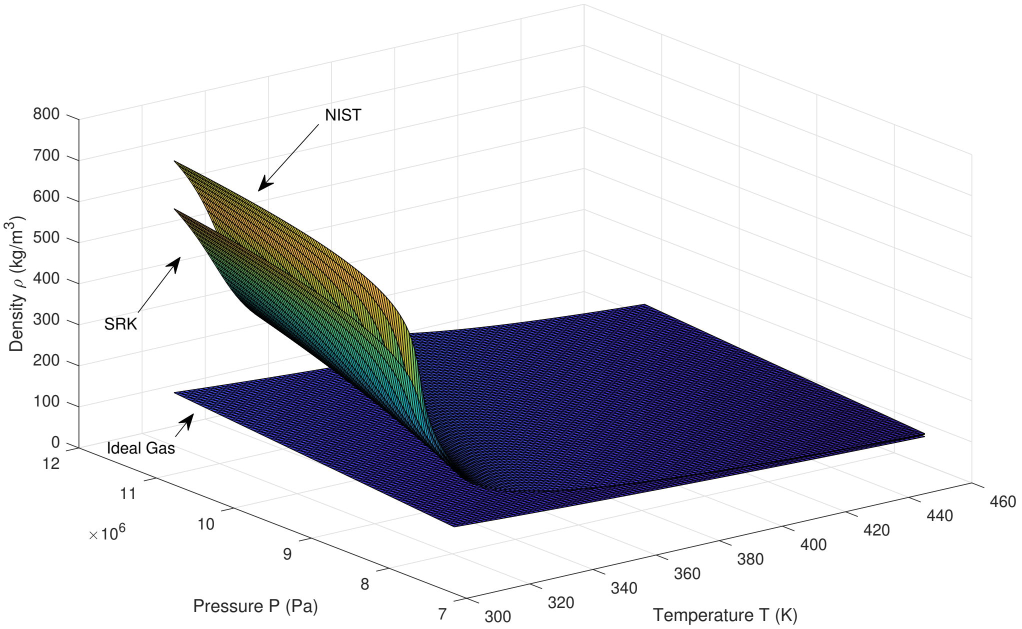

Figure 2.3: Density comparison between NIST, SRK and ideal gas for CO_2

Fig 2.3 compares density of different models. In the visualized range, the density in the ideal gas EoS shows a huge deviation from other models. The main difference between the SRK model and NIST (National Institute of Standards and Technology) data occurs near critical temperature, though they capture the same trend.

2.1.4 Peng Robinson Equation of State

In 1976, Peng and Robinson presented their model[19]. They improved the prediction of liquid density values, vapor pressures, and equilibrium ratios by modifying the SRK EoS. The Peng-Robinson (PR) model can be conveniently written as

$$p(T, v) = \frac{RT}{v - b} - \frac{a}{v^2 - 2bv - b^2} \tag{2.51}$$

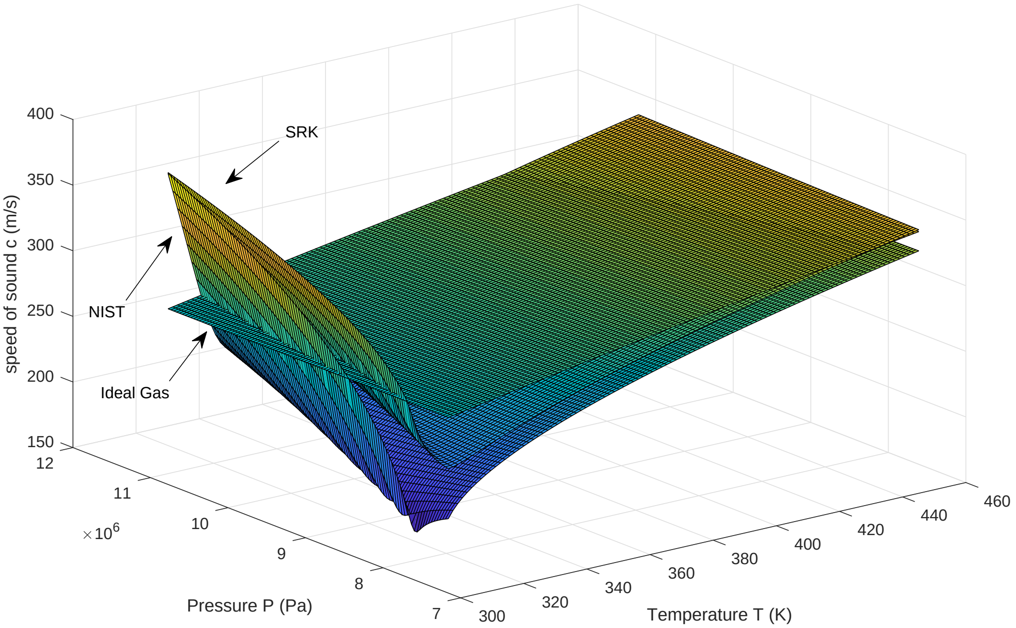

Figure 2.4: Speed of sound comparison between NIST, SRK and ideal gas

where

$$a \equiv 0.45724 \frac{(R_u T_c)^2}{p_c} \left[1 + S(1 - T_r^{0.5})\right]^2 \tag{2.52}$$

$$b \equiv 0.0778 \frac{R_u T_c}{p_c} \tag{2.53}$$

$$T_r \equiv \frac{T}{T_c} \tag{2.54}$$

$$S \equiv 0.37464 + 1.54226\omega - 0.26992\omega^2 \tag{2.55}$$

2.2 Fundamental Derivative

As discussed in Chapter 1, a parameter called fundamental derivative is used to identify the dynamics of compressible-fluid flows, it is defined as

$$\Gamma = \frac{c^4}{2v^3}\left(\frac{\partial^2 v}{\partial p^2}\right)_s, \tag{2.56}$$

where c is the speed of sound

$$c^2 = \left(\frac{\partial p}{\partial \rho}\right)_s. \tag{2.57}$$

With proper thermodynamic relations, it can also be expressed in 3 other forms as

$$\Gamma = \frac{v^3}{2c^2}\left(\frac{\partial^2 p}{\partial v^2}\right)_s \tag{2.58}$$

$$\Gamma = \frac{1}{c}\left(\frac{\partial \rho c}{\partial \rho}\right)_s = 1 - \frac{v}{c}\left(\frac{\partial c}{\partial v}\right)_s \tag{2.59}$$

$$\Gamma = 1 + \frac{c}{v}\left(\frac{\partial c}{\partial p}\right)_s \tag{2.60}$$

Classical gasdynamics theory implicitly assumes that $\Gamma > 1$. It can be proved that $\Gamma = (\gamma + 1)/2$ with the ideal gas model. Therefore, it is always a constant larger than 1. From the qualitative point of view, gas with $\Gamma > 1$ resembles the gasdynamics behavior of the ideal gas [67]. Studies [20][68] also showed there exists fluids endowed with a non-ideal gasdynamic behavior in a finite vapor-phase region, in the vicinity of the saturation curve and critical point. In this region, Γ is less than unity and can even go to negative. Fluid with $\Gamma < 0$ and fluid with $0 < \Gamma < 1$ behave qualitatively differently. Equation (2.60) indicates that, unlike an ideal gas, the speed of sound increases with pressure on isentropic compressions for both fluid with $0 < \Gamma < 1$ and $\Gamma < 0$. Equation (2.56) shows that the fundamental derivative is directly related to the term $\left(\frac{\partial^2 v}{\partial p^2}\right)_s$, which is also known as the curvature of isentrope. The isentrope is concave up for fluid with a positive Γ and is concave down for fluid with a negative Γ as shown in Figure 2.5. Thompson[69] showed that the peculiar gas behavior such as expansion shock only occurs in fluid with negative Γ. It then can be concluded that the speed of sound decreases on isentropic compression is a necessary but not sufficient condition for nonclassical gasdynamic phenomena to occur.

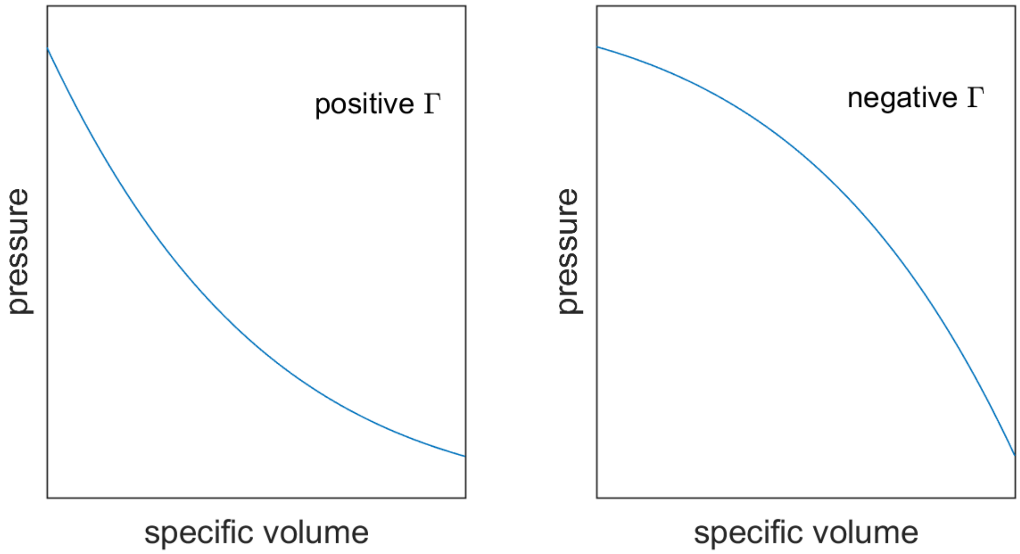

Figure 2.5: Sign of the fundamental derivative

Therefore, Γ can be used to identify the regime of the flow as shown in Table 2.2.

Table 2.2: Classification of flow regime based on the value of Γ

value of Γ	Region name
$\Gamma > 1$	ideal regime
$1 > \Gamma > 0$	non-ideal regime
$\Gamma < 0$	non-classical regime

By applying thermodynamic equations and Maxwell relation, Bethe[70] gave an alternative expression for Γ by using v and T as the independent thermodynamic state variables

$$\Gamma(T,v) = \frac{v^3}{2c^2}\left[\frac{\partial^2 p}{\partial v^2} - \frac{3T}{c_v}\frac{\partial p}{\partial T}\frac{\partial^2 p}{\partial T \partial v} + \left(\frac{T}{c_v}\frac{\partial p}{\partial T}\right)^2 \left[\frac{3}{T}\frac{\partial c_v}{\partial v} + \frac{1}{T}\frac{\partial p}{\partial T}\left(1 - \frac{T}{c_v}\frac{\partial c_v}{\partial T}\right)\right]\right] \tag{2.61}$$

this equation provides a convenient way to calculate the value of Γ by using the equation of state directly. In the present study, Γ is computed with the Van der Waals gas model for MDM fluid (Octamethyltrisiloxane, $C_8H_{24}O_2Si_3$). The results are plotted in Figure 2.6 where the saturation curve, contour line of $\Gamma = 0$ and contour line of $\Gamma = 1$ are plotted. Three regions including $\Gamma < 0$, $0 < \Gamma < 1$, and $1 < \Gamma$ are marked in the Figure. It can be seen that $\Gamma < 0$ region is very close to the saturation vapor line.

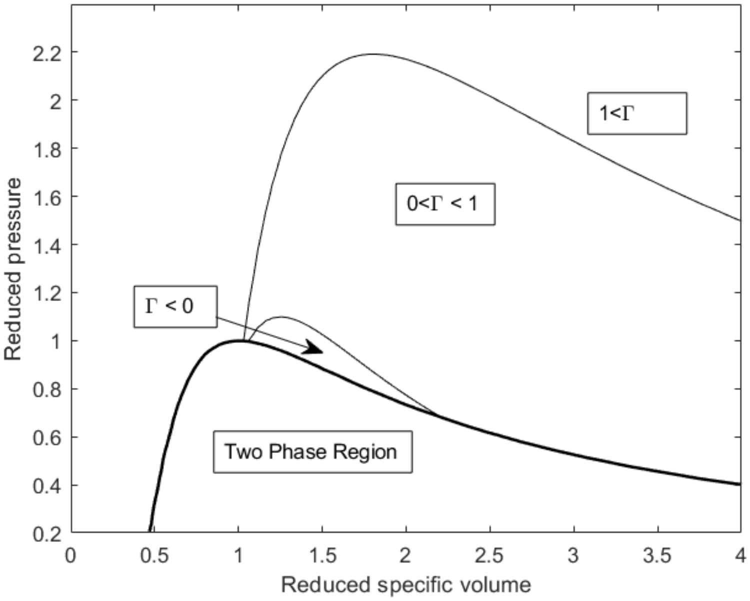

Figure 2.6: p-v diagram of a fluid featuring a non-ideal region. The liquid-vapor saturation curve (bold line) and the Γ= 1 and Γ = 0 contour lines are plotted;

In Figure 2.7, an isentrope of MDM is plotted in the $p - v$ diagram. The isentrope starts from classical region with a concave up curvature and then cross into the non-classical region with a concave down curvature.

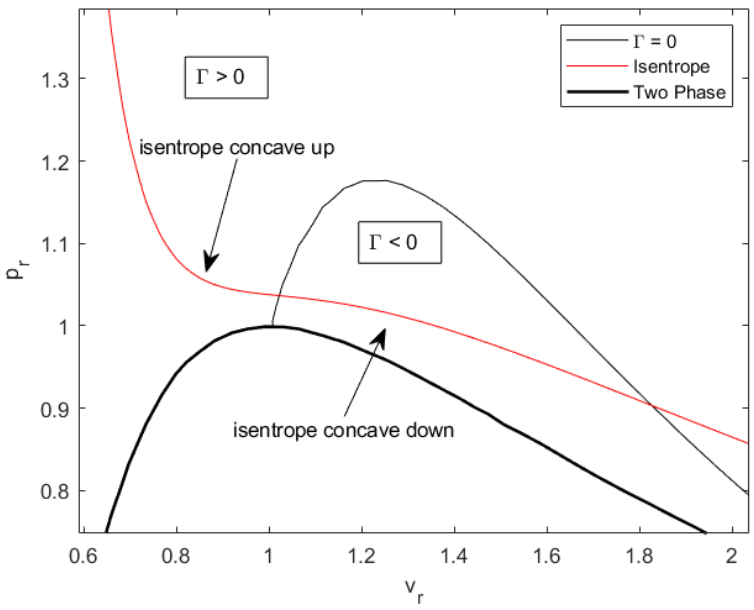

Figure 2.7: isentrope of MDM on p-v diagram

2.3 Properties of Dense Gas Candidates

The regular gases usually do not have a negative fundamental derivative region, because negative Γ requires gases of high molecular complexity. Earlier researchers had doubts about the existence of the so-called BZT gas and the related non-classical gas behavior. Examples of BZT fluids have been identified for certain heavy hydrocarbons and some methylsiloxanes[71]. More BZT fluids were presented in the recent studies[28] including siloxanes, a working fluid that is currently used in organic Rankine cycle engines. Thermodynamic properties of selected siloxanes and fluorinated fluid are provided in Table 2.3

In the present work, a compound gas named Octamethyltrisiloxane (also called MDM) is chosen as the working fluid. It is an organosilicon compound with the formula $C_8H_{24}O_2Si_3$. Organometallics are useful reagents, catalysts, and precursor materials with applications in thin film deposition, industrial chemistry, pharmaceuticals, LED manufacturing, and others. The chemical structure of MDM is shown in Figure 2.8. [72]

Name	Chemical Formula	$M(g/mol)$	$T_c(K)$	$p_c(kPa)$	Z_c	$T_b(K)$	$\frac{c_v}{R}$	w
PP series								
$PP10$	$C_{13}F_{22}$	574	630.2	1614.5	0.2859	467	78.37	0.4833
$PP25$	$C_{17}F_{30}$	774	673.6	1149.0	0.2500	533.15	123.0	0.7157
Siloxanes								
MDM	$C_8H_{24}O_2Si_3$	236.53	564.1	1415.2	0.278	425.7	57.96	0.530
MD_2M	$C_{10}H_{30}O_3Si_4$	310.69	599.4	1179.4	0.283	467.4		0.650

Table 2.3: Chemical formulas, molecular weight M, critical pressure p_c, critical temperature T_c, and critical compressibility factor Z_c for fluorinated and siloxanes substances [68][28].

(a) 2D view

(b) 3D view

Figure 2.8: Chemical structure of $C_8H_{24}O_2Si_3$

Figure 2.9 shows the non-classical region computed with the Van der Waals model. It can be seen in Figure 2.9a the maximum reduced pressure of the MDM non-classical region is $p_r = 1.09$ while the maximum reduced pressure of the $PP10$ non-classical region is $p_r = 1.13$ in Figure 2.9b. This comparison shows that fluids with more complex molecular structure tends to have a larger non-classical region.

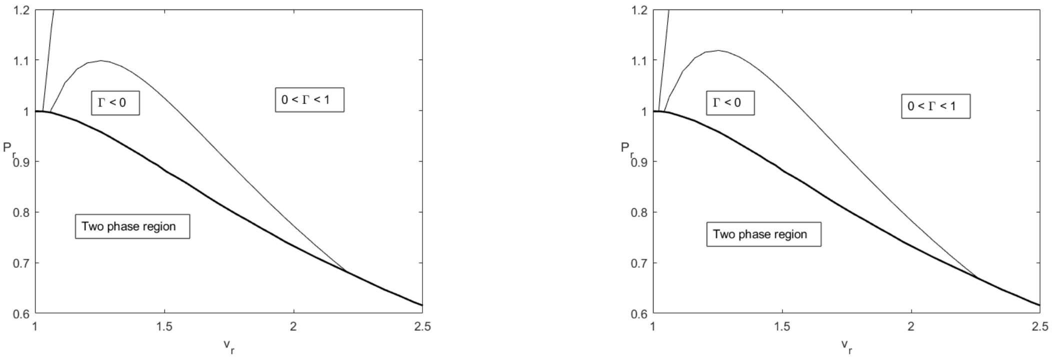

(a)

(b)

Figure 2.9: Non-classical region with the Van der Waals EOS (a) MDM (b) PP10 (Saturation vapor line are calculated by numerically solving the system equations of equal chemical potential and equal temperature at the vapor and liquid side)

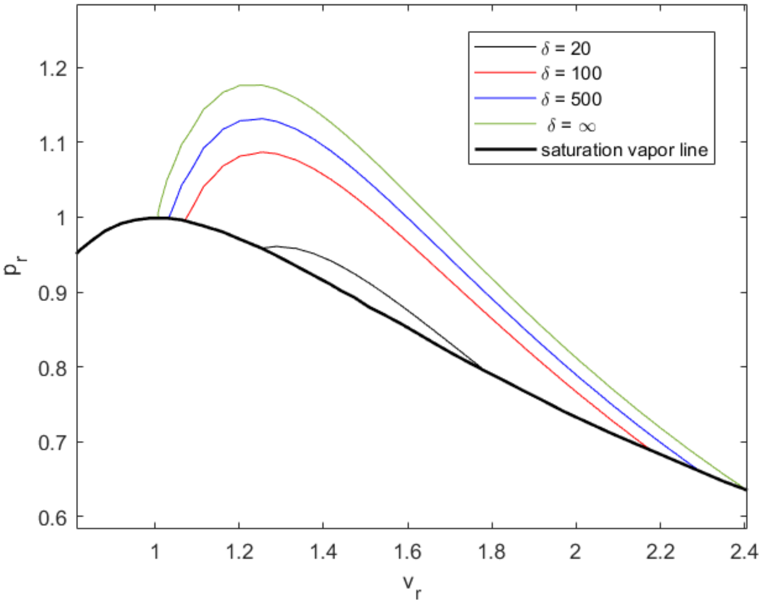

Figure 2.10: Negative Γ region for a Van der Waals fluid with different δ

In Figure 2.10, the non-classical regions are plotted for substances with different δ, where $\delta = c_v/R$. As δ increases, the area of the non-classical region increases. But when δ is sufficiently large, there exist a limit that the non-classical region can reach as shown by the green line in the Figure 2.10. When $\delta < 17$, the non-classical region disappears. This is also confirmed in Thompson's work [73].

Chapter 3

Quasi-1D Isentropic Flow of BZT Gas

Previous studies has shown that for a flow with $\Gamma < 0$, a divergent-convergent nozzle is required to accelerate it from subsonic to supersonic[20]. However, this is only valid when the entire flow-field is completely in the region $\Gamma < 0$. For a fluid from region of $\Gamma < 1$ to the region of $\Gamma < 0$ or cross the entire region of $\Gamma < 0$, a divergent-convergent may not be enough to expand the fluid from subsonic to supersonic [74]. In this chapter, relations between Mach number, velocity and cross-sectional area in quasi-1D flow will be examined in details. A more detailed analysis of the nozzle geometry and the variation of corresponding thermodynamic properties will be carried out for different inlet conditions.

3.1 Differential Form of Conservation Laws

Quasi-one-dimensional (Q1D) flow means that the flow properties change only in the direction of the flow and there are no transverse variations in the flow properties. In practical terms, a necessary (but not sufficient) condition for using the Q1D relations is that the channel cross-sectional area has gradual variations. This simplification is quite helpful and leads us to some interesting results.

Consider flow through a channel in which the flow direction is taken as x and has a cross-sectional area $A(x)$. A mono-component, single-phase fluid flows isentropically through this channel. The conservation equations of mass, momentum, and energy are:

$$\begin{cases} \dfrac{d\rho}{\rho} + \dfrac{du}{u} + \dfrac{dA}{A} = 0 \\ \rho u du + dp = 0 \\ dh + udu = 0 \end{cases} \tag{3.1}$$

Equation (3.1) is the general form of conservation laws for isentropic Q1D flow. All the analyses for unconventional gas behavior in the present work are based on these equations. Rewriting Eq. (3.1) with expressions from former sections gives the following statements. Momentum conservation

$$\rho u du + dp = 0 \tag{3.2}$$

$$\rho u du + \left(\frac{\partial p}{\partial \rho}\right)_T d\rho + \left(\frac{\partial p}{\partial T}\right)_\rho dT = 0 \tag{3.3}$$

Energy conservation

$$dh + udu = 0 \tag{3.4}$$

$$c_p dT + \left[v - T\left(\frac{\partial v}{\partial T}\right)_p\right] dp + udu = 0 \tag{3.5}$$

In practical conditions, the upstream and the downstream pressure of the channel will be given in most cases. To keep consistency with that, here the pressure is selected as the independent variable and all the other variables will be written in terms of dp.

First of all, the velocity difference can be derived from Eq. (3.2) directly

$$\frac{du}{dp} = -\frac{1}{\rho u} \tag{3.6}$$

The temperature difference regarding pressure is then given by Eq. (3.5)

$$\frac{dT}{dp} = \frac{T}{c_p}\left(\frac{\partial v}{\partial T}\right)_p \tag{3.7}$$

Once the temperature equation is obtained, substitute it into the following expression of dp

$$dp = \left(\frac{\partial p}{\partial \rho}\right)_T d\rho + \left(\frac{\partial p}{\partial T}\right)_\rho dT \tag{3.8}$$

which leads to the expression of density change with pressure

$$\frac{d\rho}{dp} = \frac{1 - \frac{T}{c_p}\left(\frac{\partial p}{\partial T}\right)_\rho \left(\frac{\partial v}{\partial T}\right)_p}{\left(\frac{\partial p}{\partial \rho}\right)_T} \tag{3.9}$$

So far, the ordinary differential equation system for quasi-1D nozzle flow calculation is obtained:

$$\begin{cases} \dfrac{du}{dp} = -\dfrac{1}{\rho u} \\ \dfrac{dT}{dp} = \dfrac{T}{c_p}\left(\dfrac{\partial v}{\partial T}\right)_p \\ \dfrac{d\rho}{dp} = \dfrac{1 - \dfrac{T}{c_p}\left(\dfrac{\partial p}{\partial T}\right)_\rho \left(\dfrac{\partial v}{\partial T}\right)_p}{\left(\dfrac{\partial p}{\partial \rho}\right)_T} \end{cases} \tag{3.10}$$

To determine the local Mach number at each point, recall the Mach number-velocity relation, Eq. (3.15)

$$\frac{du}{u} = \frac{1}{1 + (\Gamma - 1)M^2} \frac{dM}{M}$$

The Mach number variation versus pressure is obtained by combining Eq. (3.15) with Eq. (3.6), which gives

$$\frac{dM}{dp} = -M(1 + (\Gamma - 1)M^2)\frac{1}{\rho u^2} \tag{3.11}$$

3.2 Non-classical Behavior of a BZT Gas in Quasi-1D Flow

To show the differences between conventional and unconventional gas behavior more clearly, several channel cases are computed. The gas MDM introduced previously is selected as the working fluid in the computation. By judicially choosing the initial conditions, there are some sections within the channel where the fundamental derivative may become negative.

Section 3.2.4 and section 3.2.5 examine two isentropic flow cases starting from the same thermodynamic state $p_{in} = 1.1p_c, v_{in} = 0.8v_c$, one with an initial subsonic speed $M = 0.5$ and the other with supersonic speed $M = 3.0$. The inlet point is chosen to be as close to the critical point. In this way, the isentropic process we examine will have a segment that falls within the negative fundamental derivative region and then stay in the $\Gamma < 1$ region until the nozzle outlet. Both cases show interesting results which are opposite to the conventional behavior. For comparison with the flow behavior of an ideal gas, results computed based on the ideal gas law with properties specified at the initial inlet conditions are also presented.

3.2.1 Mach - Velocity Relation

Consider an inviscid isentropic flow through a channel of cross-sectional area $A(x)$, where x represents the flow direction. The conservation of momentum is given as

$$\rho u du + dp = 0 \tag{3.12}$$

Combine it with the definition of the fundamental derivative

$$\Gamma = 1 + \frac{c}{v}\left(\frac{\partial c}{\partial p}\right)_s \tag{3.13}$$

which gives $vdp = \dfrac{cdc}{\Gamma - 1}$. Substituting the above into Eq. (3.12) yields

$$udu + \frac{cdc}{\Gamma - 1} = 0 \tag{3.14}$$

In the ideal gas situation, we are familiar with the result that as a flow accelerates its temperature and sound speed decrease monotonically. Equation (3.14) re-states this result for the ideal gas but reveals the opposite behavior for a real gas with $\Gamma < 1$, as shown in Table 3.1. For a real gas with $\Gamma < 1$, the sound speed increases as the flow accelerates downstream.

Table 3.1: Speed of sound - Velocity relation related to Γ

Γ	Gas Behavior
$\Gamma > 1$	speed of sound decreases with u increasing
$\Gamma < 1$	speed of sound increases with u increasing

Let $M = u/c$, substitute M into the equation above and simplify the result.

$$\begin{aligned} dM &= \frac{1}{c}du - \frac{u}{c^2}dc \\ \frac{dc}{c} &= \frac{du}{u} - \frac{dM}{M} \\ udu &+ \frac{c^2}{\Gamma - 1}\left(\frac{du}{u} - \frac{dM}{M}\right) = 0 \end{aligned}$$

Then, the relation between velocity and Mach number is

$$\frac{du}{u} = \frac{1}{1 + (\Gamma - 1)M^2}\frac{dM}{M} \tag{3.15}$$

Equation (3.15) shows how the Mach number would be changed with velocity. For any classical gas with $\Gamma > 1$, Mach number always increases with the velocity monotonically. But for a non-classical gas when Γ goes below 1, the change of Mach number would be depending on the sign of the term $1 + (\Gamma - 1)M^2$. When $M^2 < \frac{1}{1 - \Gamma}$, Mach number still increases with velocity like how it behaves in the classical gas case. Otherwise, if $M^2 > \frac{1}{1 - \Gamma}$, Mach number will decrease with velocity and therefore show some non-classical properties.

Table 3.2: Mach - Velocity relation related to Γ

Γ	Gas Behavior
$\Gamma > 1$	M increases monotonically with u
$\Gamma < 1$	M increases with u only for $M^2 < \frac{1}{1 - \Gamma}$

3.2.2 Mach - Area Relation

Classical theory has established a complete system for quasi-1D nozzle flow. Consider a quasi-1D isentropic flow, the velocity-area relation is given as

$$\frac{1}{u}\frac{du}{dx} = \frac{M^2-1}{A}\frac{dA}{dx} \tag{3.16}$$

Substituting Eq. (3.16) into Eq. (3.15), the relation between Mach number and area change is

$$\frac{1}{M}\frac{dM}{dx} = \frac{1+(\Gamma-1)M^2}{M^2-1}\frac{1}{A}\frac{dA}{dx} \tag{3.17}$$

Equation (3.17) states that the transition between subsonic and supersonic flow only occurs when $\frac{dA}{dx} = 0$, and how the Mach number changes regarding to area ratio is related to the sign of $(1+(\Gamma-1)M^2)/(M^2-1)$. Conventionally, along with the increasing cross-sectional area ratio, the Mach number increases in a supersonic flow and decreases in a subsonic flow. But for non-classical gas cases, there are some different gas behaviors shown below.

Figure 3.1 maps out four regions where $\frac{dM}{dA}$ changes sign in the (M,Γ) domain. In regions ① and ② where $M^2 < \frac{1}{1-\Gamma}$, the flow behaves the same way as the classical theory predicts. A converging channel accelerates a subsonic flow ($\frac{dM}{dA} < 0$) and decelerates a supersonic flow ($\frac{dM}{dA} > 0$). In regions ③ and ④ however, the flow behaves in complete opposite way to a conventional gas. A diverging channel accelerates a subsonic flow ($\frac{dM}{dA} > 0$) and decelerates a supersonic flow ($\frac{dM}{dA} < 0$). It is clear then that in order to accelerate a subsonic flow from subsonic to supersonic flow, or decelerate a supersonic flow to subsonic flow smoothly, one has to use a diverging-converging channel. To investigate the flow properties at the transonic point, the second-order derivative with respect to area ratio change needs to be derived from

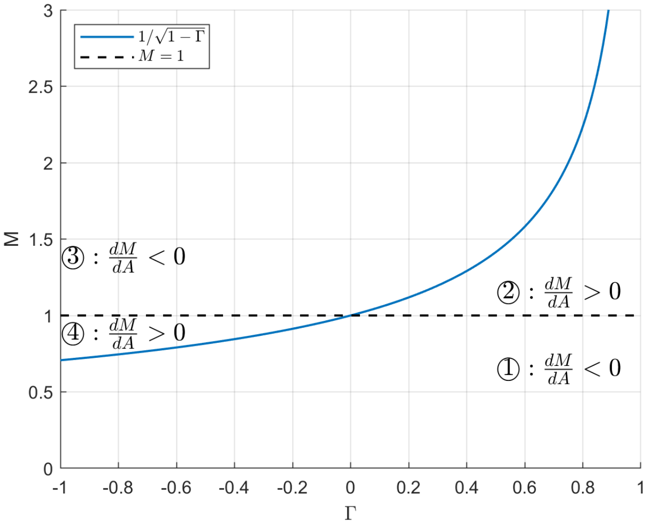

Figure 3.1: Mach number - Area relation related to Γ (for Γ < 1)

Eq. (3.17). To avoid the singularity value at transonic point $M = 1$, apply $L'Hospital's$ rule to Eq. (3.17)

$$\lim_{M\to 1} \frac{dM}{dx} = \lim_{M\to 1} \frac{\frac{d}{dx}\left[(1+(\Gamma-1)M^2)\,\frac{M}{A}\frac{dA}{dx}\right]}{\frac{d}{dx}\left[M^2-1\right]} \tag{3.18}$$

When $M \to 1$, $\dfrac{dA}{dx} \to 0$, so

$$\lim_{M\to 1} \frac{dM}{dx} = \lim_{M\to 1} \frac{1+(\Gamma-1)M^2}{2A\frac{dM}{dx}} \frac{d^2A}{dx^2} = \frac{\Gamma}{2A\frac{dM}{dx}} \frac{d^2A}{dx^2} \tag{3.19}$$

Rearrange the equation

$$\left(\frac{dM}{dx}\right)^2 = \frac{\Gamma}{2A}\frac{d^2A}{dx^2} \tag{3.20}$$

The LHS of Eq. (3.20) is always non-negative. So, for gases with Γ greater than 0, the sonic point has the minimum cross-sectional area. However, when Γ goes smaller than 0, the cross-sectional area will have the maximum value at the sonic point. Instead of the classical convergent-divergent nozzle, here a divergent-convergent nozzle will be needed for non-classical gas transonic flow.

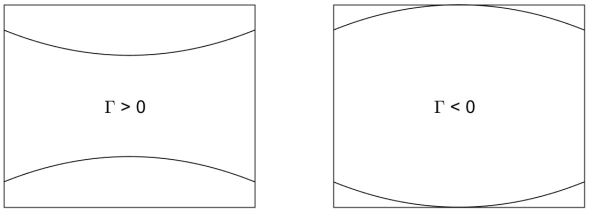

Figure 3.2: Transonic nozzle related to Γ

3.2.3 General Differential Equations for Quasi-One-Dimensional Isentropic Flow

From previous discussions, the equations needed for numerical computation are summarized here in table 3.3. All the equations are in differential form.

Table 3.3: Quasi-1D isentropic flow equations for non-conventional gas

Flow Variable	Calculation Formula
pressure	dp is taken as the independent variable
density	$\frac{d\rho}{dp} = \frac{1 - \frac{T}{c_p}\left(\frac{\partial p}{\partial T}\right)_\rho \left(\frac{\partial v}{\partial T}\right)_p}{\left(\frac{\partial p}{\partial \rho}\right)_T}$
temperature	$\frac{dT}{dp} = \frac{T}{c_p}\left(\frac{\partial v}{\partial T}\right)_p$
velocity	$\frac{du}{dp} = -\frac{1}{\rho u}$
cross-sectional area	$\frac{dA}{dp} = A\left(\frac{1}{\rho u^2} - \frac{\left[1 - \frac{T}{c_p}\left(\frac{\partial p}{\partial T}\right)_\rho \left(\frac{\partial v}{\partial T}\right)_p\right]}{\rho\left(\frac{\partial p}{\partial \rho}\right)_T}\right)$
Mach number	$\frac{dM}{dp} = -M(1 + (\Gamma - 1)M^2)\frac{1}{\rho u^2}$
Enthalpy	$dh = c_p dT + \left[v - T\left(\frac{\partial v}{\partial T}\right)_p\right] dp$
Specific Heat	$c_p - c_v = T\left(\frac{\partial v}{\partial T}\right)_p \left(\frac{\partial p}{\partial T}\right)_v$
Fundamental Derivative	$\Gamma(T, v) = \frac{v^3}{2c^2}\left[\frac{\partial^2 p}{\partial v^2} - \frac{3T}{c_v}\frac{\partial p}{\partial T}\frac{\partial^2 p}{\partial T \partial v} + \left(\frac{T}{c_v}\frac{\partial p}{\partial T}\right)^2 \left[3\frac{\partial^2 p}{\partial T^2} + \frac{1}{T}\frac{\partial p}{\partial T}\left(1 - \frac{T}{c_v}\frac{\partial p}{\partial T}\right)\right]\right]$

This system of ODEs can be easily integrated numerically by a Runge-Kutta method with a uniform pressure increment of $dp = 10^{-4} p_c$ between each interval. Vieta's formulas[75] are used to solve the EoS defined in Eq. (2.23).

3.2.4 Isentropic Flow with Subsonic Inlet Condition

Consider the flow in a nozzle with a specified continuously decreasing pressure profile. The needed cross-sectional area change is to be determined based on the pressure change. The flow starts at the initial static condition $p = 1.1p_c$ and $v = 0.8v_c$ and at a Mach number $M = 0.5$. The isentropic expansion process is plotted in the p-v diagram in Figure 3.3

together with the vapor dome and the $\Gamma = 0$ and 1 boundaries. The starting point is chosen to be slightly above the critical point and close to the vapor dome so that the isentrope goes through longer segment in the negative fundamental derivative region.

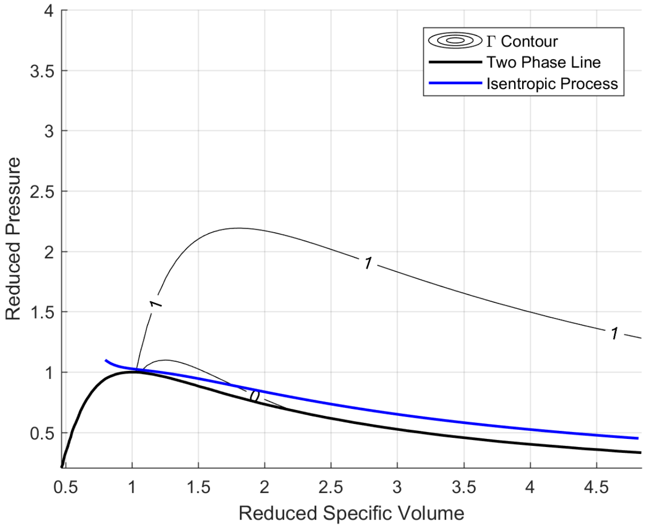

Figure 3.3: Case 1: $p_{in} = 1.1p_c, M_{in} = 0.5, v_{in} = 0.8v_c$

The fundamental derivative is a thermodynamic property of the gas along with temperature and sound speed. Therefore, they are uniquely determined as functions of pressure and specific volume only and can be calculated along the isentrope by using isentropic thermodynamic relations without integrating the ODEs for the flow. To facilitate the visualization of the flow behavior of the gas that accomplishes such an isentropic expansion process in a 1D channel, the pressure variation along the channel is specified as a parabolic function along the flow direction as shown in figure 3.4a. Figure 3.4b shows the change of the fundamental derivative with the static pressure. Γ is in the conventional regime at $p_r = 1.1$ and then turns to drop rapidly when the pressure starts to decrease. This drop happens close to the critical point in the p-v diagram when the isentrope goes across multiple Γ contour lines so that Γ first drops below 1.0 and continues to drop below 0 until $\Gamma \approx -1$ before it recovers gradually back to Γ close to 1, but still below 1. It achieves its minimum value when the pressure equals the critical pressure of the gas. It looks like that Γ keeps staying in the $\Gamma < 1$ region forever until the nozzle outlet. One may ask if the isentrope can cross the $\Gamma = 1$ boundary. The answer is 'Yes'. Γ will eventually go greater than 1 if the gas is going to be expanded to a super low pressure at the nozzle outlet. Based on our computation results, it requires the outlet pressure to be hundreds of times smaller than the inlet pressure.

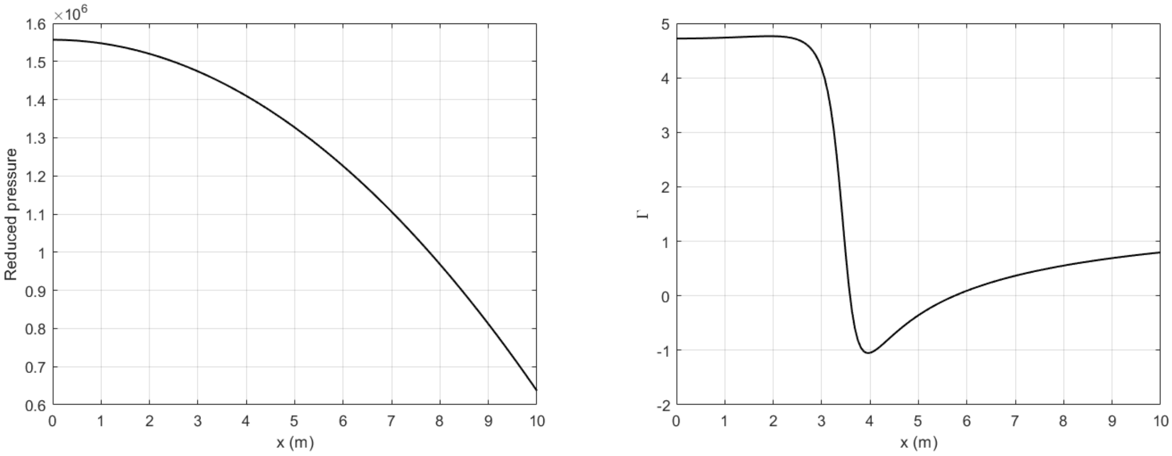

(a) Pressure Profile (b) Fundamental Derivative

Figure 3.4: Variation of pressure and fundamental derivative along channel for Case 1

Figure 3.5 shows how temperature changes along the isentrope. The initial temperature by using the ideal gas law is very different from that by the Van der Waals model. Both the Van der Waals model and the ideal gas law present a monotonic decrease of temperature as the pressure drops in the isentropic expansion. However, the temperature ratio relative to the initial temperature drops more for the Van der Waals gas than for the ideal gas. This is plotted in figure 3.6a. Figure 3.6b shows the density variations along the channel axis. The density drops also monotonically, but the density by the real gas model drops more than that by the ideal gas law because of the increased sensitivity of pressure on density to account for the finite size of the molecules and the inter-molecular interactions for the real gas at high pressure levels. In terms of the specific volume, the real gas expands more in volume for the same pressure drop. This means more internal energy is converted to kinetic energy of the fluid, resulting in the higher relative temperature drop for the real gas shown in figure 3.6a.

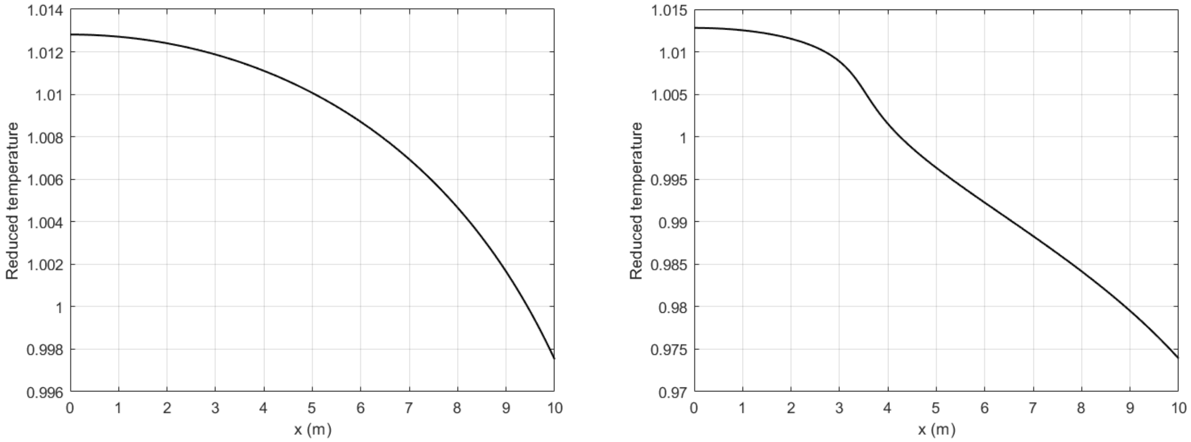

(a) Ideal Gas Model

(b) Van der Waals Gas Model

Figure 3.5: Variation of temperature along channel for Case 1

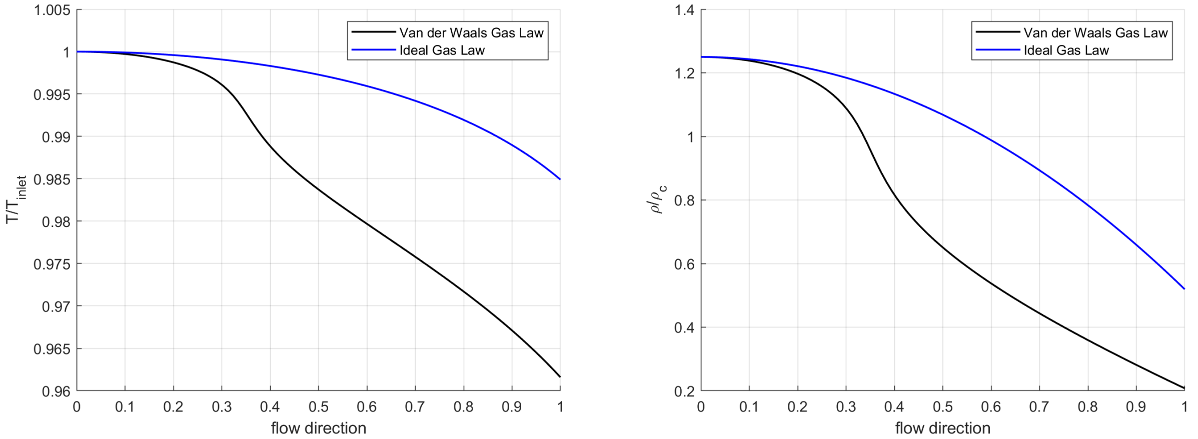

(a) Ideal Gas Model

(b) Van der Waals Gas Model

Figure 3.6: Variation of density along channel for Case 1

Regarding the curvature change of density in the Van der Waals model results, recall the definition of Γ [20], Eq. (1.1)

$$\Gamma = \frac{c^4}{2v^3}\left(\frac{\partial^2 v}{\partial p^2}\right)_s$$

It states that the curvature of the density function is related to the sign of Γ. For an ideal gas, Γ is always a positive number which leads to positive $\left(\frac{\partial^2 v}{\partial p^2}\right)_s$. But for a non-conventional gas, it will cause the density function turning from concave to convex at the $\Gamma = 0$ point.

Figure 3.7a and 3.7b show how the speed of sound changes in the ideal gas and the BZT gas cases, respectively. In the ideal gas case, the speed of sound is a function of temperature only and thus decreases with decreasing pressure monotonically as shown in figure 3.7a. In general, Eq. (3.13) gives the dependence of sound speed on pressure in an isentropic process as

$$\left(\frac{\partial c}{\partial p}\right)_s = \frac{v}{c}(\Gamma - 1)$$

which shows that the sound speed decrease as pressure decreases for $\Gamma > 1$. For a non-conventional gas flow when Γ goes below 1, the speed of sound decreases with increasing pressure, which is opposite to the classical theory. Such is the situation demonstrated in figure 3.7b.

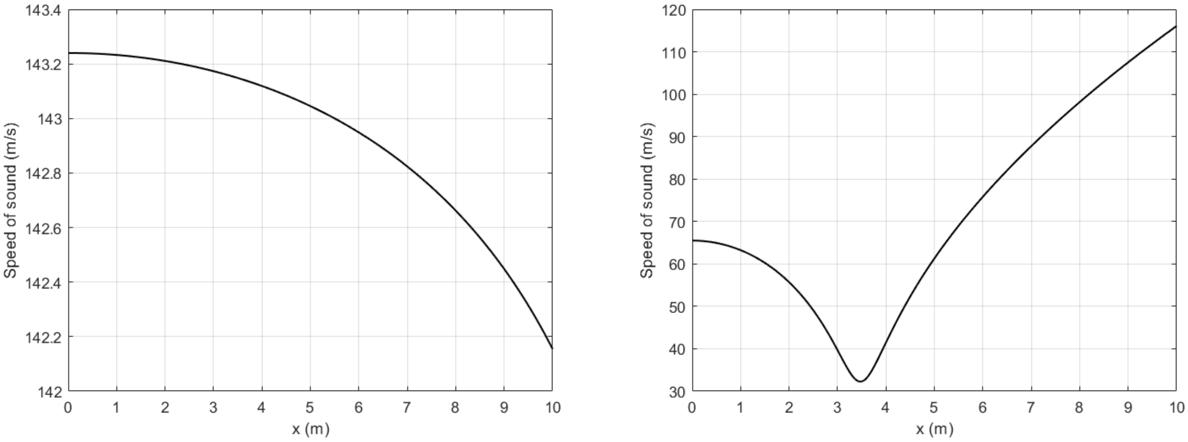

(a) Ideal Gas Model (b) Van der Waals Gas Model

Figure 3.7: Variation of sound speed along channel for Case 1

Figure 3.8 shows the velocity distribution in the nozzle. The velocity increases monotonically along the channel for both the Van der Waals gas and the ideal gas, but the net velocity increase is higher for the real gas than for the ideal gas consistent with the analysis on the higher temperature drop presented earlier. This is because the real gas incurs higher pressure rise as the gas is compressed due to the increased inter-molecular repulsion force, resulting in extra external work needed to compress the gas. In the expansion process, this extra energy stored as internal energy is then released and converted to the additional kinetic energy of the flow.

Also to be noticed is that although the flow Mach number may decrease in part of the expansion process when Γ becomes less than 1.0 as shown in figure 3.10b, the flow velocity, thus the kinetic energy per mass, $u^2/2$, monotonically increase with decreasing pressure as shown in figure 3.8b. The temperature of the gas decreases in the expansion process (see figure 3.5b) as the fluid converts part of its internal energy into its kinetic energy.

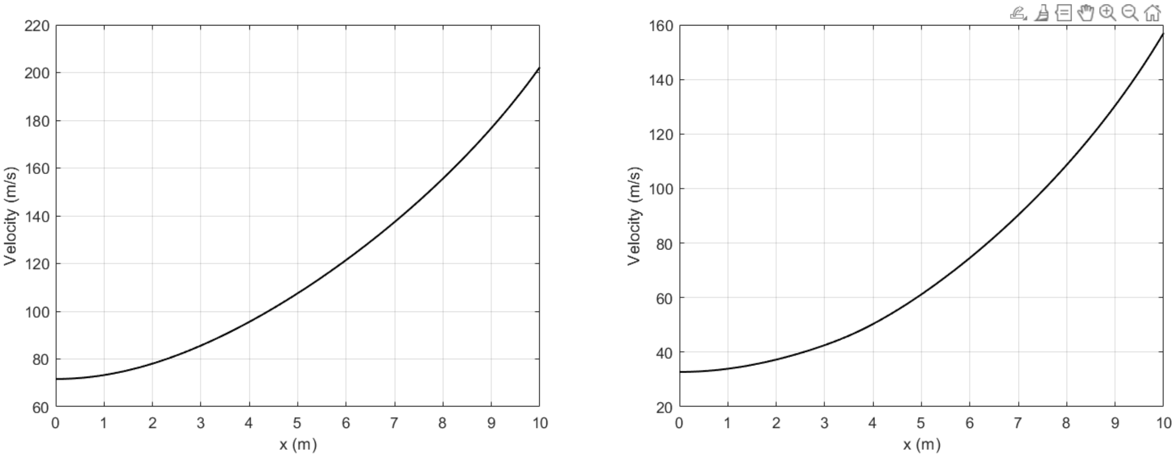

(a) Ideal Gas Model

(b) Van der Waals Gas Model

Figure 3.8: Variation of velocity along channel for Case 1

Figure 3.9a and 3.9b present the difference between the cross-sectional area ratio by using the ideal gas law and the Van der Waals model, while 3.10a and 3.10b give the Mach number comparison. From figure 3.9a and 3.10a it can be found that under the conventional assumption and analysis, a convergent-divergent nozzle is needed for transonic flow, in other words, the nozzle needs a 'throat' to achieve the sonic condition. Mach number is a monotonic function of velocity only. On the contrary, the behavior of the non-classical gas tells a different story. Also when Mach number goes beyond 1, it is not a monotonic function of velocity anymore. Recall equation (3.15)

$$\frac{du}{u} = \frac{1}{1 + (\Gamma - 1)M^2} \frac{dM}{M}$$

This equation states that the Mach number increases monotonically with u when $\Gamma > 1$ and increases with u only for $M^2 < \dfrac{1}{1-\Gamma}$ when $\Gamma < 1$. Figure 3.10b clearly shows that there is an area where Mach number is decreasing with velocity increasing, around $p_r = 0.9$ to $p_r = 1.02$. Within this range, the fundamental derivative is decreasing rapidly while the Mach number doesn't change too much, so M^2 turns to be larger than $\dfrac{1}{1-\Gamma}$.

Instead of using the relation of Mach number and mass flow rate[74], here we put emphasis on the area variation along the flow direction.

$$\left(\frac{dM}{dx}\right)^2 = \frac{\Gamma}{2A}\frac{d^2A}{dx^2}$$

which relates the curvature of the cross-sectional area change to $\frac{dM}{dx}$ for different Γ at $M = 1$. For a conventional gas where $\Gamma > 0$, a converging-diverging throat is needed for the flow to either accelerate from subsonic to supersonic or decelerate from the supersonic to subsonic flow. This is shown in Figure 3.9a and 3.9b. For the real gas case, Γ varies and may going into regions where $\Gamma < 0$. Look at figure 3.9b and figure 3.10b, there are three sonic points in total. The first one and third one have fallen into $\Gamma > 0$ area which leads to the classical convergent-divergent part of the nozzle. The sonic point in the middle is the interesting one. At this point, Γ is smaller than 0. According to Eq. (3.20), a divergent-convergent part will be needed. In figure 3.9b at around $p_r = 0.95$, it is clearly shown that there is a local maximum point corresponding with $M = 1$.

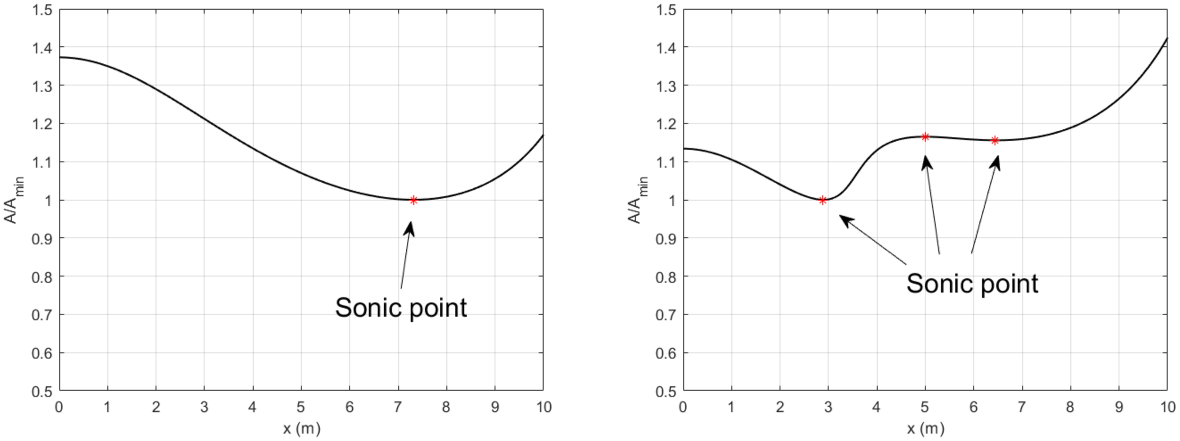

(a) Ideal Gas Model

(b) Van der Waals Gas Model

Figure 3.9: Variation of cross-sectional area ratio along channel for Case 1

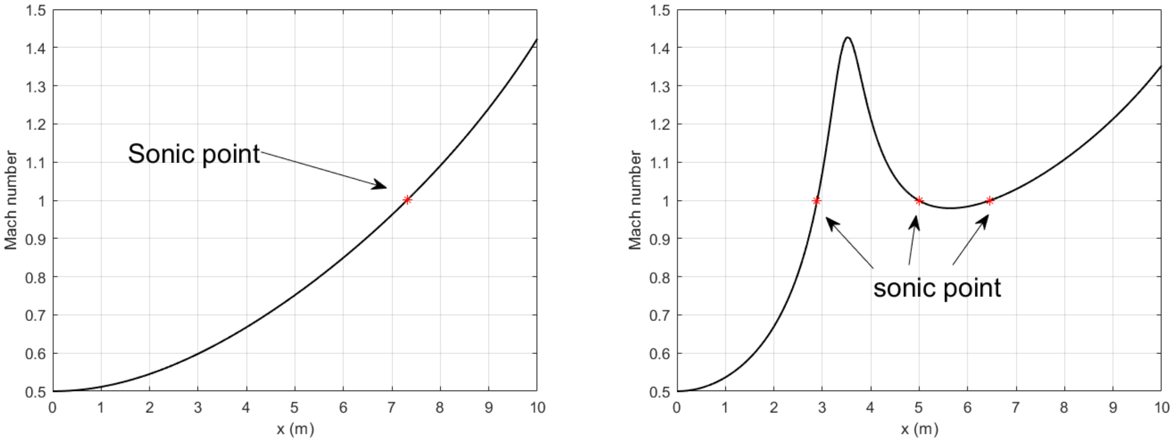

(a) Ideal Gas Model

(b) Van der Waals Gas Model

Figure 3.10: Variation of Mach number along channel for Case 1

3.2.5 Isentropic Flow with Supersonic Inlet Condition

The same upstream thermal conditions and pressure drop profile as in the previous case is imposed but with a supersonic inlet Mach number of 3 is considered in this section. The gas is expanded further, more than the subsonic case until $p = 0.1p_c$. The variables along the channel of the static thermodynamic properties such as Γ, temperature, density, and sound speed are the same as in the previous case for the same specified pressure drop profile in an isentropic expansion. The flow properties such as Mach number (figure 3.11a), cross-sectional area (figure 3.11b), and flow velocity (figure 3.11c) behave very differently compared to the subsonic inlet flow case.

Compared with the subsonic inlet flow case, there is no transonic flow in the supersonic case. Although the Mach number is not a monotonic function of velocity in the unconventional regime and the Mach number at some location in the channel is smaller than the inlet Mach number, the test data shows that the Mach number in a supersonic inlet flow case is never less than 1. As stated above, when $\Gamma < 1$, the Mach number decreases with velocity for $M^2 > \dfrac{1}{1-\Gamma}$. So when the supersonic case and the subsonic case have the same Γ value for the same pressure drop in an isentropic expansion, the supersonic inlet flow case has the larger Mach number at the beginning segment and hence the Mach number turns to decrease earlier in the channel.

In the supersonic inlet flow case, the main differences between the Van der Waals model results and the ideal gas results are given below.

- The Mach number is no longer a monotonic function and it changes a lot along the nozzle. When the isentrope is still in the conventional regime, the Mach number increases faster than the ideal gas case and goes up to larger than 6. Once the isentrope enters the negative fundamental derivative area, Mach number decreases rapidly and later turns to increase again but keeps smaller than the Mach number from the ideal gas law.
- Much larger cross-sectional area ratio is needed to achieve the same pressure drop in quasi-1D flow. Here at the outlet of the nozzle, the area ratio is about two times the ideal gas result.
- While the speed of sound is increasing with decreasing pressure in the non-classical area, the velocity keeps increasing monotonically and grows faster than the ideal gas one.

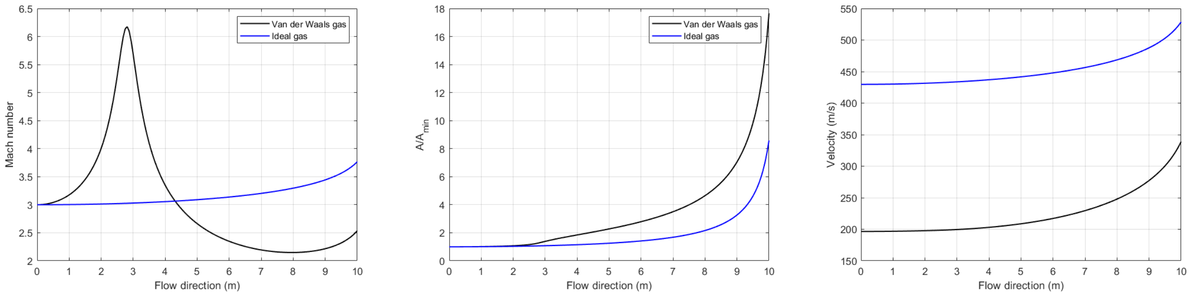

(a) Mach number (b) Cross-sectional area ratio (c) Flow velocity

Figure 3.11: Variation of flow variable along channel for Case 2

In this chapter, unconventional gas behaviors of the isentropic quasi-1D nozzle flow have been investigated systematically and in depth for MDM gas. The flow behavior of a dense gas is significantly different from an ideal gas. For a gas in the region $\Gamma < 1$, the Mach-velocity and area-velocity relations depends on the sign of $M^2 - \frac{1}{1-\Gamma}$. When this value is positive, the flow behaves differently compared to an ideal gas and Mach number may decrease as the flow accelerate. For a subsonic dense gas expansion, there may exist multiple sonic points depending on the upstream condition. However, no experimental data are available to support the theoretical findings as of to date. One major issue could be the difficulty to locate a accurate and correct inlet condition since the flow fields could change dramatically when inlet thermodynamic condition changes for a dense gas. A experiment-based thermodynamic model may be required for a more accurate analysis.

Chapter 4

Wave Phenomenon

In the past decades, a lot of works have been done on proving the existence of BZT gas and understand the non-classical wave phenomena in this region theoretically [20][25][40][76]. In this chapter, the formation of an expansion shock and the non-linear wave propagation in the non-classical region will be reviewed briefly. Using the Van der Waals EOS, jump relation and Prandtl-Meyer relation are solved numerically for MDM in three region including $\Gamma < 0$, $0 < \Gamma < 1$ and $1 < \Gamma$. Results show that, given an incoming flow in the non-classical region, there exists a maximum Mach number M_{max} where an expansion shock can no longer exist when $M > M_{max}$. The value of M_{max} is directly related to the size of the non-classical region. Another finding is that the fluid can jump from non-classical region to classical region through a single expansion shock. Such findings may serve to identify conditions of flow for experimental set up in the effort to prove the existence of expansion shocks experimentally.

Let us first recall the formation of a shock wave in an ideal gas. Consider the initial wave of a pressure pulse traveling in the positive x direction into a stationary gas with properties c_0, p_0, as shown in Figure 4.1. With left running characteristic C^- from the stationary uniform region ahead of the wave, the Riemann invariant J^- remains constant

$$u - \frac{2}{\gamma - 1}c = -\frac{2}{\gamma - 1}c_0 \tag{4.1}$$

which gives

$$u = \frac{2}{\gamma - 1}(c - c_0) \tag{4.2}$$

Any point on the wave advances with constant wave speed

$$u + c = \frac{\gamma + 1}{\gamma - 1}c - \frac{2}{\gamma - 1}c_0 \tag{4.3}$$

The monotonic increase of wave speed with the pressure increase for an idea gas will start to distort the wave shape. Within time Δt, the distance change between any point on the wave and the head of the wave, which travels at constant speed c_0, is

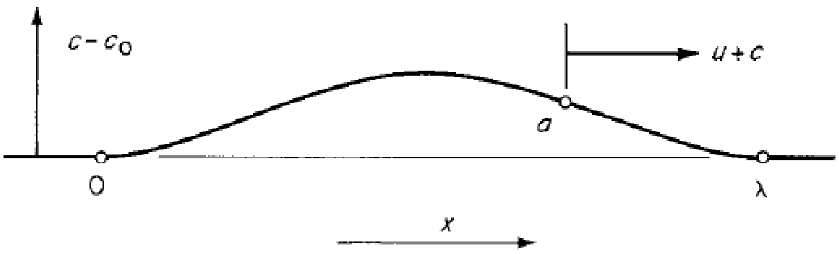

Figure 4.1: Initial wave shape [77]

$$u + c - c_0 = \frac{\gamma + 1}{\gamma - 1}(c - c_0)\Delta t \tag{4.4}$$

The evolution of the wave shape can be plotted for any value of Δt as shown in Figure 4.2. At time $t = t_1$, wave starts to show some distortion, in the form of steepening of the compressive part and spreading of expansive part. Eventually at $t = t_2$, a portion s of the leading edge of the wavefront becomes vertical. The point behind overtakes the point ahead.

This time t_2 is identified as the instant of shock formation. Next, we shall consider how fundamental derivative Γ effects the formation of a shock wave.

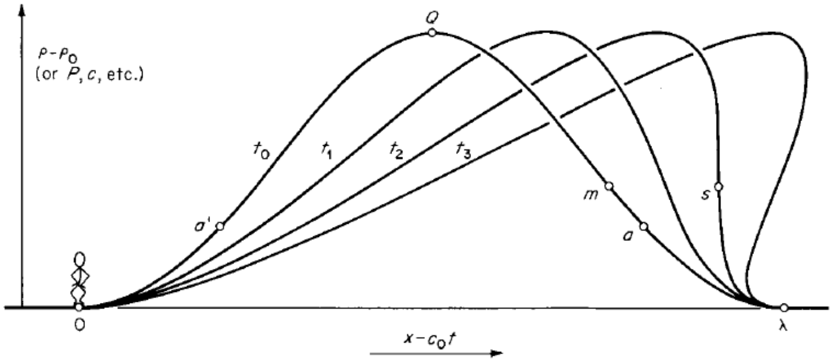

Figure 4.2: Wave distortion at different time instance [77]

For a real gas simple wave as shown in Figure 4.1, the C^+ characteristic will not be parallel anymore. Instead, they will either converge or diverge, and where they intersect a shock will form. As discussed previously, the dependence of wave speed $u + c$ on pressure p will affect the formation of the wave. Consider the differential form of the Riemann invariant on C^-

$$du - \frac{dp}{\rho c} = 0 \tag{4.5}$$

The change of $u + c$ can be expressed as

$$d(u + c) = du + dc = \frac{dp}{\rho c} + dc \tag{4.6}$$

Substitute the following equation into equation 4.6

$$\frac{dp}{\rho c} = c\frac{d\rho}{\rho} = \frac{dc}{\Gamma - 1} \tag{4.7}$$

We get

$$d(u + c) = \Gamma\frac{dp}{\rho c} \tag{4.8}$$

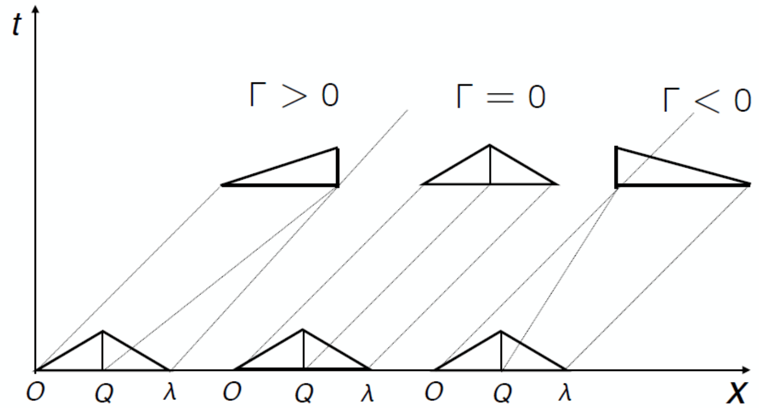

Figure 4.3: Behavior of the wave for various values of the fundamental derivatives Γ

The sign of $d(u+c)$ is the same as the sign of fundamental derivative Γ. Therefore, if $\Gamma > 0$, the compressive part of the wave will steepen and a compression shock will form. If $\Gamma < 0$ the expansive part of the wave will steepen to form an expansion shock. But if $\Gamma = 0$, the wave will stay undistorted. The entropy condition will be discussed in the next section.

4.1 Jump Relations and the Existence of Expansion Shock

In a coordinate system that is moving with the discontinuity, the conservation equations for mass, normal momentum, transverse momentum and energy across the discontinuity can be expressed as follow

$$\rho_1 u_1 = \rho_2 u_2 \tag{4.9}$$

$$\rho_1 u_1^2 + p_1 = \rho_2 u_2^2 + p_2 \tag{4.10}$$

$$v_1 = v_2 \tag{4.11}$$

$$h_1 + \frac{1}{2}u_1^2 = h_2 + \frac{1}{2}u_2^2 \tag{4.12}$$

where u and v are the normal and transverse velocity components, respectively. Subscripts 1 and 2 pertain respectively to conditions on the upstream and downstream sides of the shock. Equation (4.12) can also be written as $h_{t1} = h_{t2}$, where h_t is the total enthalpy. Rearrange equation (4.9),(4.10) and (4.12), the system of equations can be expressed as

$$h_2 - h_1 = \frac{1}{2}(p_2 - p_1)(v_2 + v_1) \tag{4.13}$$

This represents the well-known Rankine-Hugoniot jump relations. The Rankine-Hugoniot relations assume that the tangential velocity and the total enthalpy are constants across shock waves. The above equation determines the thermodynamics states before and after a shockwave. Given upstream states p_1 and v_1, the post-shock state can be defined by the curve $p_2 = \phi(v_2, p_1, v_1)$, which is known as shock adiabat centered on upstream state. Moreover, equations (4.9) and (4.10) may be combined to give

$$-\frac{p_2 - p_1}{v_2 - v_1} = j^2 \tag{4.14}$$

where j is the mass flux. With a given pre-shock state, the above expression defines a straight line referred to as Rayleigh line, named after Lord Rayleigh, that has a negative slope. The intersections between the shock adiabat and the Rayleigh line determines values of the post shock specific volume that satisfy (4.9) to (4.12) . Equation (4.14) contains only thermodynamic quantities. Thus, given a pair of state 1 and state 2 that satisfies Rankine-Hugoniot relations, either state 1 or state 2 can be regarded as pre-shock state. But not all solutions are physically realizable. The jump relations must be supplemented with the second law of thermodynamics to rule out nonphysical solutions, that is, the jump of the specific entropy across a shock wave must not be negative

$$s_2 - s_1 \geq 0 \tag{4.15}$$

In addition, the formation of a shock is by intersecting wave fronts. That means in the coordinate system that is moving with the shock wave, the upstream Mach number must be supersonic while the downstream Mach number must be subsonic in order to have a stable shock front

$$M_{1,n} \geq 1 \geq M_{2,n} \tag{4.16}$$

where additional subscript n indicates the normal component. In general, shocks are classified according to the sign of the pressure jump $p_2 - p_1$:

$$p_2 - p_1 > 0 \quad \text{compression shock} \tag{4.17}$$

$$p_2 - p_1 < 0 \quad \text{rarefaction or expansion shock} \tag{4.18}$$

In conventional gasdynamics, rarefaction shocks are not admissible due to the violation of the second thermodynamics law. Thompson[77] expanded the Rankine-Hugoniot equation

(4.13) using Taylor series and retained terms up to third order:

$$\Delta s = \frac{1}{12T_1}\left(\frac{\partial^2 v}{\partial p^2}\right)_s (\Delta p)^3 + O(\Delta p)^4 \tag{4.19}$$

Because the higher-order terms are omitted, this is only applicable to weak shocks. The first term in the above equation is related to Γ. It shows that with $\Gamma < 0$, the second law of thermodynamics can be satisfied with a decrease of pressure across the discontinuity surface, which is an expansion shock wave.

4.2 Expansion Shock

Table 4.1: Pre-shock states

States	$\frac{p}{p_c}$	$\frac{v}{v_c}$	Γ
A	2	3.5	$1 < \Gamma$
B	0.8	3	$0 < \Gamma < 1$
C	1	1.3	$\Gamma < 0$

In this section, a set of example cases for the polytropic van der Waals model of fluid PP10 is examined. Three different upstream states are considered as described in Table 4.1. The conventional gas dynamic analysis (case A) requires that Γ must be greater than 1, which represents most cases under regular working conditions. $\Gamma > 1$, the speed of sound increases with pressure increase and gas behavior is in good agreement with the classical theory. When Γ reaches 1, equation (1.2) shows that the speed of sound remains as a constant with pressure change because pressure is a linear function of density only. When Γ is smaller than 1 (case B), the speed of sound decreases with increasing pressure. Accompanying with the change of the speed of sound, the gas starts to show some unconventional behavior. If Γ goes further below 0 (case C), equation (1.1) shows that isentropes in this region have negative curvature and the gas dynamic behaviors are totally different or even opposite to classical theory.

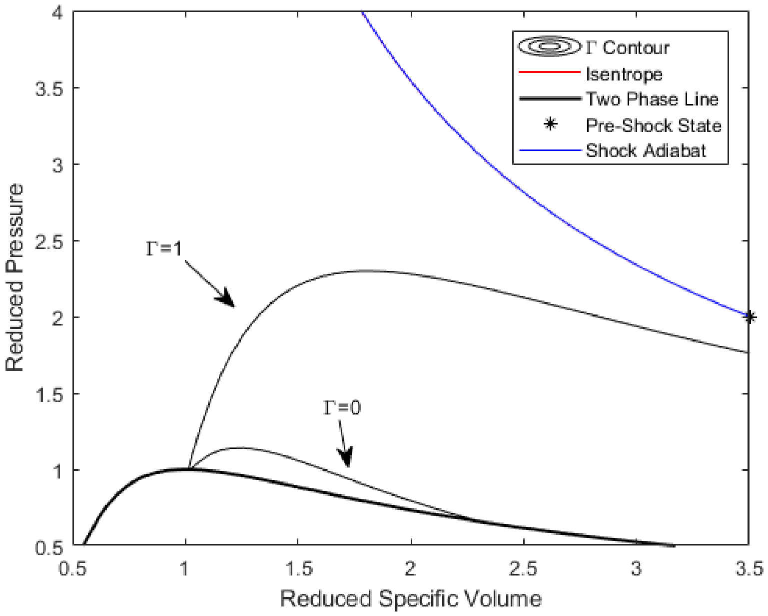

Figure 4.4: Shock adiabat on p-v plane with upstream state A

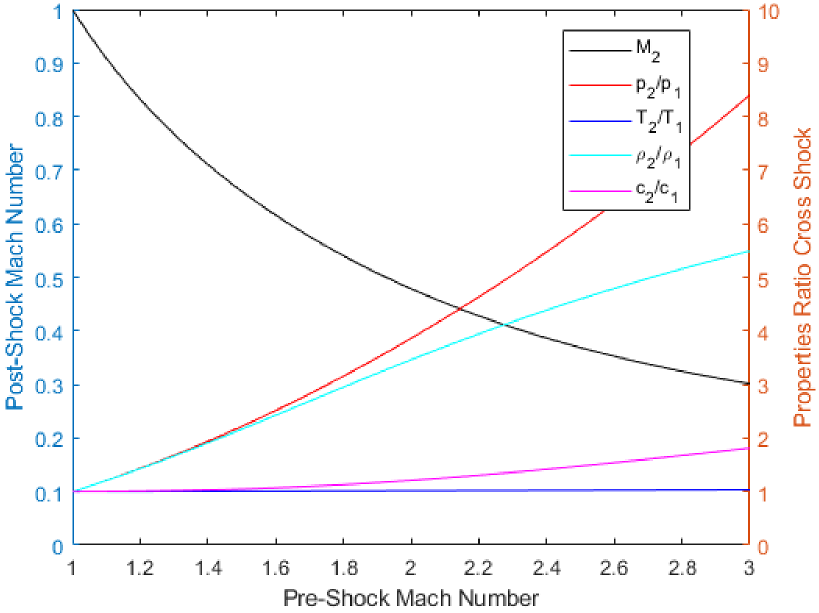

Figure 4.5: Variation of downstream Mach number M_2, density ratio$\frac{\rho_2}{\rho_1}$, static temperature ratio $\frac{T_2}{T_1}$, static pressure ratio $\frac{p_2}{p_1}$ and speed of sound ratio $\frac{c_2}{c_1}$ for upstream state A

Results of normal shocks originating from pre-shock state A, which is located in the region $\Gamma > 1$, are given in figure 4.5. The pre-shock state A is marked as a black star and the blue line is the shock adiabat in fig 4.4. The shock adiabat centered on state A is entirely located in the region $\Gamma > 1$ and the pressure increases with increasing pre-shock Mach number M_1 along the shock adiabat. Figure 4.5 shows the variation of the ratios ρ_2/ρ_1, p_2/p_1, T_2/T_1 and downstream Mach number M_2. As predicted by classical gasdynamics theory, pressure, density, speed of sound and density all increase across the shock wave. The monotonic decrease of post-shock Mach number M_2 is less with increasing pre-shock Mach number M_1 and moves towards a constant asymptote. The density ratio also tends to reach a maximum value as M_1 increases. The temperature increase is extremely small across the shock wave in the BZT fluid. The root cause of this phenomenon is the large isochoric heat capacity. It results in large internal energy so that the kinetic energy change across the shock thus becomes negligible compared to the internal energy. The shock adiabat and the isentrope are close to each other, indicating a small entropy change cross the shock wave. The same phenomenon is observed in both Case B and Case C. Moreover, unlike the ideal gas, where all properties across the shock wave can be expressed as a function of upstream Mach number M_1, the shock adiabat has strong dependence on the upstream thermodynamics conditions p_1 and T_1.

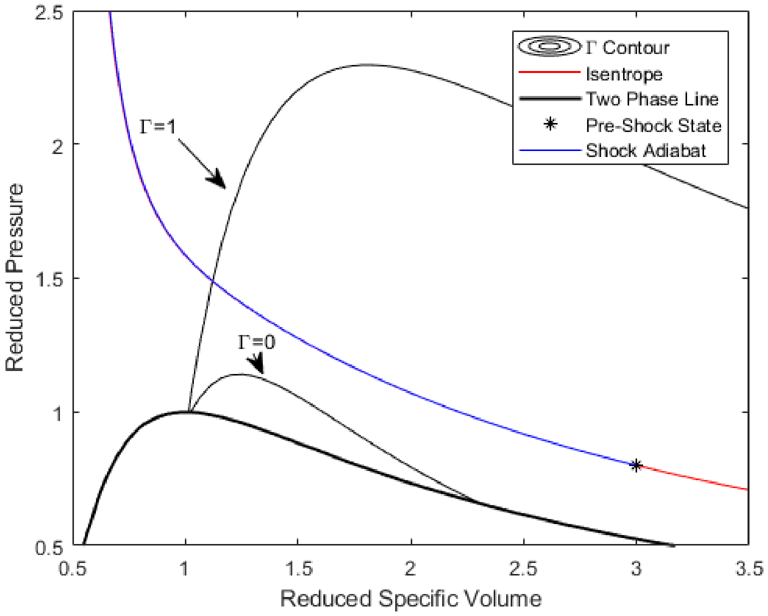

Figure 4.6: Shock adiabat on p-v plane with upstream state B

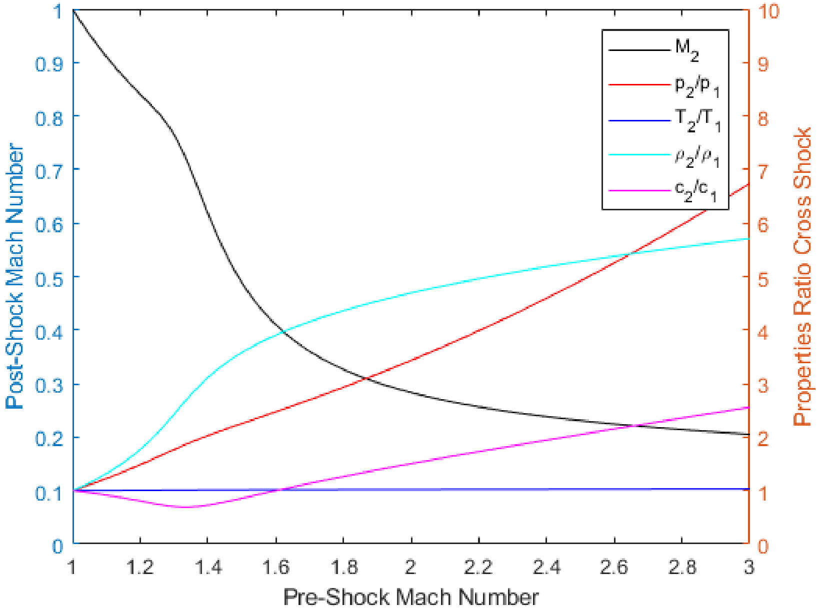

Figure 4.7: Variation of downstream Mach number M_2, density ratio$\frac{\rho_2}{\rho_1}$, static temperature ratio $\frac{T_2}{T_1}$, static pressure ratio $\frac{p_2}{p_1}$ and speed of sound ratio $\frac{c_2}{c_1}$ for upstream state B

Figure 4.6 shows the shock adiabat for Case B, where the pre-shock state is located in the region of $\Gamma < 1$. A wide portion of the shock adiabat lies inside the region $\Gamma < 1$. As the upstream Mach number M_1 increases further, the post-state falls into the region $\Gamma > 1$. In Figure 4.6, the isentrope is also plotted starting from the same upstream point. The shock adiabat and isentrope are very close to each other. This observation indicates the loss associated with the shock wave of a BZT fluid is negligible. It can be also reasonably explained by the high molecular complexity of the BZT fluid, high molecular degree of freedom and internal energy. The energy transferred from dynamic energy to internal energy is relatively small compared to the internal energy of the fluid, causing a very small temperature rise cross the shock wave. Thus, the entropy generation is very small. M_2 still decreases monotonically with the increase of M_1. But the ratio of speed of sound $\frac{c_2}{c_1}$ no longer monotonically increase with M_1 increase. For the part of shock adiabat located inside the region $0 < \Gamma < 1$, speed of sound decreases as pre-shock Mach number M_1 increases.

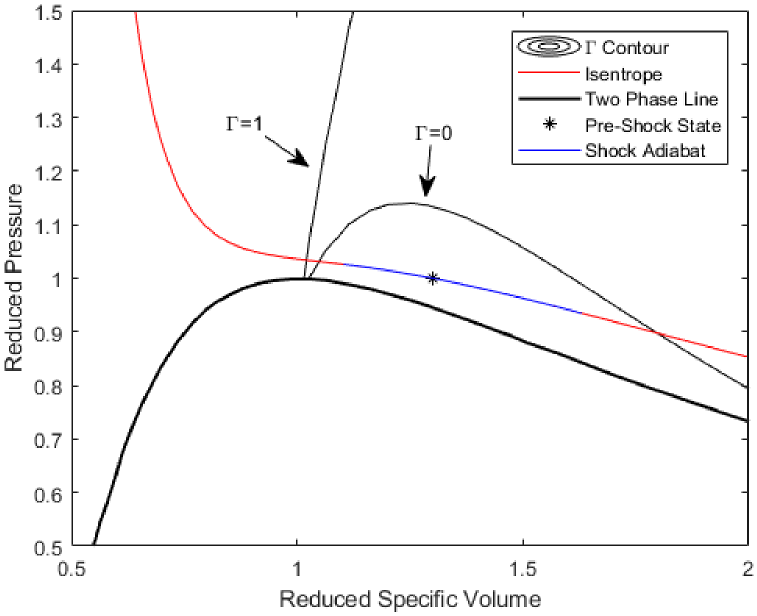

Figure 4.8: Shock adiabat on p-v plane with upstream state C

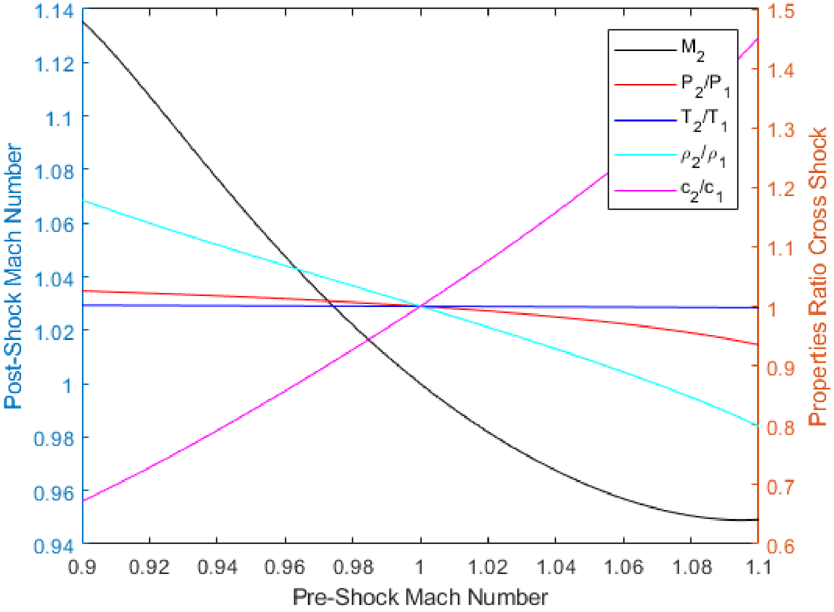

Figure 4.9: Variation of downstream Mach number M_2, density ratio$\frac{\rho_2}{\rho_1}$, static temperature ratio $\frac{T_2}{T_1}$, static pressure ratio $\frac{p_2}{p_1}$ and speed of sound ratio $\frac{c_2}{c_1}$ for upstream state C

In the last example case, where the upstream state C with $\Gamma < 0$ is considered. Figure 4.8 shows the shock adiabat where upstream Mach number M_1 ranges from 0.9 to 1.1. Both compression and expansion fraction of the shock adiabat are entirely located inside the non-classical region. The entropy change in figure 4.10 indicates that only the expansion shock adiabat branch is physically admissible in this region because of the second law of thermodynamics. The entropy results agrees with the prediction by Beth [25] and Thompson [20]. Post shock Mach number M_2 still monotonically decrease with M_1 increase and tends to reach an asymptote as M_1 is sufficiently large. Density and pressure dropped across the shock; thus, flow is accelerated. But due to the stronger inverse dependence of sound speed and pressure upon isentropic expansion, flow is changing from supersonic speed into subsonic speed across the shock, which satisfies the wave speed ordering relation $M_1 > 1 > M_2$.

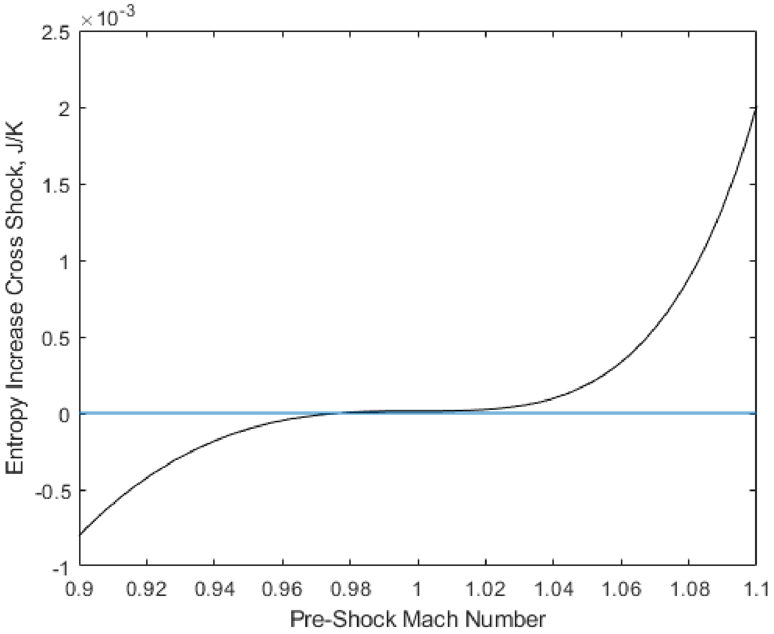

Figure 4.10: Entropy change across shock wave for upstream state C

4.3 Compression Fan

In conventional gas dynamics, the sudden withdrawal of the piston will generate an expansion wave travelling toward the opposite direction. Thus, fluid density, temperature and pressure drop through an isentropic process.

The characteristic method shows that[78]:

$$u + \int \frac{c}{\rho} d\rho = \text{constant along} : \frac{dx}{dt} = u + c; \tag{4.20}$$

$$u - \int \frac{c}{\rho} d\rho = \text{constant along} : \frac{dx}{dt} = u - c; \tag{4.21}$$

Equations (4.20) and (4.21) are called the Riemann invariants. Locally, within the wave, the disturbance travels at the sound speed. The temperature and density vary through the wave thus the wave local speeds are different. The front of the fan, or the first wave, has the greatest propagation speed. On the opposite edge, the tail of the expansion fan, has the least propagation speed. In the non-classical region where $\Gamma < 0$, compressible fan is physically possible due to the non-monotonic dependence of sound speed on pressure. If a piston is pushed into the fluid on the left end of the tube, the fluid is accelerated and the pressure increases. The sound speed will decrease as the pressure increases towards the piston so that the local wave speed $u + c$ could possibly be higher at the wave front that makes a compressible fan admissible.

We consider the unsteady flow in a one-dimensional tube as a piston at the left end pushes into the initially uniform still gas in the tube. Equations (4.20) and (4.21) are integrated numerically to search for possible compression fan solutions. For a normal gas, this would produce a compression shock for any finite speed of the piston, but for a gas with $\Gamma < 0$, we show that it produces a compression fan.

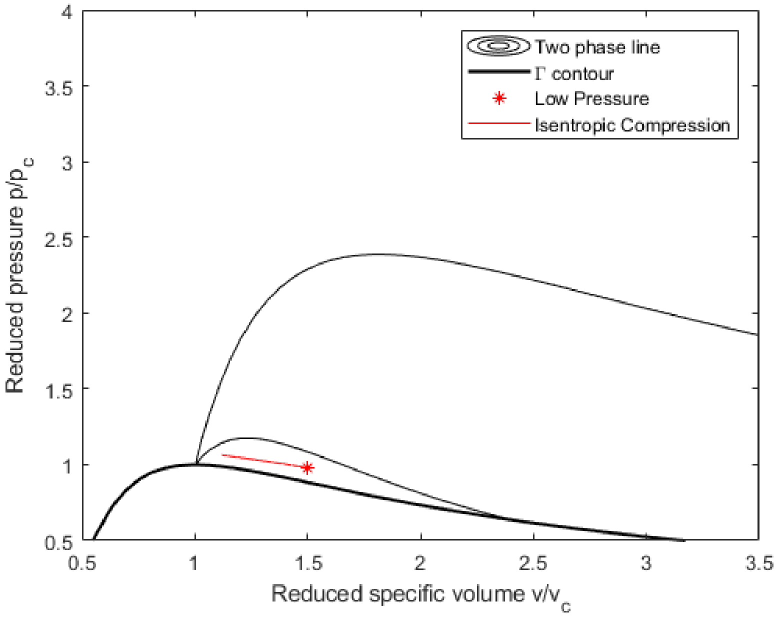

Figure 4.11: Initial state and the isentropic process for compression fan on p-v diagram

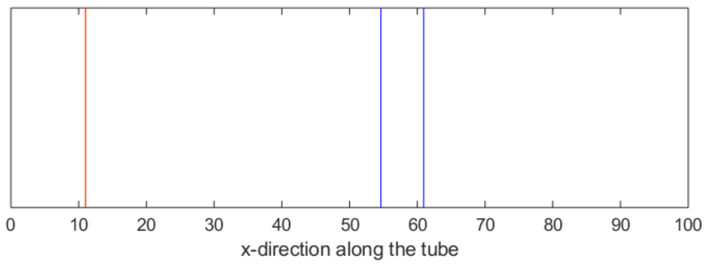

Figure 4.12: Wave location at $t = 1s$ (red line represents piston location, thin blue line is tail wave, bold blue line is front wave)

The initial state in the tube for a compression fan case is shown as the red star in fig 4.11, the red line represents the states within the fan. Fig 4.12 shows the position of the piston, wave front and wave tail. A piston (red solid line) is pushing the fluid towards the right (positive x-direction) and a set of compression wave (fan) is travelling towards the right. The front of the fan (first wave) is travelling faster than the tail of the fan (fig 4.13, which means it satisfies the wave speed relation). Fig 4.14 shows that entropy is constant for this case, where the oscillation is caused by numerical calculation and is relatively small (less than 10^{-12}).

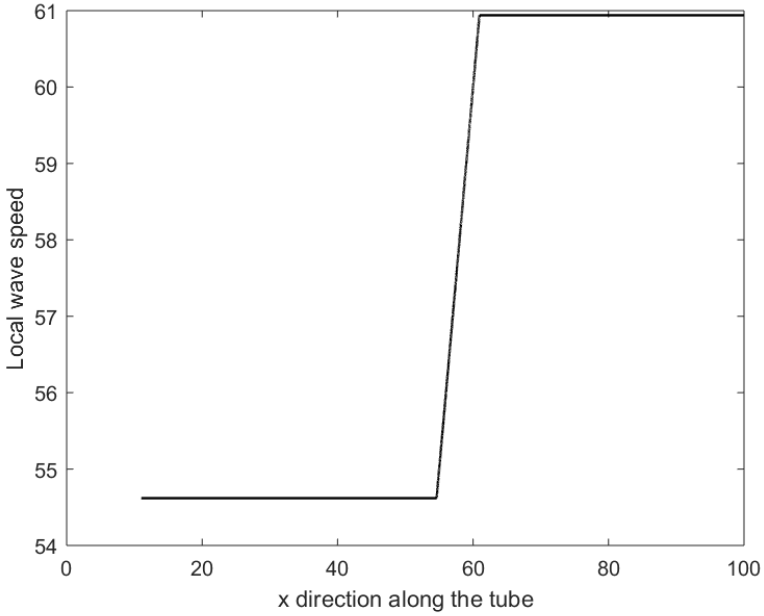

Figure 4.13: Local wave speed at $t = 1s$

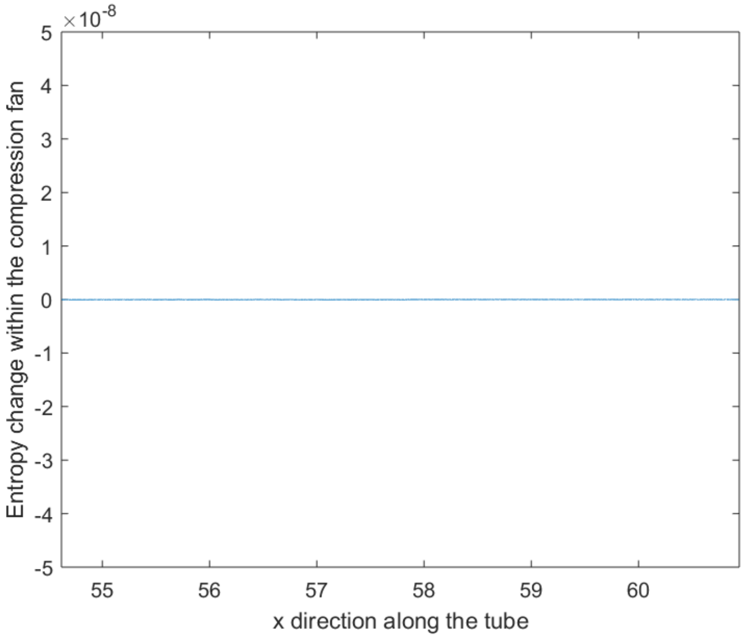

Figure 4.14: Entropy distribution

4.4 Double Sonic Shock

It is shown in Figure 2.6 that Γ can change sign when the flow cross the boundary of non-classical and classical region. Therefore, the curvature of a shock adiabat may change as well. Unlike in the region when Γ does not change sign, where only compression shock or expansion shock can be observed, both expansion shock and compression shock may be observed. Both expansion and compression wave may occur within the same pulse [79]. This could lead to the formation of a sonic shock where upstream, or downstream or both have a Mach number of unity. Figure 4.17 shows the shock adiabat of a non-classical gas. The two points connected by the black line represents upstream and downstream of a double sonic shock. Cramer [80] presented exact solutions for double sonic shock in Van der Waals gases.

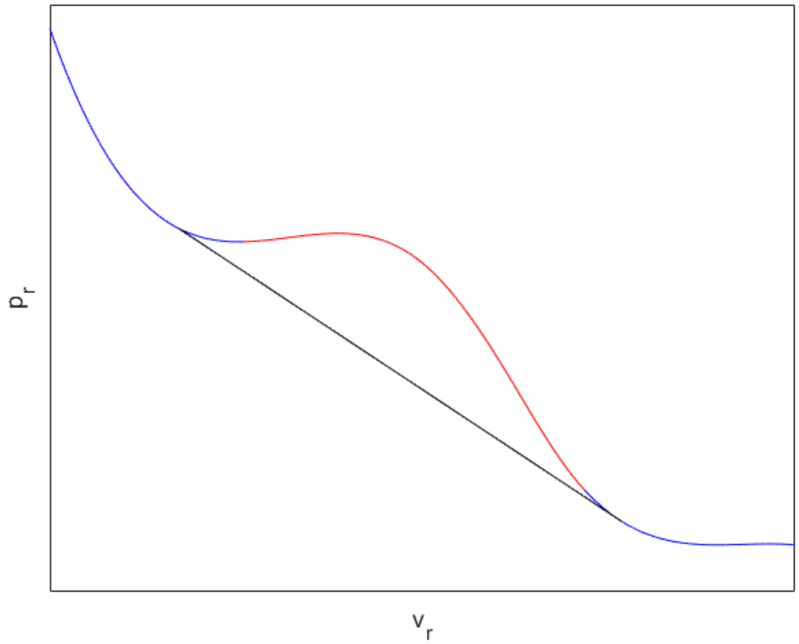

Figure 4.15: p-v diagram for double sonic shock wave, blue line is shock adiabat in $\Gamma > 0$ region and red line is shock adiabat in $\Gamma < 0$ region, black line connects upstream and downstream of the shock

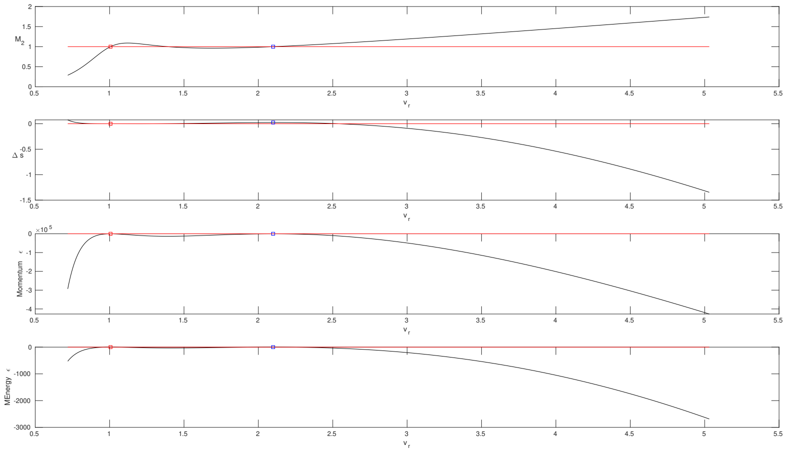

Figure 4.16: Solution along the shock adiabat with upstream $p_r = 1.0685$, $v_r = 1.006166$ and $M_1 = 1$

The initial condition for the double sonic shock wave is shown in Figure 4.17. Solutions are plotted along the shock adiabat in Figure 4.16. It can be confirmed here only one downstream state is admissible when upstream Mach number is unity. The results agrees with Cramer's result. The upstream and downstream of the double sonic shock is shown in Table 4.2.

Table 4.2: Upstream and downstream conditions for a double sonic shock

	p_r	v_r	Γ	$c(m/s)$
Upstream	1.06845	1.006166	1.7849	27.7212
Downstream	0.8259	2.1	0.3257	57.8584

This upstream and downstream conditions are used for an unsteady simulation. The left side of the tube is initially at the upstream condition and the right side of the tube is initially at the downstream condition. The discontinuity is presented at the center of the tube. Results are shown in Figure 4.18 for $t = 0.1s$. In this case, the initial Mach number on both sides are 1 and the discontinuity is maintained at the center of the tube. The flow is sonic and maintains sonic after it is expanded through the discontinuity. The flow is accelerated from 55 m/s to 84 m/s.

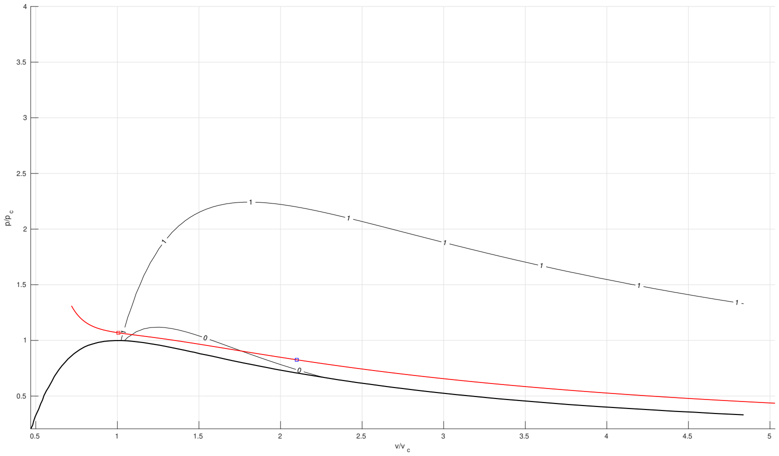

Figure 4.17: p-v diagram for double sonic shock wave

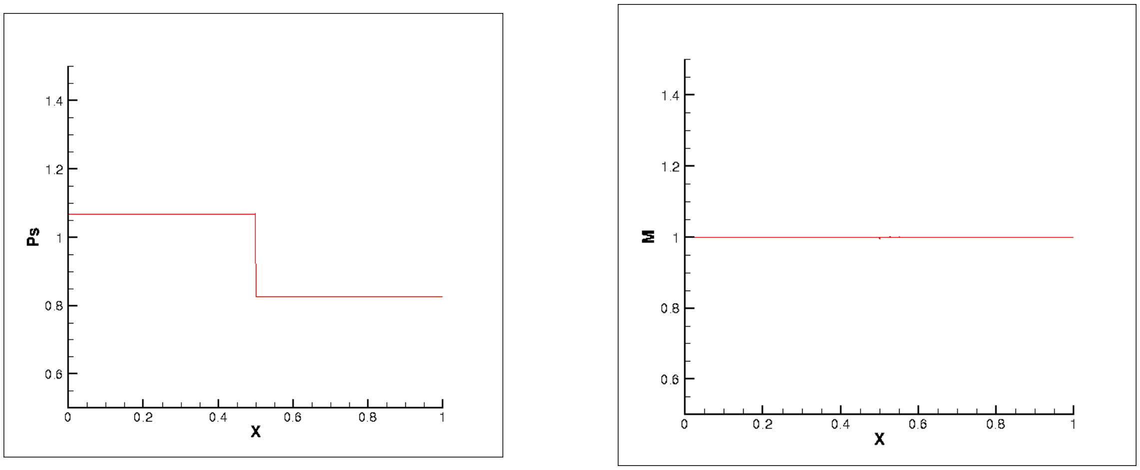

(a)

(b)

Figure 4.18: Result for double sonic shock at $t = 0.1s$ (a) Mach number (b) Pressure

4.5 Prandtl Meyer Relation and Compression Fan

The Prandtl-Meyer function plays an important role in the analysis of many steady isentropic flows. With a perfect gas, the Prandtl-Meyer function permits a simple and explicit formula. However, many applications require the consideration of real gas effects. In Organic Rankine Cycles, the fluid is operated in a region where expansion shock and compression fan may exist.

For any fluid, the differential form of the Prandtl-Meyer function is

$$d\theta = \sqrt{M^2 - 1}\frac{dV}{V} \tag{4.22}$$

where M is Mach number and V is the fluid velocity. For an ideal gas, it can be directly integrated into

$$\theta_2 - \theta_1 = \nu(M_1) - \nu_(M_2) \tag{4.23}$$

where ν is the Prandtl-Meyere function

$$\nu(M) = \sqrt{\frac{\gamma+1}{\gamma-1}}tan^{-1}\sqrt{\frac{\gamma-1}{\gamma+1}(M^2-1)} - tan^{-1}\sqrt{M^2-1} \tag{4.24}$$

For the Van der Waals equation of state, we have

$$\begin{aligned}
p_2 &= \frac{RT_2}{v_2-b} - \frac{a}{v_2^2} \\
s_2 - s_1 &= c_v ln\left(\frac{T_2}{T_1}\right) + Rln\left(\frac{v_2-b}{v_1-b}\right) \\
H_2 &= c_vT_2 - \frac{a}{v_2} + p_2v_2 = H_0 - \frac{1}{2}V_2^2
\end{aligned} \tag{4.25}$$

Differentiate equation 4.25 to get (derivation can be found in appendix)

$$ds = \frac{c_v}{T}dT + \frac{R}{v-b}dv \tag{4.26}$$

$$dH_0 = \left(c_v + \frac{Rv}{v-b}\right)dT + \left[\frac{2a}{v^2} - \frac{RTb}{(v-b)^2}\right]dv + VdV \tag{4.27}$$

For an isentropic process, entropy and total enthalpy change are 0. The change in temperature and specific volume can be evaluated by equation (4.26) and (4.27) with given change in velocity. Thus, the Prandtl-Meyer relation can be obtained by numerically integrating equation (4.26) and (4.27).

Free stream conditions are given in Table 4.3. The pressure p and specific volume v are normalized by the critical point values. Three cases are considered

Table 4.3: Dense gas cases for Prandtl Meyer relation

	P_∞	v_∞	Γ_∞	M_∞
PMC1	1.25	0.75	1.6	1.01
PMC2	1.25	0.75	1.6	1.01
PMC3	0.8	1.3	-0.04	1.01

In Case 1, the expansion process is shown in the p-v diagram (see Figure 4.19). The incoming fluid is supersonic and in the region of $\Gamma > 0$ and the entire expansion process is outside of the region where $\Gamma < 0$. In this region, the fluid is expected to behave like an ideal gas and classical gas dynamics phenomenon should be observed. Variation of Mach number with respect to the flow turning angle is plotted in Figure 4.20a. It can be seen that Mach number monotonically increases with the flow turning angle. Sound speed monotonically decreases as flow expands.

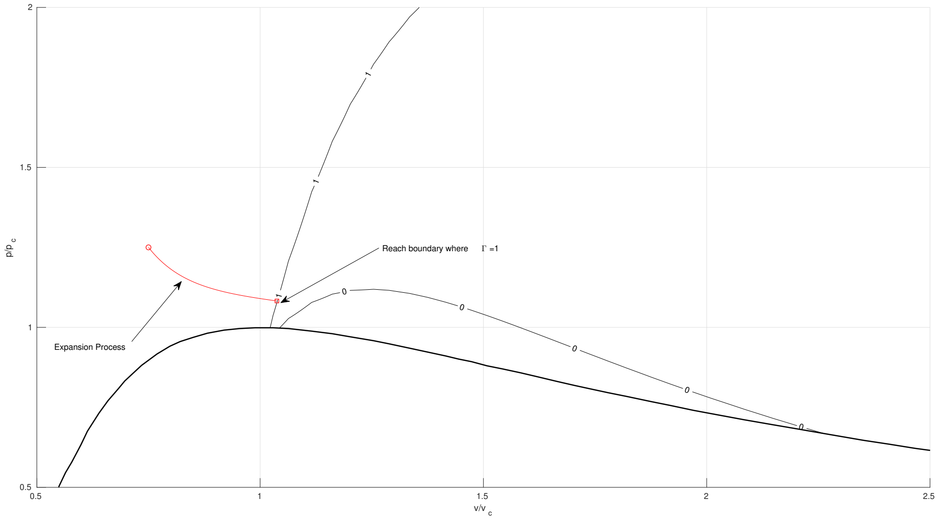

Figure 4.19: p-v diagram for case 1

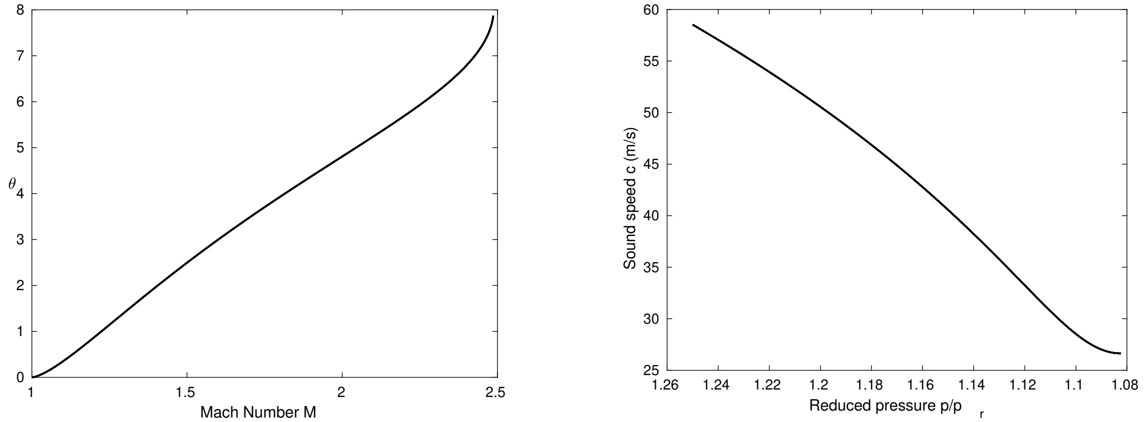

(a) (b)

Figure 4.20: (a) Case 1 Mach number vs turning angle (b) Case 1 Pressure vs sound speed

In Case 2, the upstream flow condition is the same as in Case 1 but the flow is further expanded. In the expansion process shown in Figure 4.23, the flow crosses the boundary $\Gamma = 1$ once and the boundary $\Gamma = 0$ twice. The sound speed starts to increase when pressure decreases as the flow expands into the region of $\Gamma < 1$. This may cause a decrease in Mach number if the sound speed decreases faster than the increasing rate of flow velocity, which is observed in Figure 4.22a. The Mach number reaches a maximum value of 2.47 at $\theta = 7.9^o$. Between $\theta = 7.9^0$ and $\theta = 30^o$, Mach number decreases as flow turns or expands.

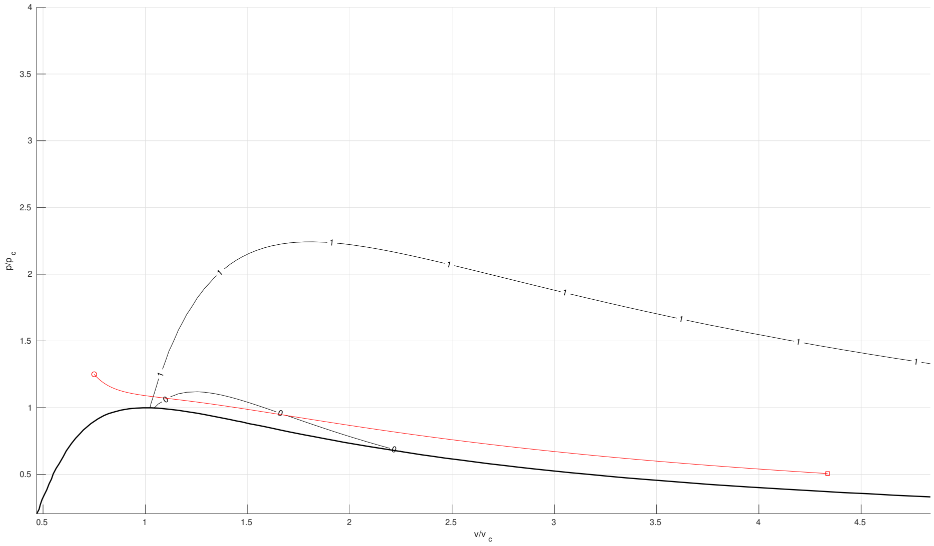

Figure 4.21: p-v diagram for case 2

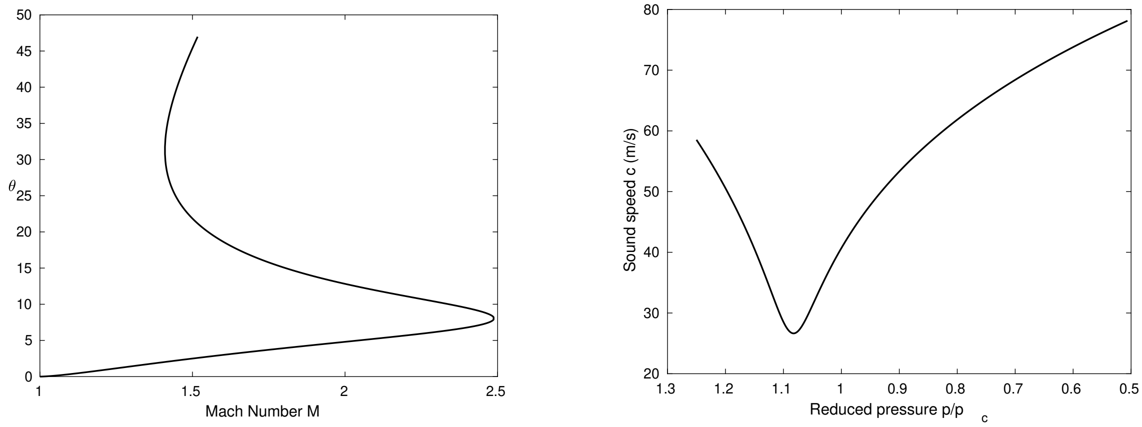

(a)

(b)

Figure 4.22: (a) Case 2 Mach number vs turning angle (b) Case 2 pressure vs sound speed

In Case 3, the wedge is compressive with $\theta = 10.7^o$. the upstream flow has Mach number $M_\infty = 1.01$ and is located in the region of < 0 with pressure $p_\infty = 0.8$ and specific volume $v = 1.3$. As the incoming flow is in the non-classical region where compression fan is admissible. A Prandtl-Meyer compression fan is centered at the corner. The compression process is isentropic.

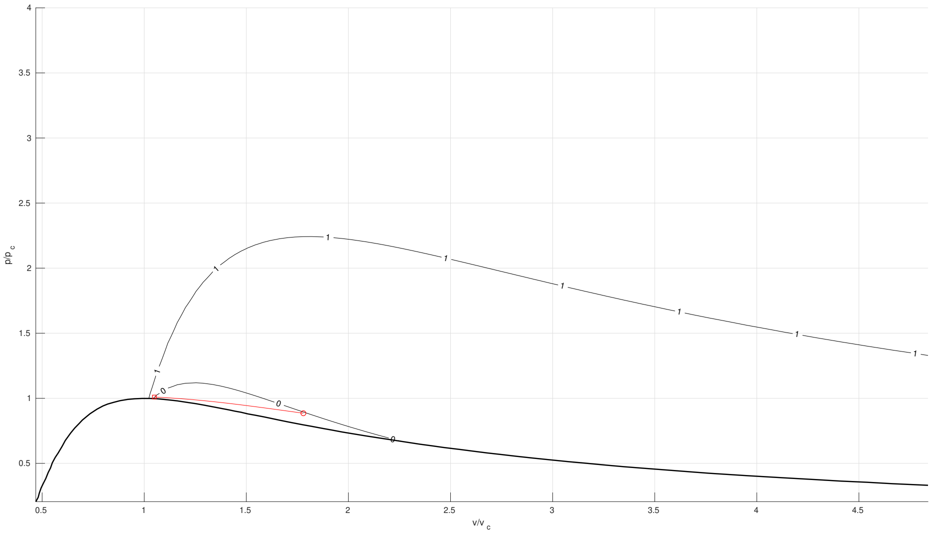

Figure 4.23: p-v diagram for case 3

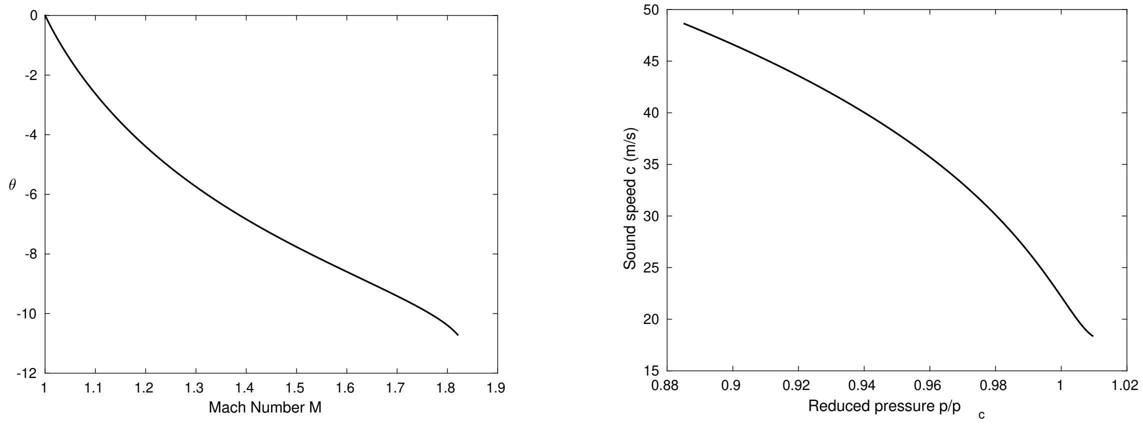

(a)

(b)

Figure 4.24: (a) Case 3 Mach number vs turning angle (b) Case 3 pressure vs sound speed

Chapter 5

Numerical Simulation

5.1 Numerical Solver

In this chapter, basic numerical methods used in this dissertation are presented [81]. All solvers employed in this dissertation use a cell-centered finite volume method. Central differencing is used to calculate numerical fluxes. The JST scheme [3] is adopted to add second-order and fourth-order artificial dissipation for stability consideration. To reach a steady-state solution, explicit multi-stage Runge-Kutta scheme is applied as pseudo-time stepping method.

5.1.1 Governing Equation

The Navier-Stokes equations which govern the dynamics of fluid flow are derived from conservation laws of mass, momentum, energy. In general, the Navier-Stokes equations with perfect gas equation of state (EOS), Fourier law of heat conduction for heat transfer and the compatibility condition for the viscous stresses are as given below.

$$\frac{\partial}{\partial t}\int_{\Omega}\rho d\Omega+\oint_{\partial\Omega}\rho\left(\vec{v}\cdot\vec{n}\right)dS=0 \tag{5.1}$$

$$\frac{\partial}{\partial t}\int_{\Omega}\rho\vec{v}d\Omega+\oint_{\partial\Omega}\rho\vec{v}\left(\vec{v}\cdot\vec{n}\right)dS=\int_{\Omega}\rho\vec{f}_e d\Omega-\oint_{\partial\Omega}p\vec{n}dS+\oint_{\partial\Omega}\left(\bar{\bar{\tau}}\cdot\vec{n}\right)dS \tag{5.2}$$

$$\frac{\partial}{\partial t}\int_{\Omega}\rho E d\Omega+\oint_{\partial\Omega}\rho H\left(\vec{v}\cdot\vec{n}\right)dS=\oint_{\partial\Omega}k\left(\nabla T\cdot\vec{n}\right)dS+\int_{\Omega}\left(\rho\vec{f}_e\cdot\vec{v}+\dot{q}_h\right)d\Omega+\oint_{\partial\Omega}\left(\bar{\bar{\tau}}\cdot\vec{n}\right)\cdot\vec{n}dS \tag{5.3}$$

where ρ is the density of the fluid, $\vec{v}$ is velocity vector, p is the thermodynamic pressure, and E refers to the total energy per unit mass. For, ideal gas, the total energy per unit mass is defined as $E=c_vT+\frac{1}{2}v^2$. If viscosity and thermal conductivity are neglected, we obtain the Euler equations for inviscid compressible flows,

$$\frac{\partial}{\partial t}\int_{\Omega}\rho d\Omega+\oint_{\partial\Omega}\rho\left(\vec{v}\cdot\vec{n}\right)dS=0 \tag{5.4}$$

$$\frac{\partial}{\partial t}\int_{\Omega}\rho\vec{v}d\Omega+\oint_{\partial\Omega}\rho\vec{v}\left(\vec{v}\cdot\vec{n}\right)dS+\oint_{\partial\Omega}p\vec{n}dS=\int_{\Omega}\rho\vec{f}_e d\Omega \tag{5.5}$$

$$\frac{\partial}{\partial t}\int_{\Omega}\rho E d\Omega+\oint_{\partial\Omega}\rho H\left(\vec{v}\cdot\vec{n}\right)dS=\int_{\Omega}\left(\rho\vec{f}_e\cdot\vec{v}\right)d\Omega \tag{5.6}$$

5.1.2 Cell-centered Finite Volume Method on Structured Grids

In the present work, structured grids and cell-centered finite volume method are used in all solvers. The flow domain is decomposed into small cells. For structured grids and cell-centered scheme, these cells can be easily ordered using indices i,j,k of cell centers. For the sake of simplicity, the finite-volume method is presented on two-dimensional Euler equations. In conservative differential form, the Euler equations can be written as

$$\frac{\partial w}{\partial t} + \frac{\partial f}{\partial x} + \frac{\partial g}{\partial y} = 0 \tag{5.7}$$

where

$$w = \begin{pmatrix} \rho \\ \rho u \\ \rho v \\ \rho E \end{pmatrix}, \quad f = \begin{pmatrix} \rho u \\ \rho u^2 + p \\ \rho uv \\ \rho E u + pu \end{pmatrix}, \quad g = \begin{pmatrix} \rho v \\ \rho uv \\ \rho v^2 + p \\ \rho E v + pv \end{pmatrix} \tag{5.8}$$

where t is time, density, p pressure. x and y stand for coordinates in two-dimensional space; u and v, are the flow velocity components in the x and y directions; Total energy and total enthalpy are $E = e + (u^2 + v^2)/2$ and $H = h + (u^2 + v^2)/2$, respectively, with $h = e + p$ and $e = \frac{p}{(\gamma-1)\rho}$. γ is the ratio of specific heats.

Integrating equation 5.7 over a grid cell, the equation becomes

$$\frac{\partial}{\partial t}\int_{\Omega} \boldsymbol{W} d\Omega + \int_{S} \boldsymbol{F} \cdot \vec{n} dS = 0 \tag{5.9}$$

where $\boldsymbol{F} = f\vec{i} + g\vec{j}$ and $\vec{n} = n_x\vec{i} + n_y\vec{j}$ is the outward unit normal vector on cell surfaces. is volume of the grid cell. For grid cell (i, j), following the method of lines and only discretize in space, the semi-discrete form of equation (5.9) can be written as

$$\frac{d}{dt}\left(\boldsymbol{W}_{i,j}\Omega_{i,j}\right) + \boldsymbol{C_{i,j}} = 0 \tag{5.10}$$

where $\Omega_{i,j}$ is the volume of grid cell (i, j), $\boldsymbol{W}_{i,j}$ is the volume-averaged solution of vector of state variables over the cell; and $\boldsymbol{C_{i,j}}$ is the finite volume approximation of the net convective fluxes flowing out of the cell that can be formulated for cell-centered scheme as

$$\boldsymbol{C}_{i,j} = \boldsymbol{F}_{i-\frac{1}{2},j} \cdot \vec{S}_{i-\frac{1}{2},j} + \boldsymbol{F}_{i+\frac{1}{2},j} \cdot \vec{S}_{i+\frac{1}{2},j} + \boldsymbol{F}_{i,j+\frac{1}{2}} \cdot \vec{S}_{i,j+\frac{1}{2}} + \boldsymbol{F}_{i,j-\frac{1}{2}} \cdot \vec{S}_{i,j-\frac{1}{2}} \tag{5.11}$$

where $\vec{S}$ is the outward normal surface vector on cell faces. It is expressed as $\vec{S}_{i+\frac{1}{2}} = \vec{n}_{i+\frac{1}{2}}\Delta S_{i+\frac{1}{2}}$ on cell face $(i + \frac{1}{2})$ for example. Hence, $\Delta S_{i+\frac{1}{2}}$ is the cell face area (length in two dimension) on cell face $(i + \frac{1}{2}, j)$. In this dissertation, the convective flux vectors at all four cell surfaces are evaluated as the average of those on the two adjacent cells as:

$$\boldsymbol{F}_{i-\frac{1}{2},j} = \frac{1}{2}\left(\boldsymbol{F}_{i-1,j} + \boldsymbol{F}_{i,j}\right) \tag{5.12}$$

$$\boldsymbol{F}_{i+\frac{1}{2},j} = \frac{1}{2}\left(\boldsymbol{F}_{i,j} + \boldsymbol{F}_{i+1,j}\right) \tag{5.13}$$

$$\boldsymbol{F}_{i,j-\frac{1}{2}} = \frac{1}{2}\left(\boldsymbol{F}_{i,j-1} + \boldsymbol{F}_{i,j}\right) \tag{5.14}$$

$$\boldsymbol{F}_{i,j+\frac{1}{2}} = \frac{1}{2}\left(\boldsymbol{F}_{i,j} + \boldsymbol{F}_{i,j+1}\right) \tag{5.15}$$

The above treatment of convective flux on cell faces is equivalent to second-order central differencing on a Cartesian grid. It is well known that a central differencing scheme alone suffers from odd-even decoupled spurious solutions as well as undesired oscillations in the neighbourhood of shock waves for transonic flows. To solve these problems, artificial dissipation is required and equation (5.10) can be revised as

$$\frac{d}{dt}\left(\boldsymbol{W}_{i,j}\Omega_{i,j}\right)+\boldsymbol{C}_{\boldsymbol{i},\boldsymbol{j}}-\boldsymbol{D}_{i,j}=0 \tag{5.16}$$

where $D_{i,j}$ is the artificial dissipation flux added to grid cell (i,j). To remove oscillations near shock waves, MacCormack et al.[82] introduced a second-order dissipation term. Then Beam et al.[83] added a fourth-order dissipation term to provide background damping for stability and convergence needs. In the JST scheme proposed by Jameson, Schmidt and Turkel [81], these two necessary components are combined together. A switching function is also introduced to activate the second-order dissipation near shock wave while turning off the fourth-order dissipation and switch off the second-order term in smooth region while allowing for the operating of the fourth-order term. In this dissertation, the JST scheme is adopted and the artificial dissipation is given as

$$\boldsymbol{D}_{i,j}=\boldsymbol{D}^{(2)}_{i,j}-\boldsymbol{D}^{(4)}_{i,j} \tag{5.17}$$

where $D^{(2)}_{i,j}$ and $D^{(4)}_{i,j}$ are second-order and fourth-order artificial dissipation fluxes, respectively. Each of them is a summation of the corresponding artificial dissipation vectors calculated on all cell faces:

$$\boldsymbol{D}^{(2)}_{i,j}=\boldsymbol{d}^{(2)}_{i+\frac{1}{2},j}-\boldsymbol{d}^{(2)}_{i-\frac{1}{2},j}+\boldsymbol{d}^{(2)}_{i,j+\frac{1}{2}}-\boldsymbol{d}^{(2)}_{i,j-\frac{1}{2}} \tag{5.18}$$

$$\boldsymbol{D}^{(4)}_{i,j}=\boldsymbol{d}^{(4)}_{i+\frac{1}{2},j}-\boldsymbol{d}^{(4)}_{i-\frac{1}{2},j}+\boldsymbol{d}^{(4)}_{i,j+\frac{1}{2}}-\boldsymbol{d}^{(4)}_{i,j-\frac{1}{2}} \tag{5.19}$$

where $\boldsymbol{d}^{(2)}$ and $\boldsymbol{d}^{(4)}$ are the second-order and fourth-order artificial dissipation vectors evaluated on cell faces and can be defined as

$$\boldsymbol{d}^{(2)} = \boldsymbol{\Lambda}_{i+\frac{1}{2},j}\epsilon^{(2)}_{i+\frac{1}{2},j}(\boldsymbol{W}_{i+1,j} - \boldsymbol{W}_{i,j}) \tag{5.20}$$

$$\boldsymbol{d}^{(4)} = \boldsymbol{\Lambda}_{i+\frac{1}{2},j}\epsilon^{(4)}_{i+\frac{1}{2},j}(\boldsymbol{W}_{i+2,j} - 3\boldsymbol{W}_{i+1,j} + 3\boldsymbol{W}_{i,j} - \boldsymbol{W}_{i-1,j}) \tag{5.21}$$

on cell face $(i + \frac{1}{2}, j)$ for example. The Λ in equation (2.11) is a variable scaling factor and is set to be:

$$\Lambda_{i+\frac{1}{2},j} = 2min(\lambda^I_{i+1,j}, \lambda^I_{i,j}) \tag{5.22}$$

where Λ^I is the spectral radius of the convective flux Jacobian in the i direction, defined as

$$\Lambda^I_{i,j} = \left|\vec{V}_{i,j} \cdot \frac{\Delta\vec{S}_{i+\frac{1}{2},j} + \Delta\vec{S}_{i-\frac{1}{2},j}}{2}\right| + c_{i,j}\frac{\Delta S_{i+\frac{1}{2},j} + \Delta S_{i-\frac{1}{2},j}}{2} \tag{5.23}$$

where $c_{i,j}$ is the local speed of sound of the cell (i, j). Spectral radius in the J direction is given similarly. $\epsilon^{(2)}$ and $\epsilon^{(4)}$ are the coefficients for the second-order and fourth-order artificial dissipation terms, respectively. They have the function of switching on or off the two dissipation terms and are defined as

$$\epsilon^{(2)}_{i+\frac{1}{2},j} = \kappa^{(2)}\min[\frac{1}{4}, \max(\nu_{i+1,1}, \nu_{i,j})] \tag{5.24}$$

$$\epsilon^{(4)}_{i+\frac{1}{2},j} = \max[0, (\kappa^{(4)} - \epsilon^{(2)}_{i+\frac{1}{2},j})] \tag{5.25}$$

where $\kappa^{(2)}$ and $\kappa^{(4)}$ are two constants in the order of 1 and ν is the JST switch function [81] using the pressure as a sensor:

$$\nu_{i,j} = \left|\frac{p_{i-1,j} - 2p_{i,j} + p_{i+1,j}}{p_{i-1,j} + 2p_{i,j} + p_{i+1,j}}\right| \tag{5.26}$$

with the above switch function, the second-order and fourth-order dissipation can work properly in different regions of a flow field. In the region close to shock waves, the pressure has a sudden jump hence ν and $\epsilon^{(2)}$ are all in the order of 1. Therefore, the second-order dissipation is enabled while the fourth-order dissipation is disabled. On the other hand, in the smooth region, ν is negligible. Then the second-order dissipation is switched off and the fourth-order dissipation is functioning to provide background damping needed by central differencing scheme.

5.1.3 Runge-Kutta Time Stepping Scheme

To obtain steady-state solutions, the residuals must be driven toward zero. A common convergence-acceleration-technique is done by using the so-called pseudo-time-forcing method. Equation (5.16) is written as

$$\frac{d}{dt}\left(\boldsymbol{W}_{i,j}\Omega_{i,j}\right) + R_{i,j}(\boldsymbol{W}_{i,j}) = 0 \tag{5.27}$$

An explicit-time-marching method may then be used to solve the above equations. Because only the steady-state result is of interest in this case, the pseudo-time stepping does not have to be time-accurate in nature and must only remain stable. At the end of pseudo-time marching, the residual $R_{i,j}(\boldsymbol{W}_{i,j})$ achieves zero and the desired solution is reached.

In this dissertation, a four-stage Runge-Kutta scheme is employed as the explicit pseudo-time marching method, which is given as

$$\begin{aligned}
W^{(0)} &= W^n \\
W^{(1)} &= W^{(0)} - \frac{\Delta t}{2\Omega} R(W^{(0)}) \\
W^{(2)} &= W^{(0)} - \frac{\Delta t}{2\Omega} R(W^{(1)}) \\
W^{(3)} &= W^{(0)} - \frac{\Delta t}{\Omega} R(W^{(2)}) \\
W^{(4)} &= W^{(0)} - \frac{\Delta t}{6\Omega} (R(W^{(0)}) + 2R(W^{(1)}) + 2R(W^{(2)}) + R(W^{(3)})) \\
W^{n+1} &= W^{(4)}
\end{aligned} \tag{5.28}$$

where superscript $n+1$ and n refer to two successive pseudo-time steps. Besides, techniques such as local time stepping, residual smoothing and multigrid method can be applied to accelerate convergence to the steady-state solution.

5.1.4 Extension to Arbitrary Thermodynamic Models

For ideal gas, internal energy e, pressure p and density ρ can be related by the simple relation

$$e = \frac{1}{\gamma - 1} \frac{p}{\rho} \tag{5.29}$$

the pressure p can be updated directly from the conservative variables. Additionally, the partial derivatives of primary thermodynamic variables can be calculated directly from ideal gas model, thus making it very simple to implement Roe type scheme. However, the numerical schemes for real-fluid flows require the calculation of partial and secondary derivatives of primary thermodynamic variables as a function of density ρ and internal energy e. They can be calculated from the conservative variables as follows

$$\rho = W_1 \tag{5.30}$$

$$e = \frac{W4}{W1} - \frac{W_2^2 + W_3^2}{2W_1^2} \tag{5.31}$$

Any other thermodynamic property ϕ can be calculated through an arbitrary thermodynamic model

$$\phi = \phi(\rho, e), \tag{5.32}$$

Equation (5.32) could be explicit for some equations of state such as van der Waals EOS and Peng Robinson EOS. Numerical iteration scheme may be required if explicit form can not be determined. For more accurate computation, the external thermodynamic libarary REFPROP from NIST could be implemented easily for this central solver.

5.2 Shock Tube

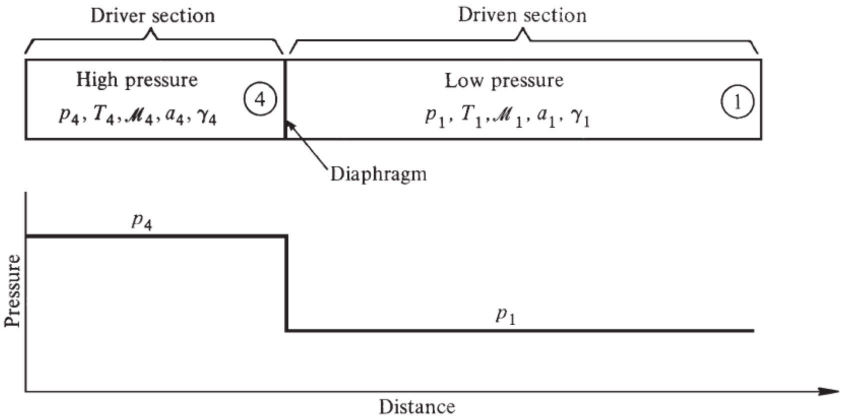

Figure 5.1: Initial conditions in a pressure-driven shock tube [84]

The shock tube problem, sometimes known as the Riemann problem, is a classic fluid dynamics and computational fluid dynamics problem. Experimental fluid dynamicists have used the shocktube to study shock and expansion waves, as well as their interactions, for decades. Shock tubes have also been used to supply supersonic and hypersonic wind tunnels with high-pressure and high-temperature gas. The shock tube is a common one-dimensional test problem for numerical algorithms in CFD. The Shock tube structure is sketched in Figure 5.1. This is a tube closed at both ends, with a diaphragm separating a region of high-pressure gas on the left from a region of low-pressure gas on the right. The initial pressure distribution is also shown in Figure 5.1.

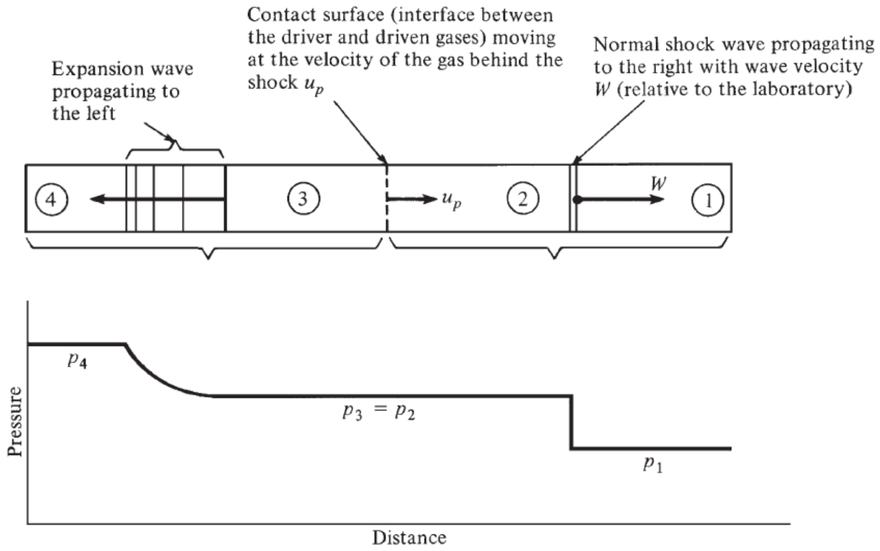

Figure 5.2: Flow in a shock tube after the diaphragm is broken [84]

For an ideal gas, the shock tube problem has been well studied both numerically and experimentally. As shown in Figure 5.2, when the diaphragm is broken, a shock wave propagates into the low-pressure end (section 1) and an expansion wave propagates into high-pressure end (section 4). As discussed in previous chapters, BZT gases exhibit non-classical phenomena including mixed wave, which depends on the value of Γ. Therefore, the flow in the non-classical shock tube could develop into multiple wave structures after the diaphragm breaks and it is determined by the initial condition of the shock tube.

5.2.1 Results

For this non-classical shock tube simulation, the shock tube is initially at rest with a diaphragm in the middle to separate the high-pressure fluid and low-pressure fluid. The high-pressure fluid is located at the left side of the shock tube and the low-pressure fluid is located at the right side of the shock tube . Three cases are discussed to illustrate the non-classical wave phenomenon in a shock tube. The initial conditions can be found in table 5.1. In each case, flow evolution is plotted in p-v diagram and x-t diagram. Solution for p, T, ρ at a given time t is plotted.

Table 5.1: Dense gas cases

	ρ_L	P_L	Γ_L	Wave Type	ρ_R	P_R	Γ_R	Wave Type
Case1	0.879	1.09	-0.0031	ES	0.562	0.885	-4.016	CF
Case2	0.909	1	-1.41	ES	0.4	0.75	0.48	CS
Case3	0.879	1.09	-0.0031	ES+EF	0.275	0.575	0.703	CS

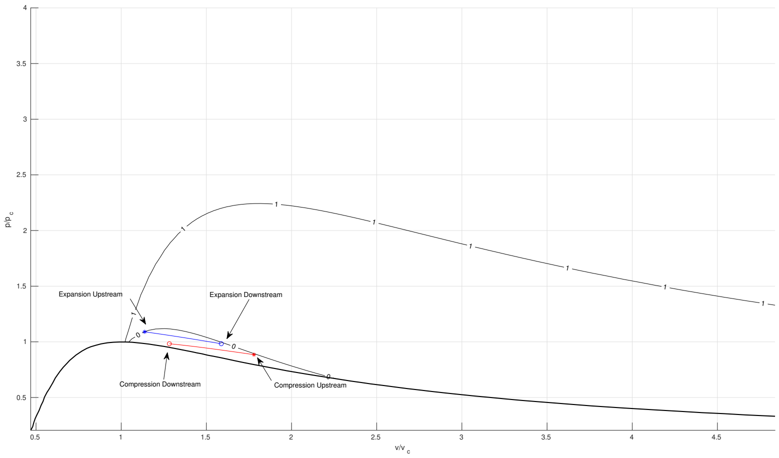

Figure 5.3: Case 1 p-v diagram

Case 1 is a typical non-classical behavior, since the initial states belong entirely to the regions with $\Gamma < 0$ and it remains in this region in the whole flow field without crossing the boundary of $\Gamma = 0$. Figure 5.3 shows that both state 1 and state 4 are located inside the region of $\Gamma < 0$. Figure 5.4 show that an expansion shock propagates into the high-pressure fluid with shock speed $u_s = 32\ m/s$. The compression fan is propagating to the right with leading edge and trailing edge located at $x = 0.9\ m$ and $x = 0.81\ m$ respectively as shown in the Figure 5.11. The contact surface is located between the expansion shock and compression fan at $x = 0.6\ m$ and is propagating to the right. The contact surface in Figure 5.4 is not very sharp because of the artificial dissipation of the central scheme.

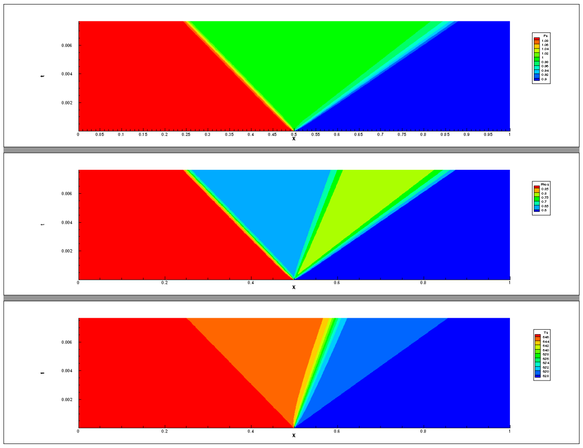

Figure 5.4: Case 1 x-t diagram (P, ρ, T)

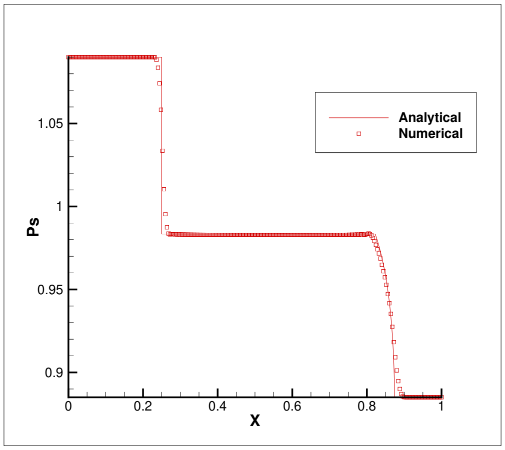

Figure 5.5: Case 1 pressure distribution

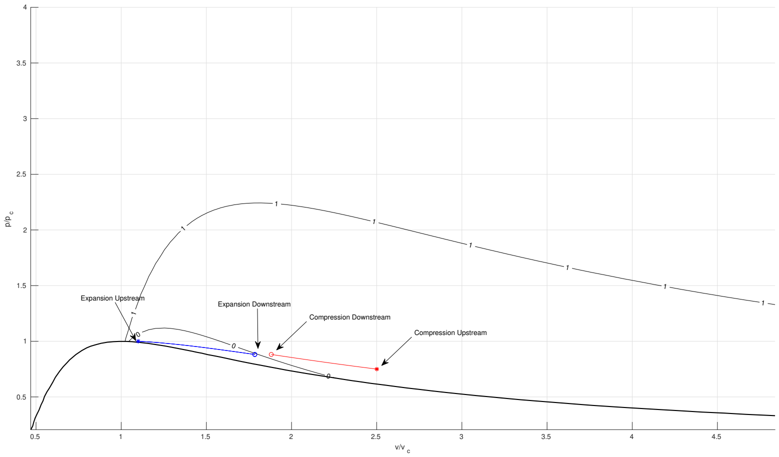

Figure 5.6: Case 2 p-v diagram

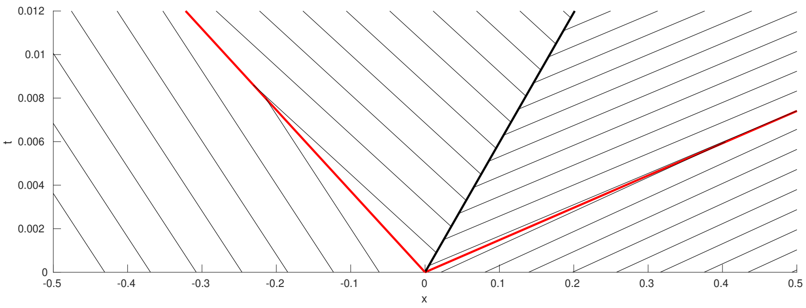

Figure 5.7: Case 2 wave field (red line on the left is expansion shock, red line on the right is compression wave, black bold line is contact surface)

For Case 2, the initial condition for high-pressure fluid is located in the region of $\Gamma < 0$ but the low-pressure fluid is located in the region of $\Gamma > 0$ as shown in Figure 5.6. The pressure distribution at $t = 0.5s$ is shown in Figure 5.9. An expansion shock located at $x = 0.35m$ is propagating to the high-pressure fluid and a compression shock located at $x = 0.95m$ is propagating to the low-pressure fluid at a higher speed, The contact surface is located between expansion shock and compression shock and is propagating towards the low-pressure fluid. In the x-t diagram, both types of shock are distinguishable as they remain compact during the propagation. The entropy distribution is shown in Figure 5.10, note that there is a positive entropy jump across both expansion shock and compression shock but they are relatively small compared to the entropy difference across the contact surface. The shock wave for dense gas generally has a smaller entropy jump compared to the shock wave in dilute gas because of the large internal energy.

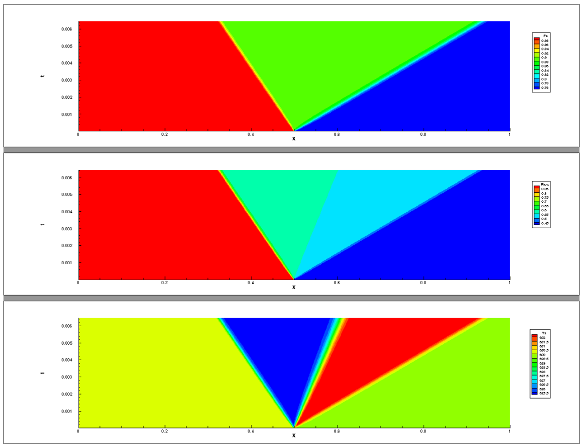

Figure 5.8: Case 2 x-t diagram (P, ρ, T)

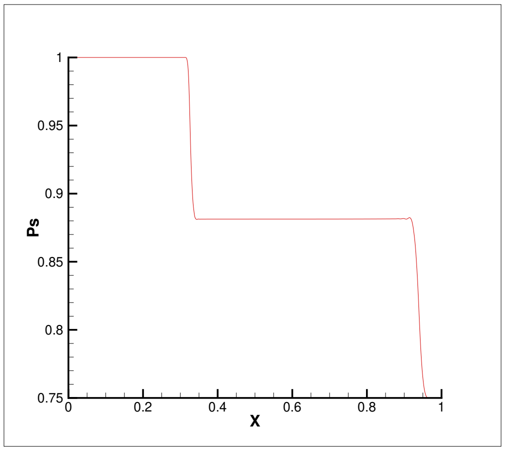

Figure 5.9: Case 2 pressure distribution

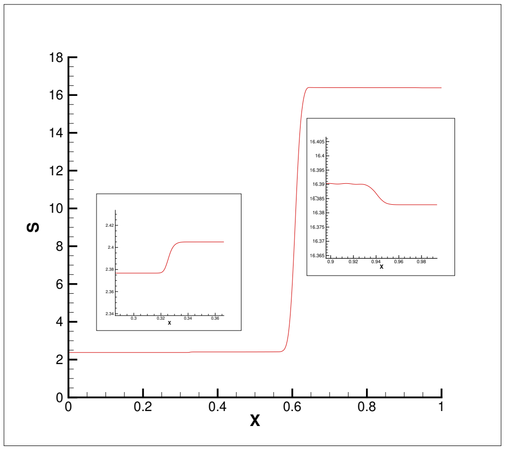

Figure 5.10: Case 2 Entropy distribution

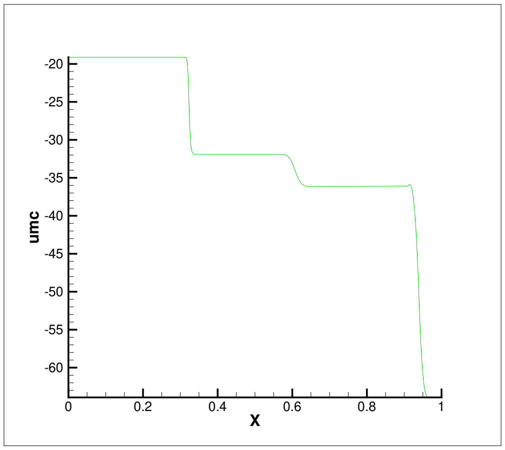

Figure 5.11: Case 2 wave speed

The initial condition for Case 3 is shown in Figure 5.12. The initial condition for case 3 is very similar to the initial condition of Case 2 where the high-pressure fluid is in the region of $\Gamma < 0$ and the low-pressure fluid is in the region of $\Gamma > 0$. But the low-pressure fluid has a much lower pressure in this case. Mixed wave phenomenon is observed in Case 3. The boundary of $\Gamma = 0$ is crossed during the flow evolution. At $x = 0.81m$, a compression shock is propagating into the low-pressure fluid. The expansion shock is propagating to the left followed by a set of expansion fans with the leading edge at $x = 0.41m$. In computational results, it is very hard to capture the exact location where the shock is split into a set of fans because the shock wave is also represented by a set of discrete point rather than a very sharp discontinuity. In Figure 5.15, it can be seen that more grid points appear after $x = 0.41$; this is also observed in the density distribution in Figure 5.16. It indicates the location where expansion shock collides with the leading edge of the expansion fan. This is later confirmed by the analytical results. Note that, at this point, the fluid is already in the region of $\Gamma > 0$; this indicate the transition from expansion shock to expansion fan does not occur at the boundary $\Gamma = 0$. The high-pressure fluid in the non-classical region is first expanded by an expansion shock into the region of $\Gamma > 0$; then, it is further expanded by a continuous expansion fan. The left-running wave speed is shown in Figure 5.17, the expansion shock speed is propagating to the left at speed of $29.2 m/s$ and the wave in front of the shock wave is propagating at a lower speed. After the expansion shock, the wave speed decreases.

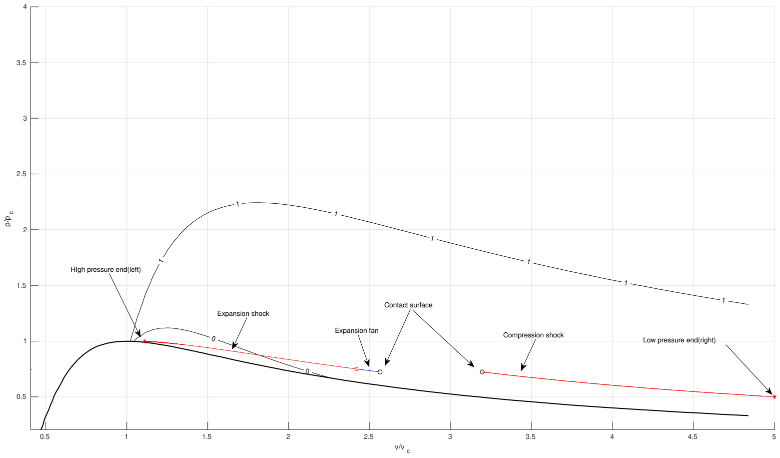

Figure 5.12: Case 3 p-v diagram

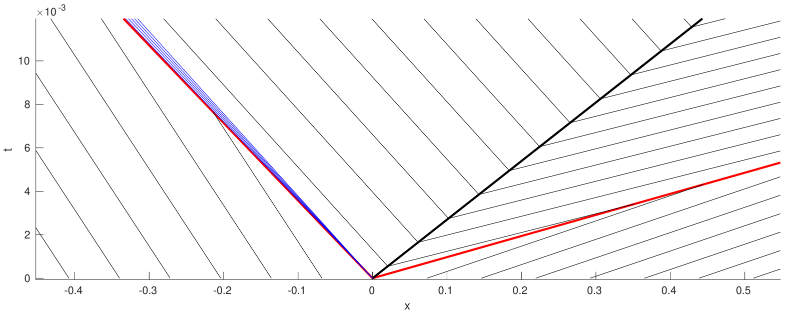

Figure 5.13: Case 3 wave field (red line on the left is expansion shock, blue lines are expansion fan, red line on the right is compression wave, black bold line is contact surface)

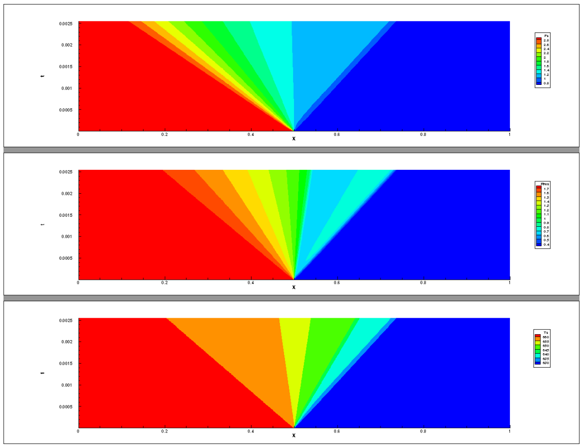

Figure 5.14: Case 3 x-t diagram (P, ρ, T)

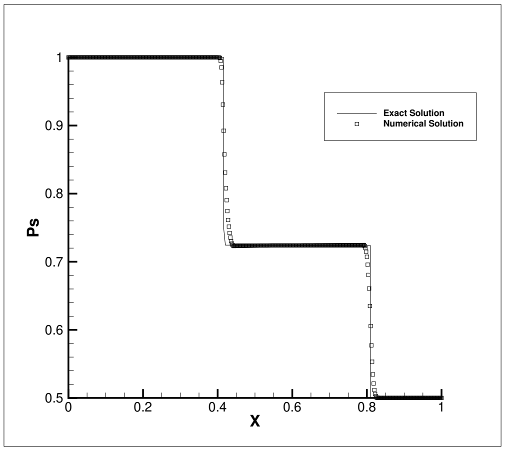

Figure 5.15: Case 3 pressure distribution

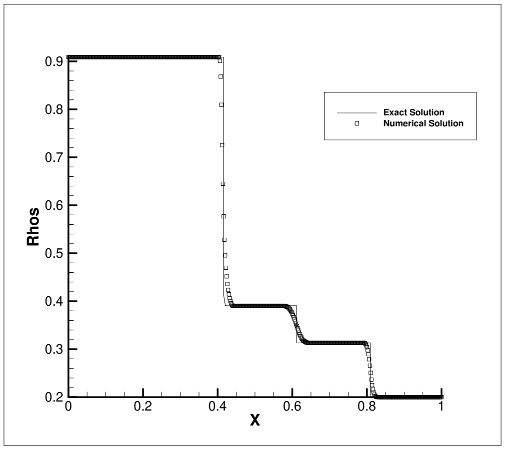

Figure 5.16: Case 3 density distribution

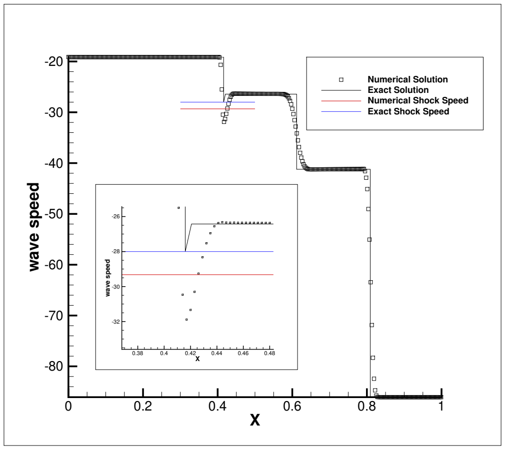

Figure 5.17: Case 3 left-running wave speed

5.3 Flow Over Corner

Supersonic flows over corner geometries provide important predictions of realistic flow phenomena in aerodynamics. For gas in classical region, an oblique shock occurs when a supersonic flow is turned in by a compression corner as shown in Figure 5.18(a). In contrast, an expansion wave is formed when a supersonic flow is turned away by an expansion corner as shown in Figure 5.18(b), flow properties change smoothly through the expansion fan and entropy remains constant.

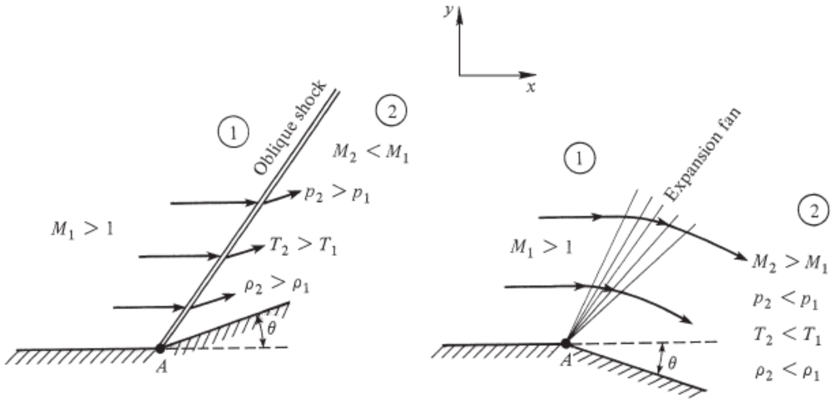

(*a*) Concave corner
(*b*) Convex corner

Figure 5.18: Supersonic flow over corner for classical gas[84]

For a given incoming flow Mach number, the deflection angle and oblique shock angle of the flow over a compression corner can be determined by the The $\theta - \beta - M$ relation [84]

$$\tan\theta = 2\cot\beta \left[\frac{M_1^2 \sin^2\beta - 1}{M_1^2(\gamma + \cos 2\beta) + 2} \right] \tag{5.33}$$

where M_1 is the Mach number of the incoming flow, β is the oblique shock angle and θ is the deflection angle. The relation is plotted in figure 5.19. As shown in the figure, there is a maximum deflection angle θ_{max} for a given Mach number M_1. θ_{max} decreases as M_1 decreases. For a deflection angle $\theta < \theta_{max}$, there are two values of the oblique shock angle β as shown in figure 5.20. One corresponds to a weak shock and the other corresponds to a strong shock. For the weak oblique shock in the classical gas region, flow may be either supersonic or subsonic after the shock. For the strong oblique shock, the flow is subsonic after the shock. For any deflection angle $\theta > \theta_{max}$, the shock will be curved and detached as shown in Figure 5.21.

In contrast to classical gas, the wave fields are much more complex as discussed in chapter 3. The gas behavior over compression and expansion corners can no longer be predicted by classical gas theory. To understand non-classical supersonic flows behavior over corner geometries, numerical simulation are performed using supersonic MDM flow for both classical and non-classical.

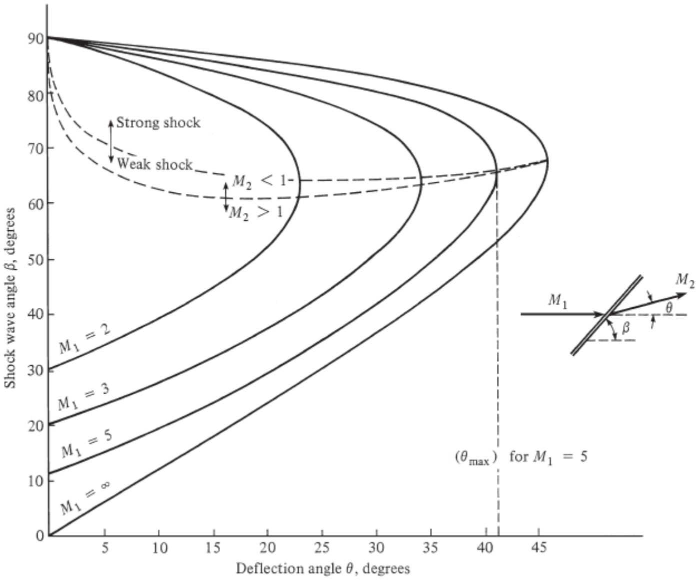

Figure 5.19: $\theta - \beta - M$ relation (θ: oblique shock angle; δ: deflection angle; M: Mach number) [84]

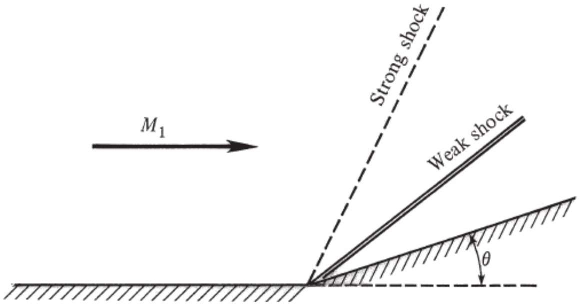

Figure 5.20: Weak and Strong shock[84]

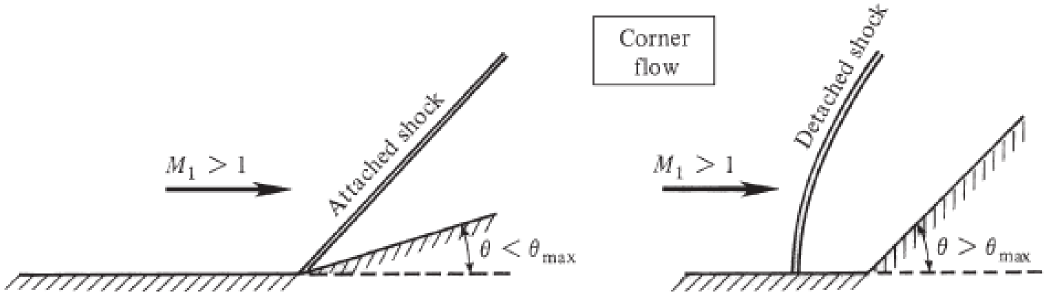

Figure 5.21: Attached and detached shock[84]

5.3.1 Expansion Corner

Table 5.2: Initial conditions for the flow over an expansion corner

Case	$\frac{p}{p_c}$	$\frac{v}{v_c}$	Γ	M	Deflection δ
NC1	1	1.3	-0.915	3.21618484	-7^o
NC2	1	1.3	-0.915	3.21618484	-20^o
C1	1.2	1.7	0.558	3.21618484	-7^o
C2	1.2	1.7	0.558	3.21618484	-20^o

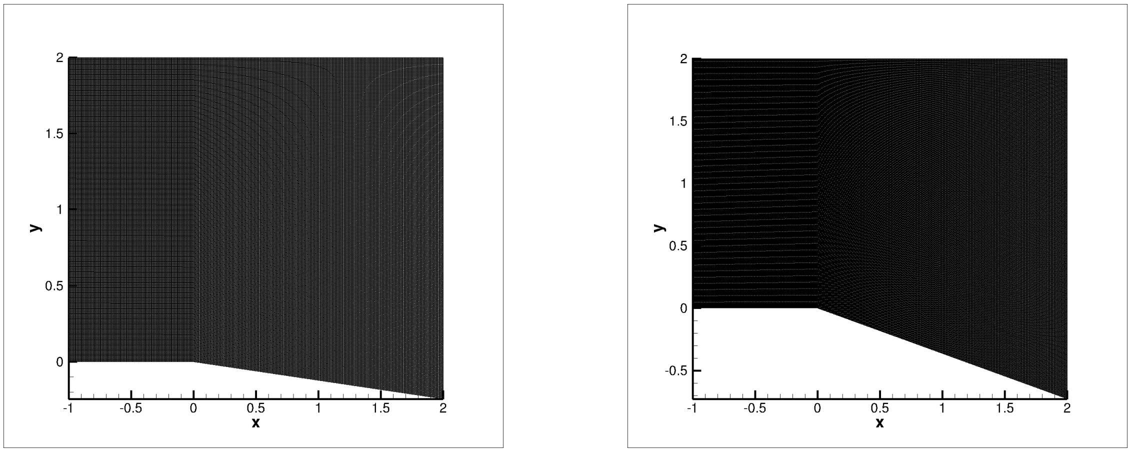

(a) (b)

Figure 5.22: Computational domain for expansion ramp (a) 600×600 grid with $\theta = -7^o$ (b) 600×600 grid with $\theta = -20^o$

The initial conditions for the expansion corner cases are in Table 5.2. Pressure p and specific volume v are normalized by the critical point values. Two 600×600 meshes are used as shown in figure 5.22. The first one has deflection angle of -7^o and the second one has deflection angle of -20^o. C represents classical gas case with initial condition of the flow in the region $\Gamma > 0$ and NC represents non-classical gas case with initial condition of the flow in the region $\Gamma < 0$.

Figure 5.23 -5.24 show the solutions for case C1 and NC1. In NC1, the upstream state was properly selected to generate a non-classical expansion shock wave. The geometry consists of a simple domain containing a corner with slope $\theta = -7^o$. Figure 5.23 reports the fundamental derivative field for both C1 and NC1. In C1, the flow recovers classical gas behavior and a expansion fan develops over the corner. The flow expands smoothly across the expansion fan and the fluid stays in the classical region both before and after the expansion fan. In contrast, An expansion shock can be observed in figure 5.23b - 5.24b for NC1. This strong discontinuity separates the domain into two uniform regions. Mach number decreases across the shock. The fundamental derivative increases from negative to positive across the shock, which indicates that flow can jump from the non-classical region to the classical region through an expansion shock. At the same time, a pressure drop and an entropy increase are observed across the discontinuity as revealed in figure 5.26, which further confirmed this is a non-classical expansion shock.

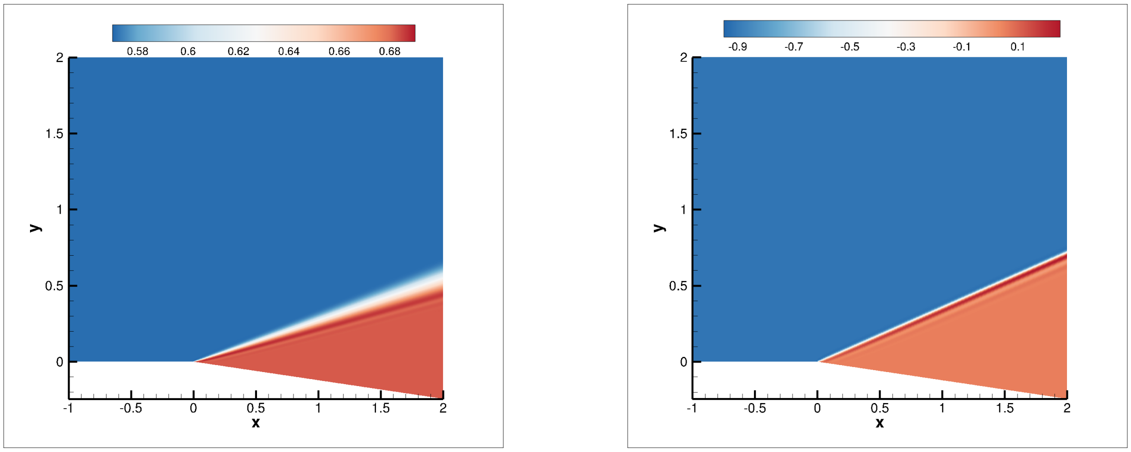

(a) (b)

Figure 5.23: Fundamental derivative Γ contour (a) C1 (b) NC1

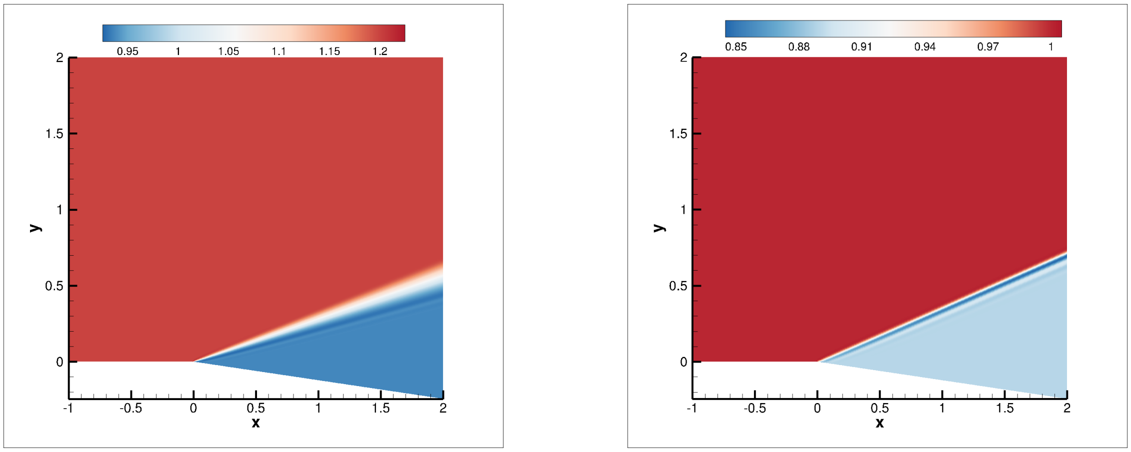

(a) (b)

Figure 5.24: Pressure contour (a) C1 (b) NC1

In figure 5.26, numerical results are compared to analytical results where the solid black line represents analytical solution and the red squares represent numerical solution. Overall, the numerical solution agrees with the analytical solution except for some entropy oscillation after the expansion shock. However, the error between the numerical solution and analytical solution is still within 0.1%.

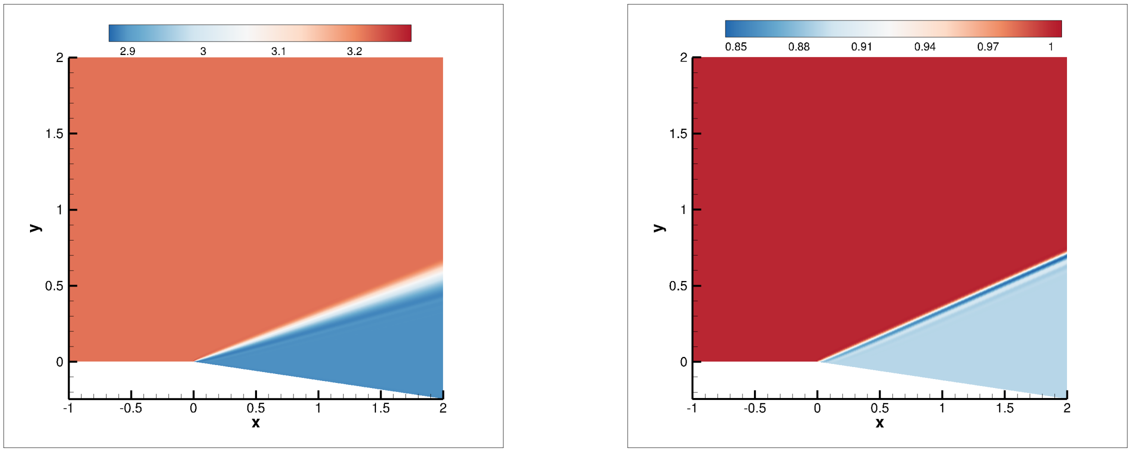

(a) (b)

Figure 5.25: Mach number contour (a) C1 (b) NC1

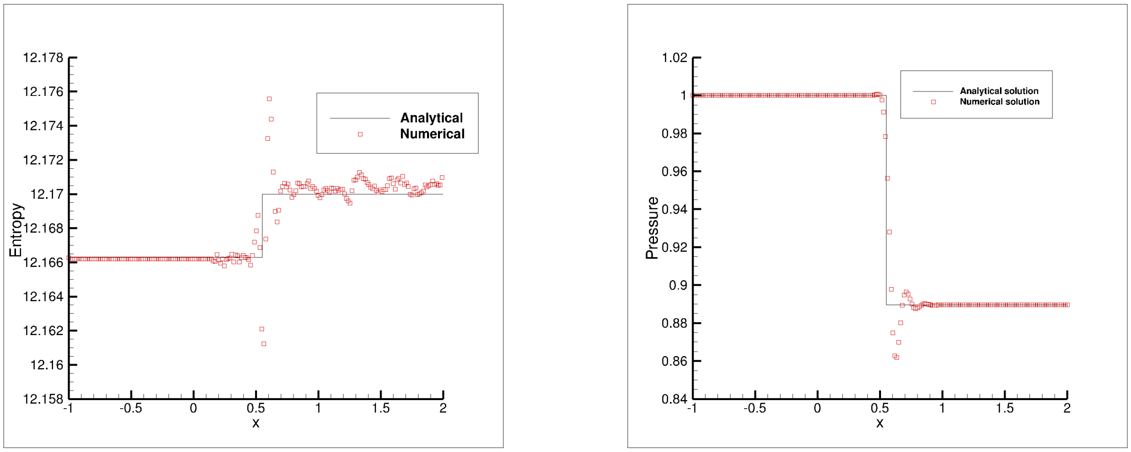

(a) (b)

Figure 5.26: Case NC1 (a) Entropy distribution at $y = 0.2$ (b) Pressure distribution at $y = 0.2$

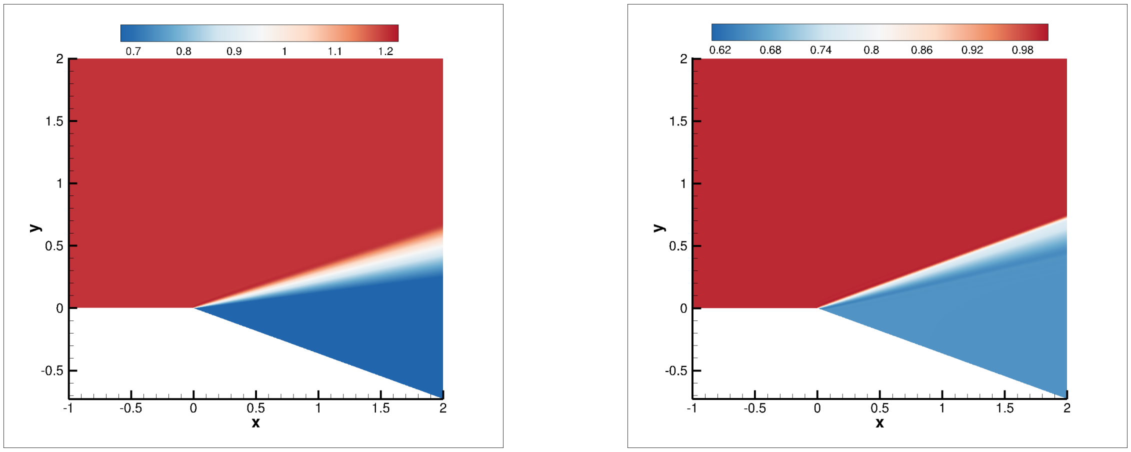

(a) (b)

Figure 5.27: Pressure contour (a) C2 (b) NC2

Figure 5.27 - 5.29 show the results for Cases C2 and NC2. In both cases, the initial conditions are the same as in Cases C1 and NC1 but the deflection angle θ is increased from -7^o to -20^o as shown in figure 5.22. In Case C2, an expansion fan is still centered at the corner. But to compensate for a larger turning angle, the expansion fan spreads wider compared to the expansion fan in C1, see figure 5.23a and 5.28a. Figure 5.27b, however reveals a expansion shock-fan combination centered at the corner. Figure 5.28b shows that the flow is first expanded from $\Gamma < 0$ to $\Gamma > 0$ by an expansion shock and then is further expanded through the expansion fan. The contour line is plotted in figure 5.29a to better distinguish the expansion shock and expansion fan. The pressure distribution at $y = 0.2$ is plotted in figure 5.29b. It be can be clearly seen that the pressure drops from 1 to approximately 0.75 and then keep drooping smoothly from 0.75 to 0.65 through.

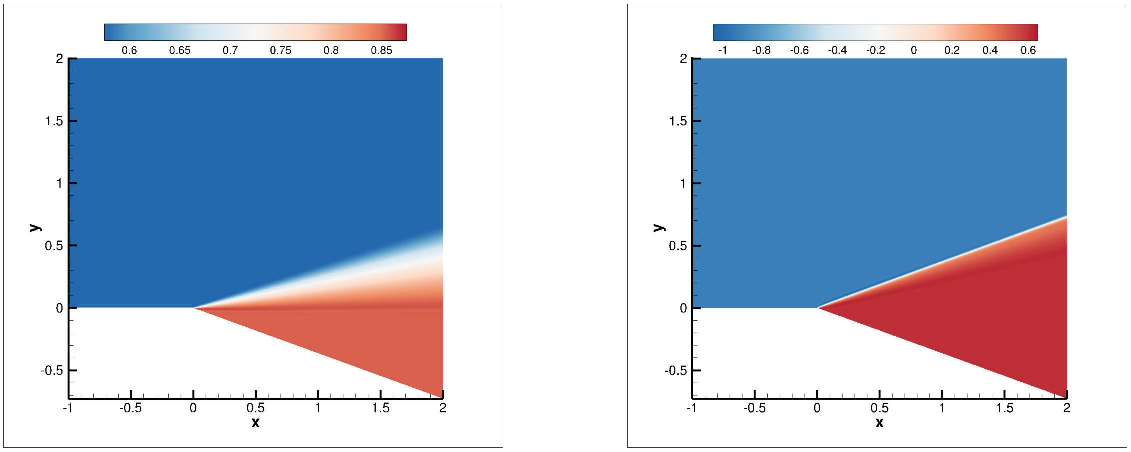

(a) (b)

Figure 5.28: Fundamental derivative Γ contour (a) C2 (b) NC2

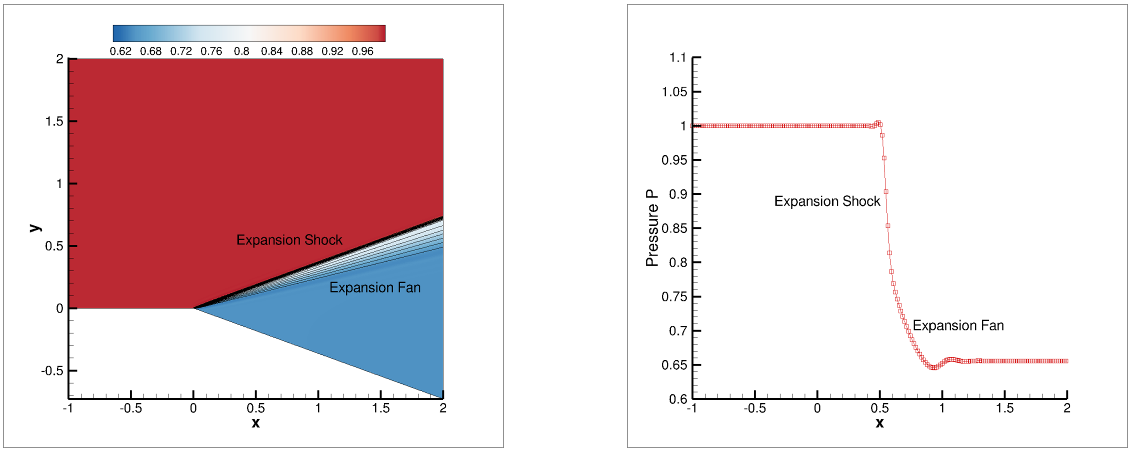

(a) (b)

Figure 5.29: (a) NC2 pressure contour (b) NC2 pressure distribution at $y = 0.2$

5.3.2 Compression Corner

The initial conditions of flow over a compression corner are given in Table 5.3. The geometry consists of a simple domain with a 10^o compression corner. Three Mach numbers are considered for both classical and non-classical cases. The classical and non-classical gas flow fields are compared in Figures 5.31 - 5.38.

Table 5.3: Initial conditions for flow over the compression ramp

Case	$\frac{p}{p_c}$	$\frac{v}{v_c}$	Γ	M	Deflection δ
C1	0.9	2.5	0.662	1.3	10^o
C2	0.9	2.5	0.662	2	10^o
C3	0.9	2.5	0.662	1.1	10^o
NC1	0.9	1.6	-0.476	1.3	10^o
NC2	0.9	1.6	-0.476	2	10^o
NC3	0.9	1.6	-0.476	1.05	10^o

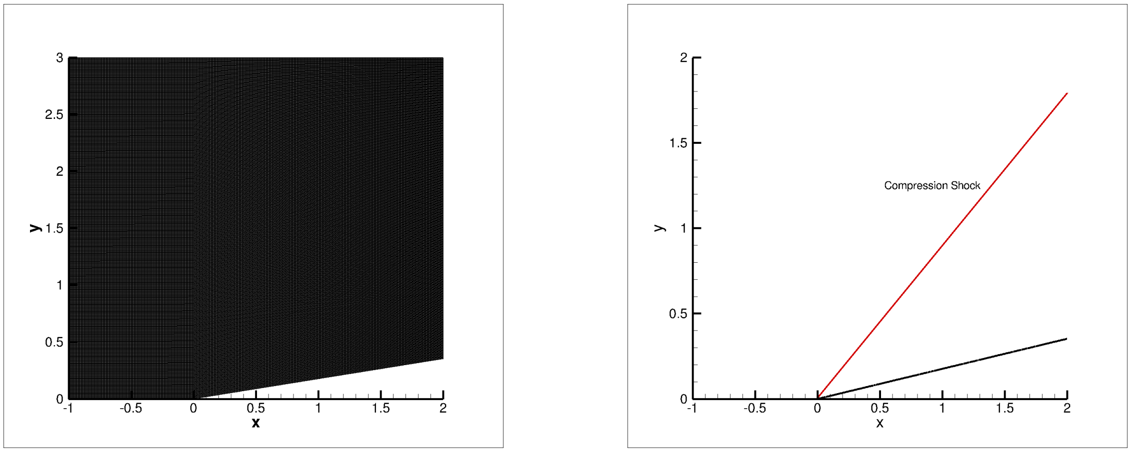

(a) (b)

Figure 5.30: (a) Computational domain for compression ramp and (b) Schematic wave field for flow over compression ramp in classical region

Free-stream state is chosen such that $\Gamma > 0$ for case C1 and $\Gamma < 0$ for case NC1. Free-stream Mach number is 1.4 for C1 and 1.3 for NC1. Figure 5.31 compares the pressure fields between C1 and NC1. An oblique compression shock attached to the corner is shown in figure 5.31a. An entropy jump can be observed in the entropy contour (see Figure 5.32a). Figure 5.31b show that flow is compressed smoothly through a compression fan centered at the corner. The entropy contour in Figure 5.32b confirms that the compression process in NC1 is completely isentropic. This agrees with the theory for non-classical gas as discussed in chapter 3.

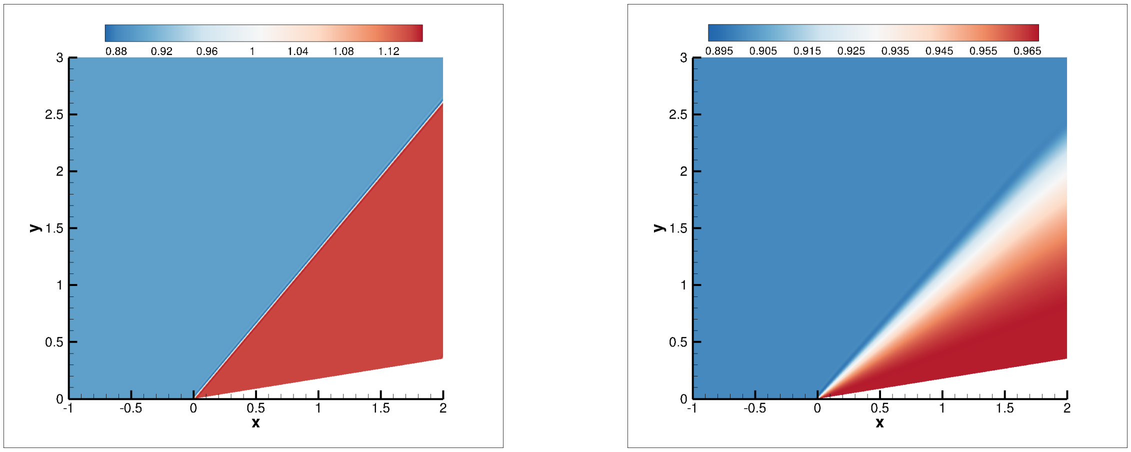

(a) (b)

Figure 5.31: Pressure contour (a) C1 (b) NC1

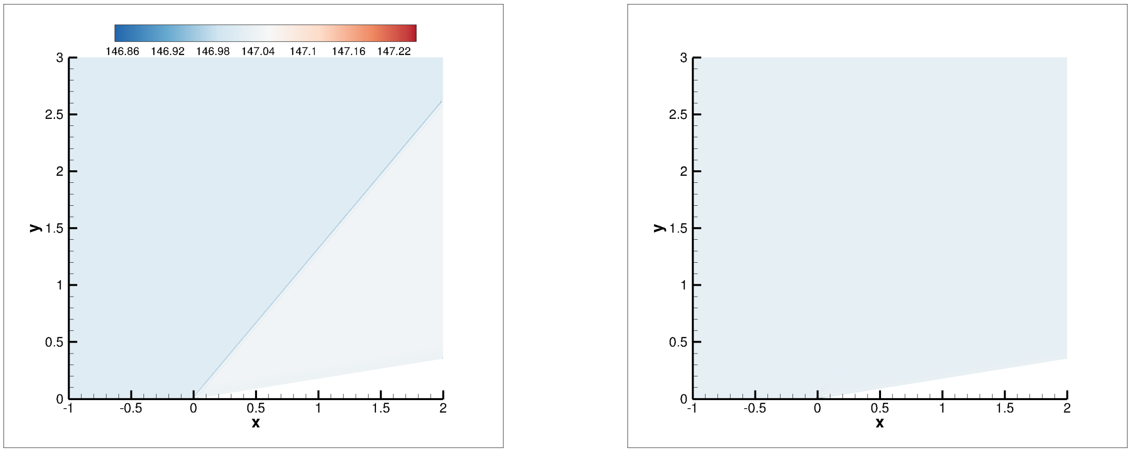

(a) (b)

Figure 5.32: Entropy contour (a) C1 (b) NC1

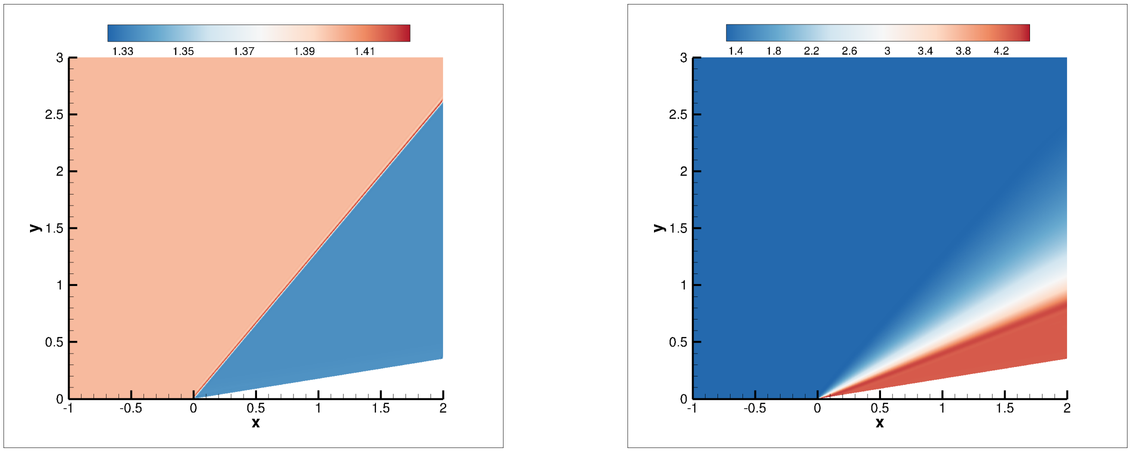

(a) (b)

Figure 5.33: Mach number contour (a) C1 (b) NC1

In Case C2 and NC2, pressure and density are kept the same as in Case C1 and NC1 while Mach number is increased to 2.0 for both cases. As expected, fluid is still compressed through a compression oblique shock in Case C2. The compression oblique shock angle is smaller comparing to the angle in Case C2. This agrees with the $\theta - \beta - M$ relation as shown in Figure 5.33. For the same deflection angle, the shock angle decreases when the freestream Mach number increases. At the same time, the Mach number increases from 2 to 2.13 for the BZT gas, which is opposite to the classical gas theory where the Mach number always decreases across an oblique shock. The same phenomenon is also observed in Case NC1 and Case NC2 (see Figure 5.33b). Recall equation (1.2), the fundamental derivative Γ is related to the dependence of sound speed on pressure on an isentrope. For an ideal gas Γ is always greater than unity and therefore sound speed always monotonically increases when pressure increase in an isentropic process. However, for gas with $0 < \Gamma < 1$ or $\Gamma < 0$, sound speed no longer increases with pressure increase. Instead, sound speed drops with pressure increase. Velocity decreases when the fluid is compressed through a compression shock or a compression fan but the sound speed also decreases as shown in Figure 5.35b. When the change in sound speed is larger than the change in velocity in the compression process, Mach number will increase. Gori [24] reported the same findings for MDM by solving the oblique shock relations using Van der Waals EOS. But their work focus on the analytical solution of obliques shock in the non-ideal region only($0 < \Gamma < 1$).

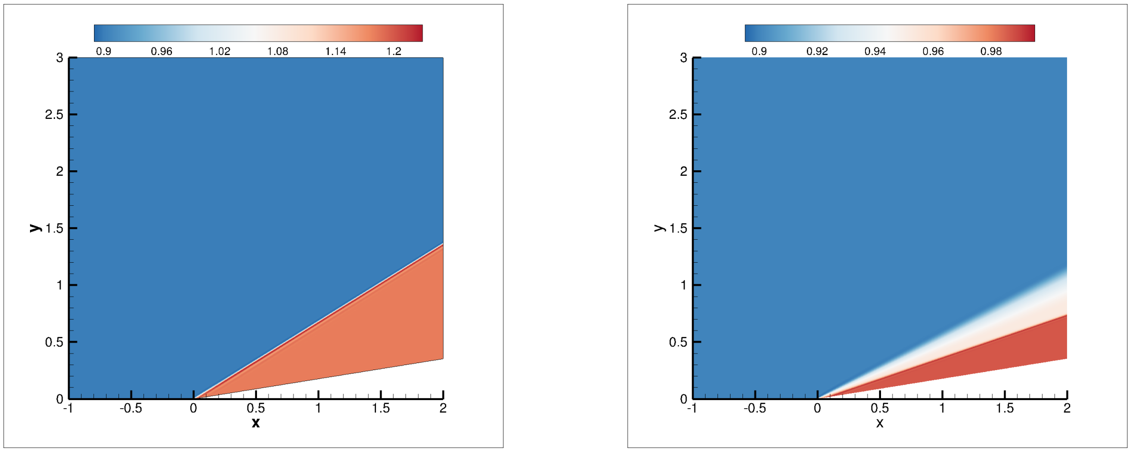

(a) (b)

Figure 5.34: Pressure contour (a) C2 (b) NC2

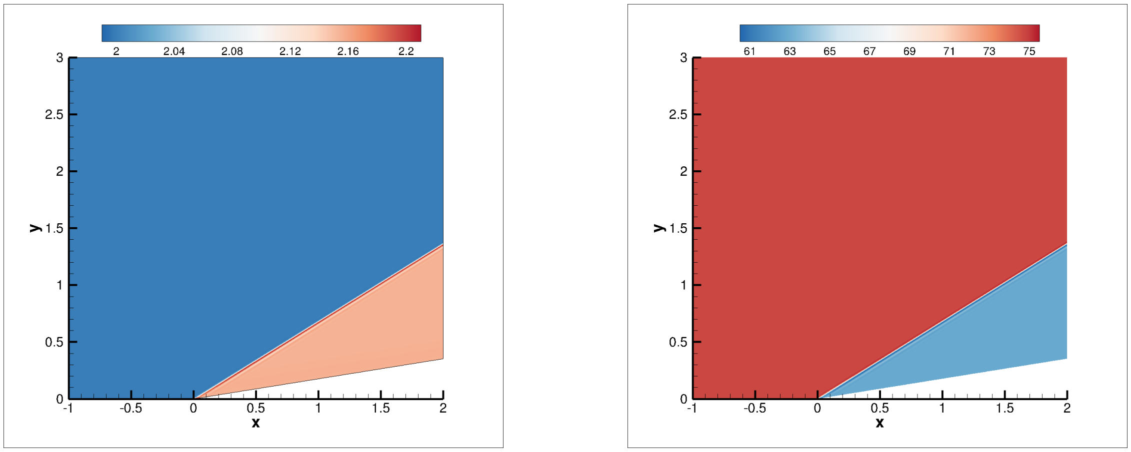

(a) (b)

Figure 5.35: (a) C2 Mach number contour (b) C2 Sound speed contour

In Case NC2, a compression fan-shock is centered at the corner. The fluid is first compressed by a compression fan from $\Gamma < 0$ to $\Gamma > 0$, then it is compressed through the compression shock. The contour lines are marked in Figure 5.37a. The pressure distribution is plotted in Figure 5.37b, where it can be seen clearly that the pressure increases smoothly from 0.9 to 0.95 first and then increases from 0.95 to 0.99 suddenly through a discontinuity. This further confirms the compression fan-shock structure in Case NC2.

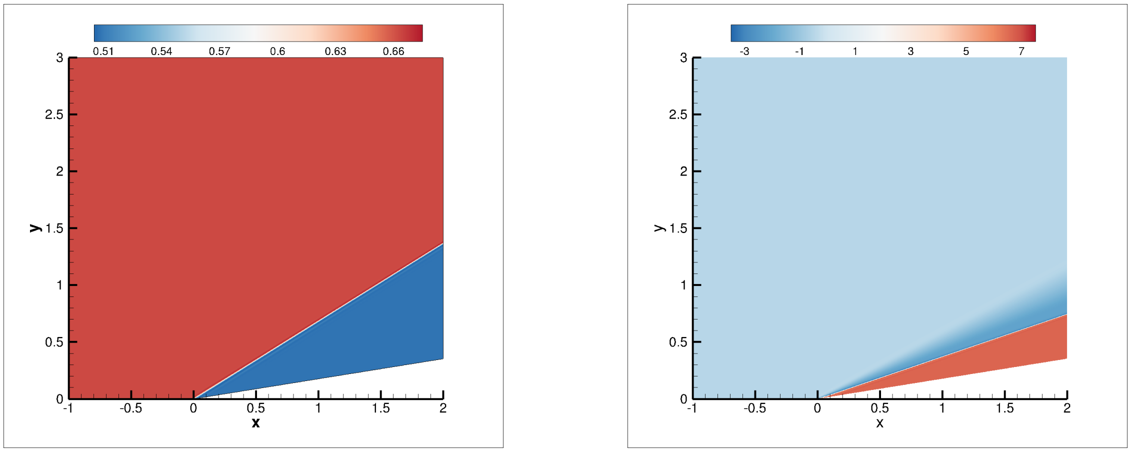

(a) (b)

Figure 5.36: Fundamental derivative Γ contour (a) C2 (b) NC2

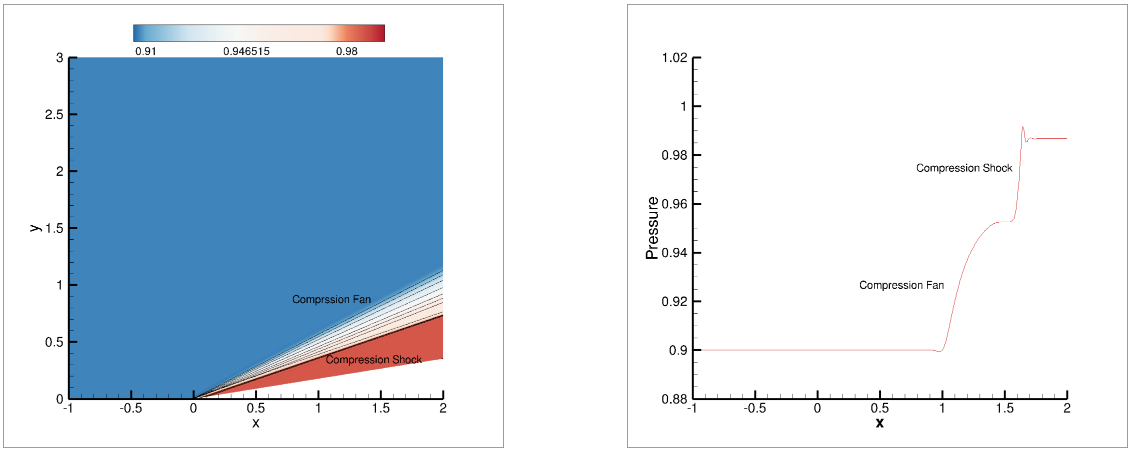

(a) (b)

Figure 5.37: Case NC2 (a) Pressure contour with compression fan and compression shock marked (b) Pressure distribution along $y = 0.5$

Deflection angle is still 10^o for the last two cases C3 and NC3. The free-stream pressure and density remain the same while the Mach number is decreased to 1.1 and 1.05 for C3 and NC3 respectively. As shown in Figure 5.33, the max deflection angle θ_{max} decreases when the Mach number decreases. Therefore, if the Mach number is small enough, the deflection angle of the corner is greater than the max deflection angle. The oblique shock is expected to detach in this case for the classical gas. Figure 5.38a confirms the detached shock for case C3 where the free-stream fluid is in the classical region. Figure 5.38b show that for flow in non-classical region, as Mach number decreases, a compression fan still forms centering at the corner. Due to the non-monotonic dependence of sound speed on pressure, the Mach number increases to a much higher value after the compression fan as shown in Figure 5.39b.

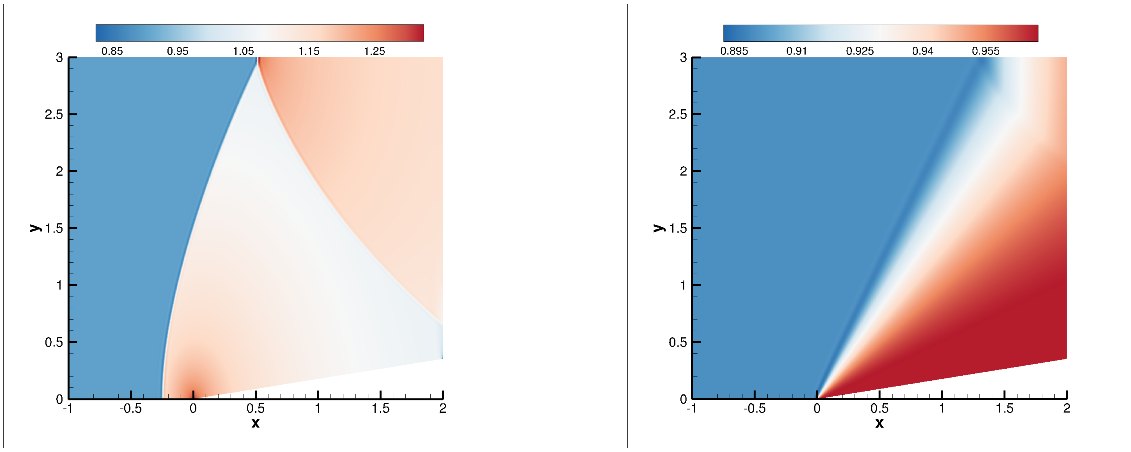

(a)

(b)

Figure 5.38: Pressure contour (a) C3 (b) NC3

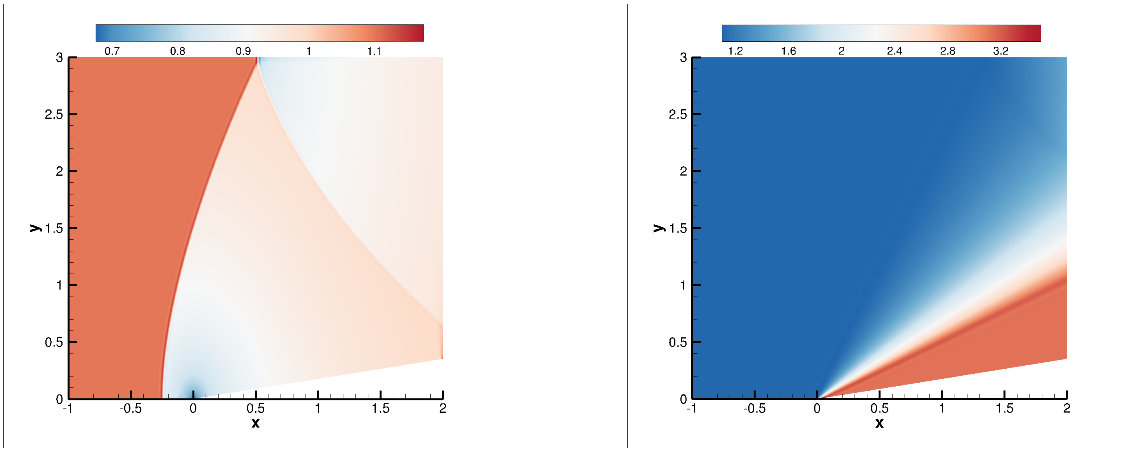

(a)

(b)

Figure 5.39: Mach number contour (a) C3 (b) NC3

Figure 5.31b and Figure 5.34b show that with incoming flow Mach number increase, a compression fan becomes a compression fan-shock. In Case NC4, upstream pressure and density remain the same while Mach number is increased to 5. The results are reported in Figure 5.40. As shown in Figure 5.40a, the wave fields contains only one single compression shock without any compression fan in front of it. Mach number decreases across the shock wave and the fundamental derivative Γ of the flow jumps from negative to positive.

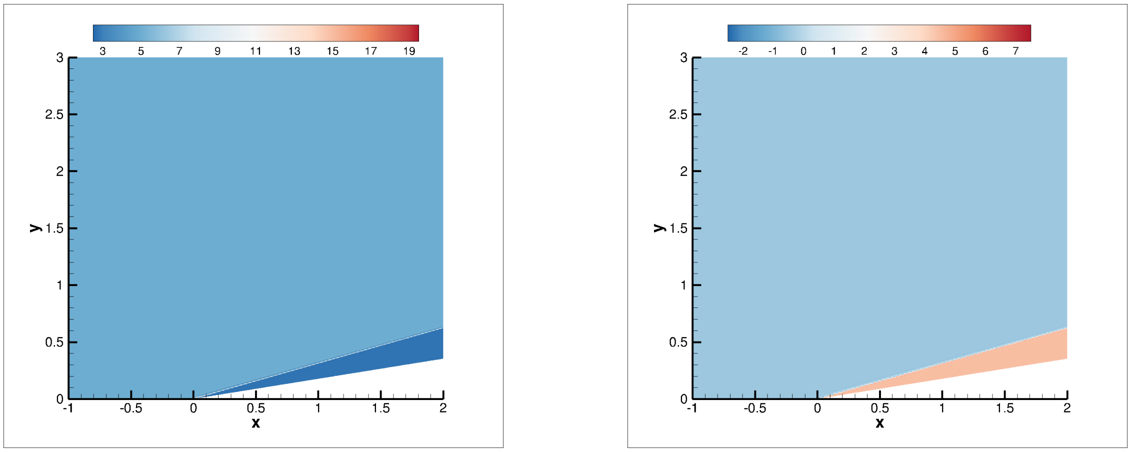

(a) (b)

Figure 5.40: (a) NC4 Mach number contour (b) NC4 Fundamental derivative Γ contour

5.4 Flow Over a Circular Bump

In the previous section, the possible wave fields of flow over a expansion and compression corner are mapped out. Only one single wave structure can appear in the flow over corners. To compare more complicated wavefield between the classical and non-classical region, the flow over a circular bump is considered in this section. The geometry can be fonud in Figure 5.41. The initial conditions considered here are in Table 5.4.

Table 5.4: Initial conditions for flow over arc

Case	$\frac{p}{p_c}$	$\frac{v}{v_c}$	Γ	M
C1	1.2	1.7	0.558	2
NC1	0.9	1.6	-0.476	2

In Case C1, we first consider the flow of a gas in the classical region with $0 < \Gamma < 1$. With incoming Mach number of 2.0 as shown in Figure 5.43a, a compression shock is attached to the leading edge of the bump and followed by expansion fan on the curved surface. Flow is expanded smoothly until it encounter a compression shock attached to the trailing edge

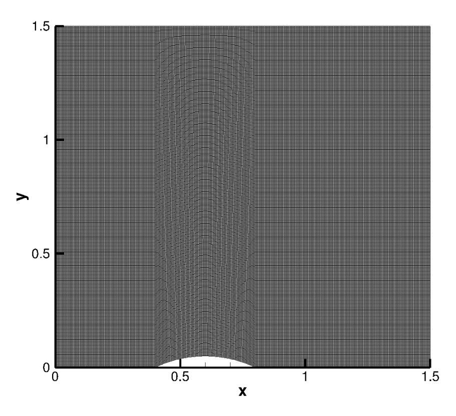

Figure 5.41: Computational domain

of bump. The fundamental derivative stays positive for the entire flow field. For the Case NC1, the incoming flow is in the non-classical region with $\Gamma = -0.476$. A compression forms attached to the leading edge. This attached compression shock splits into compression fan-shock when the flow is away from the bump. Note that fundamental derivative changes its sign across the compression shock and compression fan-shock. The flow then forms an expansion shock which expands flow through the $\Gamma < 0$ region.

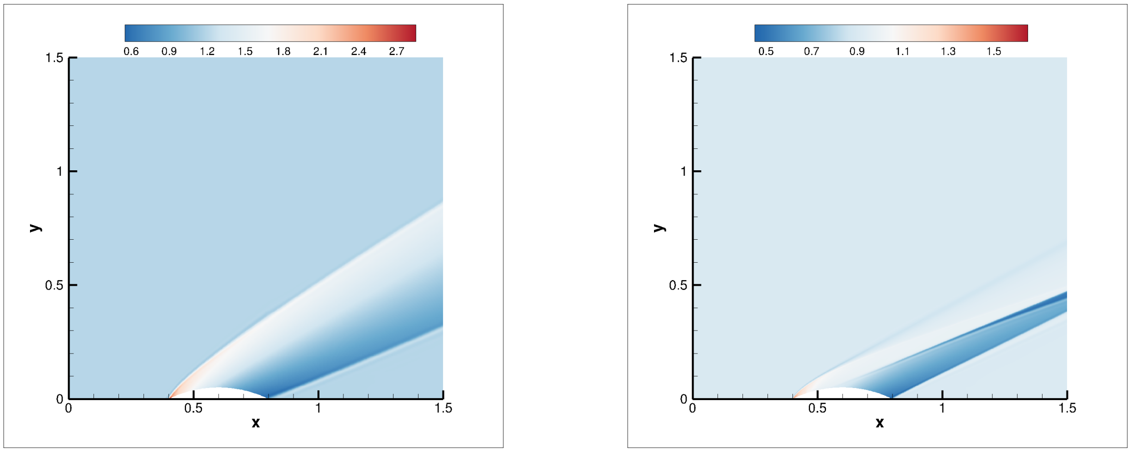

(a) (b)

Figure 5.42: Pressure contour (a) C1 (b) NC1

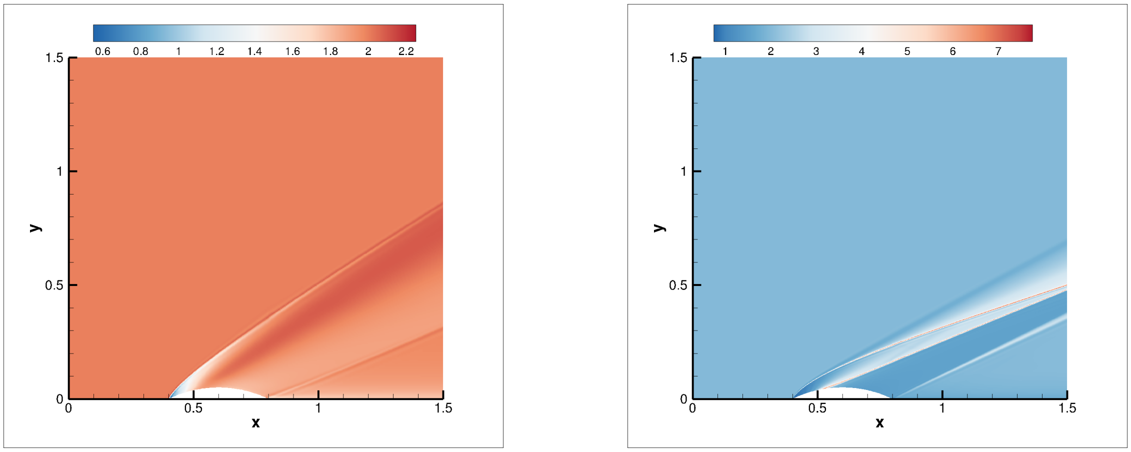

(a) (b)

Figure 5.43: Mach number contour (a) C1 (b) NC1

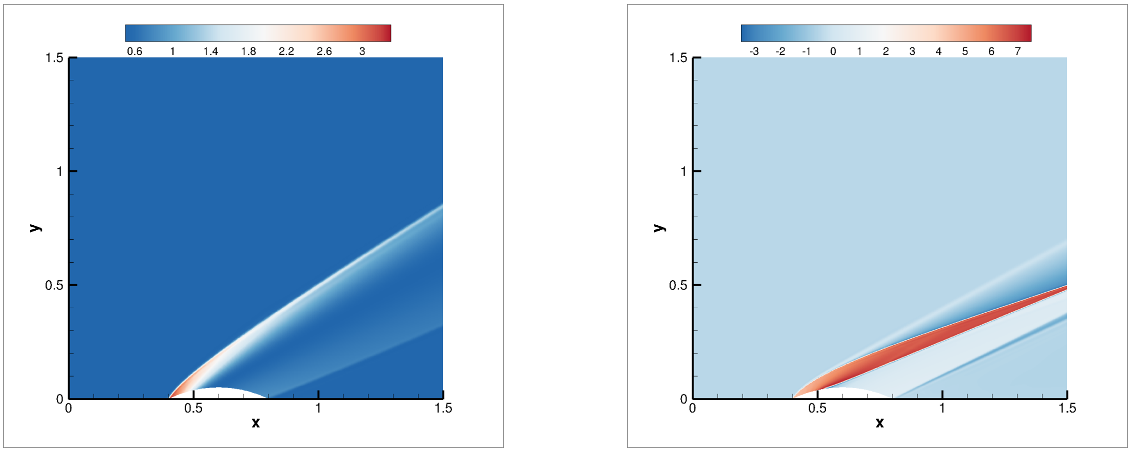

(a) (b)

Figure 5.44: FD contour (a) C1 (b) NC1

Chapter 6

Conclusions and Future Work

6.1 Conclusions

In this dissertation, different topics related to the non-classical gasdynamics of BZT gases have been investigated. In chapter 2, real gas effect is examined by comparing thermodynamic properties of CO_2 from National Institute of Standards and Technology (NIST) with the properties calculated by ideal gas equation of state and Soave–Redlich–Kwong (SRK) equation of state. Distribution of compressibility factor Z shows that the fluid deviates from idea gas behavior the most near saturation vapor line. The formula for the fundamental derivative computation is then derived. The fundamental derivative is computed using SRK, Peng Robinson and Van der Waals. Regions of $\Gamma < 0$, $0 < \Gamma < 1$ and $1 < \Gamma$ are identified and mapped out in the p-v diagram. The result shows for fluids such as siloxanes, there exists a region with negative fundamental derivative near the saturation line. Such gas is named as Bethe-Zel'dovich-Thompson gas. The BZT regions predicted by the Van der Waals equation of state gives the largest area in $p - v$ diagram. Analysis also shows that fluids with higher molecular complexity tend to have larger BZT regions.

In Chapter 3, unconventional gas behaviors of the isentropic quasi-1D nozzle flow have been investigated systematically and in depth for a typical BZT gas, the MDM gas using the Van der Waals real gas equation of state. The flow behavior of a dense gas is different from ordinary gas dynamics, and those regions are divided by two significant demarcation lines of Γ marked out in the p-v plane, $\Gamma = 0$ and $\Gamma = 1$.

- When $\Gamma > 1$, the gas behaves the same way as the conventional theory predicts.
- When $\Gamma < 1$, the speed of sound decreases with increasing pressure, and the Mach number is no longer a monotonic function of flow velocity. Meanwhile, the relations between the velocity and cross-sectional area change is different. More specifically, it can be divided into two conditions. For $M^2 < \dfrac{1}{1-\Gamma}$, the gas behaves the same way as a conventional gas. The Mach number increases with increasing velocity, as well a converging channel accelerates a subsonic flow and decelerates a supersonic flow. For $M^2 > \dfrac{1}{1-\Gamma}$, the flow behaves in the complete opposite way to the classical theory. The Mach number decreases with increasing velocity, as well a diverging channel accelerates a subsonic flow and decelerates a supersonic flow.
- When $\Gamma < 0$, the nozzle geometry at the transonic location is changed. To accelerate a subsonic flow to supersonic, or vice versa, the divergent-convergent nozzle is needed instead of the traditional convergent-divergent nozzle.

Notice that multiple of the above non-classical gas dynamic behaviors may appear in one channel flow case. Sometimes, there is more than one sonic point in the nozzle and hence multiple throats are needed to accelerate the flow. In Chapter 4, the formation of an expansion shock is explained from the perspective of wave propagation. When $\Gamma < 0$, an expansion shock can satisfy the wave speed ordering and entropy condition. Due to the sign change of the isentrope curvature (i.e., from $\Gamma < 0$ to $\Gamma > 0$ or the opposite), more complicated wave structure, such as sonic shock, double sonic shock, fan-shock, shock-fan, and fan-shock-fan, are possible. The jump relation for the BZT gas is solved numerically and it shows that if the pre-shock state is located in the non-classical region $\Gamma < 0$, the speed of sound increases with the decrease of density along the shock adiabat thus allowing physically possible expansion shocks. Moreover, the entropy generation in an expansion shock is negligibly small. The expansion shock allows a BZT fluid to be accelerated suddenly through a shock wave without significant loss generation. A double sonic shock is confirmed numerically with the Van der Waals equation of state. A BZT gas can be expanded through a discontinuity while maintaining unity Mach number for both upstream and downstream of the discontinuity.

In chapter 5, A real gas numerical solver using Jameson-Schmidt-Turkel scheme developed. The dense gas shock tube simulations show complex, unsteady wave fields unlike those expected for a perfect gas. Mixed wave phenomena, such as an expansion shock followed by an expansion fan, are confirmed numerically. Steady computations are performed on flow over the expansion and compression corners. Results confirms all possible wave fields for various upstream conditions. For flow in the non-classical region and a given deflection angle, the wave structure may change from a compression shock to a compression fan-shock, and to a compression fan as the Mach number decreases.

The analytical and numerical results of this work provide clarification of the behaviors of a dense gas near its critical point and data to help prove the unusual behavior of a real gas in possible BZT regions.

6.2 Future Work

Futures studies can build upon this one in several ways. The first thing to consider is implementing more complicated or experiment-based thermodynamic models in the solver for obtaining more accurate solutions. REFPROP [85] is a good choice as they provides very accurate thermodynamic properties based on experimental data and provides libraries that could be directly used in the solver. However, it could be computational costly. In the past few years, machine learning has been widely used in CFD [86][87][88]. With more experimental data available for the dense gas in the future, another choice is to implement a machine learning model to replace the thermodynamic model. Another extension of this work is to consider the viscous effect for the dense gas. Results in this dissertation are obtained by solving the inviscid Euler equation. The expansion shock has a negligible entropy jump comparing to the compression shock. It is still questionable if such solution exist and is stable when viscous effect kicks in. The wave interaction in the dense gas flow is another interesting topic to explore as dense gas can exhibits much more complex wave fields such as fan-shock. The CFD solver with the enhanced gas model should then be used to analyze or optimize the design of compressor and turbine blade rows in turbomachines used in future sCO_2 or Organic Rankine cycle engines.

Bibliography

[1] Bob Dudley et al. Bp statistical review of world energy. *BP statistical review, London, UK, accessed Aug*, 6(2018):00116, 2018.

[2] Shell. World energy model: a view to 2100. Technical report, 2017.

[3] Frederica Perera. Pollution from fossil-fuel combustion is the leading environmental threat to global pediatric health and equity: Solutions exist. *International journal of environmental research and public health*, 15(1):16, 2018.

[4] The hidden costs of fossil fuels. *Union of Concerned Scientists*, 2016.

[5] EPA US. Report on the environment. Technical report, 2009.

[6] A Mahmoudi, M Fazli, and MR Morad. A recent review of waste heat recovery by organic rankine cycle. *Applied Thermal Engineering*, 143:660–675, 2018.

[7] N Galanis, E Cayer, Pet al Roy, ES Denis, and M Desilets. Electricity generation from low temperature sources. *Journal of applied fluid mechanics*, 2(2):55–67, 2012.

[8] Vaclav Dostal, Pavel Hejzlar, and Michael J Driscoll. The supercritical carbon dioxide power cycle: comparison to other advanced power cycles. *Nuclear technology*, 154(3):283–301, 2006.

[9] Ernest G Feher. The supercritical thermodynamic power cycle. *Energy conversion*, 8(2):85–90, 1968.

[10] Francesco Crespi, Giacomo Gavagnin, David Sánchez, and Gonzalo S Martínez. Supercritical carbon dioxide cycles for power generation: A review. *Applied energy*, 195:152–183, 2017.

[11] Steven Lecompte, Henk Huisseune, Martijn Van Den Broek, Bruno Vanslambrouck, and Michel De Paepe. Review of organic rankine cycle (orc) architectures for waste heat recovery. *Renewable and sustainable energy reviews*, 47:448–461, 2015.

[12] O Badr, SD Probert, and PW O'callaghan. Selecting a working fluid for a rankine-cycle engine. *Applied Energy*, 21(1):1–42, 1985.

[13] James Freeman, Klaus Hellgardt, and Christos N Markides. An assessment of solar-powered organic rankine cycle systems for combined heating and power in uk domestic applications. *Applied Energy*, 138:605–620, 2015.

[14] Chayadit Pumaneratkul, Haruhiko Yamasaki, Hiroshi Yamaguchi, Shinichi Kitamura, and Yoshihiro Sako. Supercritical co2 rankine cycle system with low-temperature geothermal heat pipe. *Energy Procedia*, 105:1029–1036, 2017.

[15] Reginald Ivan Lewis. *Turbomachinery performance analysis.* Butterworth-Heinemann, 1996.

[16] Michael J Moran, Howard N Shapiro, Daisie D Boettner, and Margaret B Bailey. *Fundamentals of engineering thermodynamics.* John Wiley & Sons, 2010.

[17] Giorgio Soave. Equilibrium constants from a modified redlich-kwong equation of state. *Chemical engineering science*, 27(6):1197–1203, 1972.

[18] Roland Span and Wolfgang Wagner. A new equation of state for carbon dioxide covering the fluid region from the triple-point temperature to 1100 k at pressures up to 800 mpa. *Journal of physical and chemical reference data*, 25(6):1509–1596, 1996.

[19] Ding-Yu Peng and Donald B Robinson. A new two-constant equation of state. *Industrial & Engineering Chemistry Fundamentals*, 15(1):59–64, 1976.

[20] Philip A Thompson. A fundamental derivative in gasdynamics. *The Physics of Fluids*, 14(9):1843–1849, 1971.

[21] P Colonna and ALBERTO Guardone. Molecular interpretation of nonclassical gas dynamics of dense vapors under the van der waals model. *Physics of Fluids*, 18(5):056101, 2006.

[22] Huan Xi, Ming-Jia Li, Chao Xu, and Ya-Ling He. Parametric optimization of regenerative organic rankine cycle (orc) for low grade waste heat recovery using genetic algorithm. *Energy*, 58:473–482, 2013.

[23] Alberto Guardone, Andrea Spinelli, and Vincenzo Dossena. Influence of molecular complexity on nozzle design for an organic vapor wind tunnel. *Journal of engineering for gas turbines and power*, 135(4), 2013.

[24] Giulio Gori, Davide Vimercati, and ALBERTO Guardone. Non-ideal compressible-fluid effects in oblique shock waves. In *Journal of Physics: Conference Series*, volume 821, page 012003. IOP Publishing, 2017.

[25] HA Bethe. The theory of shock waves for an arbitrary equation of state. technical paper 545, office sci. *Res. & Dev*, 1942.

[26] Ya B Zel'dovich. Theory of shock waves and introduction to gas dynamics [in russian], izd. *AN SSSR, Moscow*, 946, 1946.

[27] KC Lambrakis and PA Thompson. Existence of real uids with a negative fundamental derivative γ. *Physics of Fluids*, 15(5):933.

[28] P Colonna, ALBERTO Guardone, and NR Nannan. Siloxanes: a new class of candidate bethe-zel'dovich-thompson fluids. *Physics of Fluids*, 19(8):086102, 2007.

[29] Hugh Longbourne Callendar. On the thermodynamical properties of gases and vapours as deduced from a modified form of the joule-thomson equation, with special reference to the properties of steam. *Proceedings of the Royal Society of London*, 67(435-441):266–286, 1901.

[30] DA Sullivan. Historical review of real-fluid isentropic flow models. *Journal of Fluids Engineering*, 103(2):258–267, 1981.

[31] V Arp, JM Persichetti, and Guo-bang Chen. The gruneisen parameter in fluids. *Journal of fluids engineering*, 106(2):193–200, 1984.

[32] E Grüneisen. Zustand des festen körpers. In *Thermische Eigenschaften der Stoffe*, pages 1–59. Springer, 1926.

[33] JC Leung and M Epstein. A generalized critical flow model for nonideal gases. *AIChE journal*, 34(9):1568–1572, 1988.

[34] Robert C Johnson. Calculations of real-gas effects in flow through critical-flow nozzles. *Journal of Basic Engineering*, 86(21):519–526, 1964.

[35] W Bober and WL Chow. Nonideal isentropic gas flow through converging-diverging nozzles. *Journal of fluids engineering*, 112(4):455–460, 1990.

[36] William A Sirignano. Normal shocks with high upstream pressure. *Physical Review Fluids*, 3(9):093401, 2018.

[37] William A Sirignano. Compressible flow at high pressure with linear equation of state. *Journal of Fluid Mechanics*, 843:244–292, 2018.

[38] Al A Borisov, Al A Borisov, SS Kutateladze, and VE Nakoryakov. Rarefaction shock wave near the critical liquid–vapour point. *Journal of Fluid Mechanics*, 126:59–73, 1983.

[39] SS Kutateladze, VE Nakoryakov, and AA Borisov. Rarefaction waves in liquid and gas-liquid media. *Annual review of fluid mechanics*, 19(1):577–600, 1987.

[40] MS Cramer. Negative nonlinearity in selected fluorocarbons. *Physics of Fluids A: Fluid Dynamics*, 1(11):1894–1897, 1989.

[41] Mark S Cramer, A Kluwick, Layne T Watson, and Wolfgang Pelz. Dissipative waves in fluids having both positive and negative nonlinearity. *Journal of Fluid Mechanics*, 169:323–336, 1986.

[42] Stephen Fergason, Alberto Guardone, and Brian Argrow. Construction and validation of a dense gas shock tube. *Journal of thermophysics and heat transfer*, 17(3):326–333, 2003.

[43] Tiemo Mathijssen. Experimental observation of non-ideal compressible fluid dynamics: with application in organic rankine cycle power systems. 2017.

[44] P Colonna, A Guardone, NR Nannan, and C Zamfirescu. Design of the dense gas flexible asymmetric shock tube. *Journal of fluids engineering*, 130(3), 2008.

[45] Andrea Spinelli, Vincenzo Dossena, Paolo Gaetani, Carlo Osnaghi, and D Colombo. Design of a test rig for organic vapours. In *Turbo Expo: Power for Land, Sea, and Air*, volume 44007, pages 109–120, 2010.

[46] Andrea Spinelli, Giorgia Cammi, Marta Zocca, Simone Gallarini, Fabio Cozzi, Paolo Gaetani, Vincenzo Dossena, and Alberto Guardone. Experimental observation of non-ideal expanding flows of siloxane mdm vapor for orc applications. *Energy Procedia*, 129:1125–1132, 2017.

[47] Andrea Spinelli, Fabio Cozzi, Giorgia Cammi, Marta Zocca, Paolo Gaetani, Vincenzo Dossena, and Alberto Guardone. Preliminary characterization of an expanding flow of siloxane vapor mdm. In *Journal of Physics: Conference Series*, volume 821, page 012022. IOP Publishing, 2017.

[48] BM Argrow. Computational analysis of dense gas shock tube flow. *Shock Waves*, 6(4):241–248, 1996.

[49] AC Aldo and BM Argrow. Dense gas flow in minimum length nozzles. 1995.

[50] Andrew C Aldo and Brian M Argrow. Supersonic minimum length nozzle design for dense gases. 1993.

[51] BP Brown and BM Argrow. Two-dimensional shock tube flow for dense gases. *Journal of Fluid Mechanics*, 349:95–115, 1997.

[52] Brady P Brown and Brian M Argrow. Nonclassical dense gas flows for simple geometries. *AIAA journal*, 36(10):1842–1847, 1998.

[53] Brady P Brown and Brian M Argrow. Application of bethe-zel'dovich-thompson fluids in organic rankine cycle engines. *Journal of Propulsion and Power*, 16(6):1118–1124, 2000.

[54] Stephen Fergason and Brian Argrow. Simulations of nonclassical dense gas dynamics. In *35th AIAA Thermophysics Conference*, page 2752, 2001.

[55] ALBERTO Guardone, Vittorio Selmin, and Luigi Vigevano. An investigation of roe's linearization and average for ideal and real gases. 1999.

[56] ALBERTO Guardone and Luigi Vigevano. Roe linearization for the van der waals gas. *Journal of Computational Physics*, 175(1):50–78, 2002.

[57] Andrew PS Wheeler and Jonathan Ong. The role of dense gas dynamics on organic rankine cycle turbine performance. *Journal of Engineering for Gas Turbines and Power*, 135(10):102603, 2013.

[58] Piero Colonna and Paolo Silva. Dense gas thermodynamic properties of single and multicomponent fluids for fluid dynamics simulations. *J. Fluids Eng.*, 125(3):414–427, 2003.

[59] G Angelino and C Invernizzi. Cyclic methylsiloxanes as working fluids for space power cycles. 1993.

[60] Alberto Guardone, Piero Colonna, Emiliano Casati, and Enrico Rinaldi. Non-classical gas dynamics of vapour mixtures. *Journal of fluid mechanics*, 741:681–701, 2014.

[61] John David Anderson. *Hypersonic and high temperature gas dynamics*. Aiaa, 2000.

[62] Johannes Diderik Van der Waals. *Over de Continuiteit van den Gas-en Vloeistoftoestand*, volume 1. Sijthoff, 1873.

[63] Otto Redlich and Joseph NS Kwong. On the thermodynamics of solutions. v. an equation of state. fugacities of gaseous solutions. *Chemical reviews*, 44(1):233–244, 1949.

[64] Bruce E Poling, John M Prausnitz, John P O'connell, et al. *The properties of gases and liquids*, volume 5. Mcgraw-hill New York, 2001.

[65] YVC Rao et al. *Chemical engineering thermodynamics*. Universities Press, 1997.

[66] William Sirignano. Normal shocks with high upstream pressure. In *APS Meeting Abstracts*, 2017.

[67] P. A. Thompson. *Compressilbe Fluid Dynamics*. McGraw-Hill, 1988.

[68] ALBERTO Guardone and BM Argrow. Nonclassical gasdynamic region of selected fluorocarbons. *Physics of Fluids*, 17(11):116102, 2005.

[69] Philip A Thompson, Garry C Carofano, and Yoon-Gon Kim. Shock waves and phase changes in a large-heat-capacity fluid emerging from a tube. *Journal of Fluid Mechanics*, 166:57–92, 1986.

[70] Hans Albrecht Bethe. On the theory of shock waves for an arbitrary equation of state. In *Classic papers in shock compression science*, pages 421–495. Springer, 1998.

[71] P Cinnella, PM Congedo, and D Laforgia. Transonic flows of bzt fluids through turbine cascades. In *Computational Fluid Dynamics 2004*, pages 227–232. Springer, 2006.

[72] Luuc Keulen, Elisabeth Mansfield, Ian H Bell, Andrea Spinelli, and Alberto Guardone. Bubble-point measurements and modeling of binary mixtures of linear siloxanes. *Journal of Chemical & Engineering Data*, 63(9):3315–3330, 2018.

[73] Ph A Thompson and KC Lambrakis. Negative shock waves. *Journal of Fluid Mechanics*, 60(1):187–208, 1973.

[74] Alfred Kluwick. Transonic nozzle flow of dense gases. *Journal of Fluid Mechanics*, 247:661–688, 1993.

[75] H Gray Funkhouser. A short account of the history of symmetric functions of roots of equations. *The American mathematical monthly*, 37(7):357–365, 1930.

[76] A Kluwick. Non-ideal compressible fluid dynamics: a challenge for theory. In *Journal of Physics: Conference Series*, volume 821, page 012001. IOP Publishing, 2017.

[77] Philip A Thompson. *Compressible-fluid dynamic*. McGraw-Hill, 1971.

[78] Hans Wolfgang Liepmann and Anatol Roshko. *Elements of gasdynamics*. Courier Corporation, 2001.

[79] MS Cramer and Alfred Kluwick. On the propagation of waves exhibiting both positive and negative nonlinearity. *Journal of Fluid Mechanics*, 142:9–37, 1984.

[80] Mark S Cramer and R Sen. Exact solutions for sonic shocks in van der waals gases. *The Physics of fluids*, 30(2):377–385, 1987.

[81] Antony Jameson, Wolfgang Schmidt, and Eli Turkel. Numerical solution of the euler equations by finite volume methods using runge kutta time stepping schemes. In *14th fluid and plasma dynamics conference*, page 1259, 1981.

[82] RW MacCormack and Bb Baldwin. A numerical method for solving the navier-stokes equations with application to shock-boundary layer interactions. In *13th Aerospace Sciences Meeting*, page 1, 1975.

[83] Richard M Beam and Robert F Warming. An implicit finite-difference algorithm for hyperbolic systems in conservation-law form. *Journal of computational physics*, 22(1):87–110, 1976.

[84] John David Anderson. *Modern compressible flow: with historical perspective*, volume 12. McGraw-Hill New York, 1990.

[85] Eric W Lemmon, Marcia L Huber, and Mark O McLinden. Nist reference fluid thermodynamic and transport properties–refprop. *NIST standard reference database*, 23:v7, 2002.

[86] Zeinab Shadram, Tuan M Nguyen, Athanasios Sideris, and William A Sirignano. Neural network flame closure for a turbulent combustor with unsteady pressure. *AIAA Journal*, 59(2):621–635, 2021.

[87] Galen T Craven, Nicholas Lubbers, Kipton Barros, and Sergei Tretiak. Machine learning approaches for structural and thermodynamic properties of a lennard-jones fluid. *The Journal of Chemical Physics*, 153(10):104502, 2020.

[88] Jiaqi Ding, Nan Xu, Manh Tien Nguyen, Qi Qiao, Yao Shi, Yi He, and Qing Shao. Machine learning for molecular thermodynamics. *Chinese Journal of Chemical Engineering*, 31:227–239, 2021.

Appendix A

Thermodynamic Identities

A.1 Exact Differential and Triple Product Rule

In thermodynamics, there's a set of equations that are derived by application of Euler's reciprocity relation to the thermodynamic characteristic functions. Consider a function described by three variables $F = F(x, y, z)$. It can be differentiated as

$$dF = Adx + Bdy + Cdz \tag{A.1}$$

The exactness criteria for this function states that

$$\left(\frac{\partial A}{\partial y}\right)_{x,z} = \left(\frac{\partial B}{\partial x}\right)_{y,z} \tag{A.2}$$

$$\left(\frac{\partial A}{\partial z}\right)_{x,y} = \left(\frac{\partial C}{\partial x}\right)_{y,z} \tag{A.3}$$

$$\left(\frac{\partial B}{\partial z}\right)_{x,y} = \left(\frac{\partial C}{\partial y}\right)_{x,z} \tag{A.4}$$

where the three variables are related by the triple product relation

$$\left(\frac{\partial x}{\partial y}\right)_z \left(\frac{\partial y}{\partial z}\right)_x \left(\frac{\partial z}{\partial x}\right)_y = -1 \tag{A.5}$$

A.2 Maxwell Relations

The general form of Gibbs equation gives that

$$du = Tds - pdv \tag{A.6}$$

$$dh = vdp + Tds \tag{A.7}$$

By applying exactness criteria, the four most common Maxwell relations are

$$\left(\frac{\partial T}{\partial v}\right)_s = -\left(\frac{\partial p}{\partial s}\right)_v \tag{A.8}$$

$$\left(\frac{\partial T}{\partial p}\right)_s = \left(\frac{\partial v}{\partial s}\right)_p \tag{A.9}$$

$$\left(\frac{\partial s}{\partial v}\right)_T = \left(\frac{\partial p}{\partial T}\right)_v \tag{A.10}$$

$$\left(\frac{\partial s}{\partial p}\right)_T = -\left(\frac{\partial v}{\partial T}\right)_p \tag{A.11}$$

A.3 Derivation of Fundamental Derivative

Fundamental derivative Γ is defined as

$$\Gamma = \frac{v^3}{2c^2}\left(\frac{\partial^2 p}{\partial v^2}\right)_s$$

To derive $\left(\frac{\partial^2 p}{\partial v^2}\right)_s$ in terms of thermodynamic state variables, start with the first order derivative along the isentrope $\left(\frac{\partial p}{\partial v}\right)_s$.

$$
\begin{aligned}
\left(\frac{\partial p}{\partial v}\right)_s &= -\left(\frac{\partial p}{\partial s}\right)_v \left(\frac{\partial s}{\partial v}\right)_p \\
&= \left(\frac{\partial T}{\partial v}\right)_s \left(\frac{\partial p}{\partial T}\right)_s \\
&= \left(\frac{\partial T}{\partial s}\right)_v \left(\frac{\partial s}{\partial v}\right)_T \left(\frac{\partial p}{\partial s}\right)_T \left(\frac{\partial s}{\partial T}\right)_p \\
&= -\frac{T}{c_v} \left(\frac{\partial p}{\partial T}\right)_v \left(\frac{\partial T}{\partial v}\right)_p \frac{c_p}{T} \\
&= -\frac{c_p}{c_v} \left(\frac{\partial v}{\partial T}\right)_p \left(\frac{\partial p}{\partial v}\right)_T \left(\frac{\partial p}{\partial v}\right)_T \left(\frac{\partial T}{\partial p}\right)_v \\
&= -\left[1 + \frac{T}{c_v} \left(\frac{\partial v}{\partial T}\right)_p \left(\frac{\partial p}{\partial T}\right)_v\right] \left[\left(\frac{\partial v}{\partial T}\right)_p \left(\frac{\partial p}{\partial v}\right)_T^2 \left(\frac{\partial T}{\partial p}\right)_v\right] \\
&= \left(\frac{\partial p}{\partial v}\right)_T + \frac{T}{c_v} \left(\frac{\partial v}{\partial T}\right)_p \left(\frac{\partial p}{\partial T}\right)_v \left(\frac{\partial p}{\partial v}\right)_T \\
&= \left(\frac{\partial p}{\partial v}\right)_T - \frac{T}{c_v} \left(\frac{\partial p}{\partial T}\right)_v^2
\end{aligned}
$$

Then another differentiation gives

$$\begin{aligned}\left(\frac{\partial^2 p}{\partial v^2}\right)_s &= \left(\frac{\partial\left(\left(\frac{\partial p}{\partial v}\right)_T - \frac{T}{c_v}\left(\frac{\partial p}{\partial T}\right)_v^2\right)}{\partial v}\right)_s \\ &= \underbrace{\left(\frac{\partial\left(\left(\frac{\partial p}{\partial v}\right)_s\right)}{\partial v}\right)_T}_{\text{①}} - \frac{1}{c_v}\left(\frac{\partial p}{\partial T}\right)_v^2 \underbrace{\left(\frac{\partial T}{\partial v}\right)_s}_{\text{②}} + \frac{T}{c_v^2}\left(\frac{\partial p}{\partial T}\right)_v^2 \underbrace{\left(\frac{\partial c_v}{\partial v}\right)_s}_{\text{③}} \\ &\quad - \frac{2T}{c_v}\left(\frac{\partial p}{\partial T}\right)_v \underbrace{\left(\frac{\partial\left(\left(\frac{\partial p}{\partial v}\right)_s\right)}{\partial T}\right)_v}_{\text{④}}\end{aligned}$$

The four terms marked in the equation above are derived below. To keep the expression elegant, here $\partial/\partial T$ implies that v is kept constant, and vice versa.

$$\begin{aligned}&\text{①} = \frac{\partial^2 p}{\partial v^2} + \frac{T}{c_v^2}\left(\frac{\partial p}{\partial T}\right)^2 \frac{\partial c_v}{\partial v} - \frac{2T}{c_v}\frac{\partial p}{\partial T}\frac{\partial^2 p}{\partial v \partial T} \\ &\text{②} = -\frac{T}{c_v}\frac{\partial p}{\partial T} \\ &\text{③} = \frac{\partial c_v}{\partial v} - \frac{T}{c_v}\frac{\partial p}{\partial T}\frac{\partial c_v}{\partial T} \\ &\text{④} = \frac{\partial^2 p}{\partial v \partial T} - \frac{1}{c_v}\left(\frac{\partial p}{\partial T}\right)^2 + \frac{T}{c_v^2}\left(\frac{\partial p}{\partial T}\right)^2 \frac{\partial c_v}{\partial T} - \frac{2}{c_v}\frac{\partial p}{\partial T}\frac{\partial c_v}{\partial v}\end{aligned}$$

Substitute the above expressions back into $\left(\frac{\partial^2 p}{\partial v^2}\right)_s$ and reorganize the equation, we obtain

$$\left(\frac{\partial^2 p}{\partial v^2}\right)_s = \frac{\partial^2 p}{\partial v^2} - \frac{3T}{c_v}\frac{\partial p}{\partial T}\frac{\partial^2 p}{\partial v \partial T} + \left(\frac{T}{c_v}\frac{\partial p}{\partial T}\right)^2 \left[\frac{3}{T}\frac{\partial c_v}{\partial v} + \frac{1}{T}\frac{\partial p}{\partial T}\left(1 - \frac{T}{c_v}\frac{\partial c_v}{\partial T}\right)\right] \tag{A.12}$$